Synthesis and Characterization of Nanostructured, Mixed-Valent Compounds for Electrochemical Energy Storage Devices

A Dissertation
Presented to
The Academic Faculty

By

Min Kyu Song

In Partial Fulfillment of the Requirements for the
Degree of Doctor of Philosophy in the
School of Materials Science and Engineering

Georgia Institute of Technology

December 2011

Synthesis and Characterization of Nanostructured, Mixed-Valent Compounds for Electrochemical Energy Storage Devices

Approved by:

Dr. Meilin Liu, Advisor
School of Materials Science and Engineering
Georgia Institute of Technology

Dr. Kenneth Sandhage
School of Materials Science and Engineering
Georgia Institute of Technology

Dr. Preet Singh
School of Materials Science and Engineering
Georgia Institute of Technology

Dr. Tom Fuller
School of Chemical and Biomolecular Engineering
Georgia Institute of Technology

Dr. Lawrence A. Bottomley
School of Chemistry and Biochemistry
Georgia Institute of Technology

Date Approved: October 21, 2011

This dissertation is dedicated to my lovely wife, JungHoon, our dearest daughter, Deborah, and our esteemed parents in Korea for their endless love and support.

ACKNOWLEDGEMENTS

I wish to give special thanks to my advisor, Dr. Meilin Liu, for his kind guidance, support and encouragement during my doctoral study at Georgia Tech. Without his trust, insightful suggestions and enormous knowledge, this thesis would not have been possible. I also would like to express my gratitude to my Ph.D. thesis committee, Dr. Kenneth Sandhage, Dr. Lawrence A. Bottomley, Dr. Preet Singh, and Dr. Tom Fuller, for their precious time, help and careful review of this thesis.

I am much indebted to all current and previous members of the Liu group for their assistance and cordial friendships. Most of the results in this thesis would not have been available without the enjoyable collaboration with Shuang Cheng. I would also like to express my great appreciation to Dr. Wentao Qin, Dr. JongJin Choi, Dr. YongMan Choi, Dr. Mingfei Liu, Kevin Blinn, Xiaxi Li, and Samson Lai for their help and fruitful discussions. I would especially like to mention my lab mates, Matt Lynch and Lei Yang, who showed me the standard of excellence in research.

Special thanks must be given to all collaborators outside the Liu group for their valuable assistance, including Dr. Kyung-Wan Nam and Dr. Xiao-Qing at Brookhaven National Laboratory, Dr. Haiyan Chen and Dr. Trevor A. Tyson at New Jersey Institute of Technology, Dr. Jianming Bai at Oak Ridge National Laboratory, Dr. Shucheng Xu and Dr. Angelo Bongiorno in the School of Chemistry and Biochemistry at Georgia Institute of Technology, and Jangsoo Lee and Dr. Jaephil Cho at Ulsan National Institute of Science & Technology, Korea.

Finally, I would like to express my sincerest gratitude to my lovely wife, JungHoon, who has filled my life and heart with her endless love. I would never have achieved this academic goal if it were not for her continual unselfish support. I also owe my great thanks to my daughter, Deborah, for bringing me the most joyful moments during my hardest times. She reminds me to be a better person every morning; I promise I will be the good father she deserves. Lastly, I would like to give my deepest thanks to my parents and all of my family members in Korea for the love and warm support they have provided throughout my life. They have been and will always be my best source of inspiration.

Financial support from the DOE Energy Frontier Research Center (HeteroFoaM, DE-SC0001061) is greatly acknowledged.

TABLE OF CONTENTS

LIST OF TABLES

LIST OF FIGURES

SUMMARY

Electrical energy storage systems play a vital role in efficient use of electricity in microgrids or smartgrids to bridge the gaps between demand and supply, especially for renewable energy sources of intermittent and cyclic nature (e.g., solar- or wind-based electrical generation). In the transportation sector, the transition from the current hybrid electric vehicles to all-electric vehicles hinges critically on the development of electrical energy storage systems with dramatically improved energy and power density, durability, and reduced cost.

However, the performance of current electrical energy storage systems (both batteries and electrochemical capacitors) are not capable of meeting tomorrow's energy storage requirements for advanced transportation, commercial, and residential applications. This is because batteries often suffer from slow power delivery, limited life-time, and long charging time whereas electrochemical capacitors suffer from low energy density. While extensive efforts have been made to the development of novel electrode materials for innovative electrical energy storage devices, progress has been hindered by the lack of a profound understanding of the complex charge storage mechanism. Therefore, the main objective of this research is to develop novel electrode materials which can exhibit both high energy and power density with prolonged life-time and to gain a fundamental understanding of their charge storage mechanism.

First, this thesis describes the controlled synthesis of thin, conformal coating of nanostructured, mixed-valent manganese oxides onto porous carbon fiber papers and their application in electrochemical capacitors. The novel electrodes exhibited

dramatically enhanced pseudocapacitive behavior in aqueous electrolytes, demonstrating an order of magnitude increase in energy density without a penalty for power density when normalized to the weight of active materials.

Additionally, this thesis outlines the characterization and correlation of the composition, structure, and morphology of electrodes with their electrochemical performance, employing both *in-situ* and *ex-situ* synchrotron-enabled X-ray analysis (diffraction and absorption), and advanced electron microscopy.

Finally, the thesis presents new insights into the enhanced pseudocapacitance and the charge storage mechanism obtained by *in-situ* synchrotron-based X-ray absorption spectroscopy (XAS). The enhanced performance is attributed to the unique mixed-valent (2+, 3+, and 4+) manganese oxides of porous nano-architectures, which may facilitate rapid mass transport and enhance surface double-layer capacitance, while promoting facile redox reactions associated with charge storage believed to be contributed by both Mn and O sites, leading to unprecedented levels of energy and power density.

In particular, the implication that significant amount of charge may be stored at the O sites of nanostructured MnO_x offers potential for taking advantages of these new energy storage mechanisms (in addition to those associated with redox reactions of cations) in rational design of a new-generation pseudocapacitor materials.

CHAPTER 1

INTRODUCTION

1.1. Motivation

The urgent need for clean and secure energy and the emergence of new energy technologies have stimulated a global resurgence in the search for advanced electrical energy storage systems. The desire to develop a more sustainable transportation system, the necessity to reduce our dependence on fossil fuel, and the demand for a clean and secure energy future are driving the development of low or zero emission electric and hybrid electric cars powered by a new generation of electric energy storage (e.g., batteries and electrochemical capacitors) and conversion (e.g., fuel cells) systems. Electric energy storage systems also play an indispensible role in smart grids, managing the mismatch between electrical generation and demand, particularly for renewable and sustainable sources (such as solar, wind, and geothermal) because of their intermittent and cyclic nature. Even for conventional power plants, efficient load-leveling (by storing energy in batteries and chemical fuels and tapping that energy later) can dramatically improve energy efficiency, reliability, and energy security while reducing emissions of greenhouse gases and air pollutants (e.g., CO_2, SO_2, and NO_x). Batteries and electrochemical capacitors often function as the primary power sources in portable electronics such as hand-held communication devices, computers, and cordless tools, and thus greatly influence the performance, portability, and reliability of these devices.

The energy and power storage characteristics of energy storage systems critically impact the commercial viability of these emerging technologies. For example, the

realization of electric vehicles hinges on the availability of energy storage systems with significantly improved energy and power density, durability, and reduced cost. The design, performance, portability, and innovation of many portable electronic devices are limited by the size, power, and cycle life of existing energy storage systems.

Among available electrical energy storage systems, pseudocapacitors represent a promising option for many applications, ranging from portable electronics to electric vehicles[1-3]. While existing batteries are often limited by low power, short cycle life, and long charging time[4], pseudocapacitors may overcome these limitations[5]. Unlike electrochemical double layer capacitors (EDLCs), which store electrical energy by accumulating ions on an electrode surface[6], pseudocapacitors make use of fast redox reactions or phase changes on the surface or subsurface of electrodes[1-3], offering much higher energy densities than EDLCs. However, the rate capability and cycling stability of pseudocapacitors are perceived to be inferior to those of EDLCs and the energy density of pseudocapacitors is believed to be much lower than those of available batteries.

The practical energy and power density, cycling life, cost, and safety characteristics of pseudocapacitors are determined critically by the composition, morphology, and microstructure of the electrode materials used. In order to achieve long cycling life, electrode materials should have high specific capacitance (available charge per unit mass and volume of the material), high cell voltage, as well as high reversibility of electrochemical reactions with minimum change in the dimension, crystal structure, and morphology of the functional components during cycling. For high power density or rate capability, the electrode materials must also have proper architecture and nano-structure to facilitate fast charge transfer across interfaces and rapid transport of reactants

to and products away from active sites for electrode reactions[7]. Design of electrode materials with proper composition, morphology, microstructure, and architecture will be vital to the creation of a new generation of energy storage systems with energy density far superior to existing systems while maintaining excellent rate capability, thus power density[8].

1.2. Research Objectives

The main objective of this research is to explore the correlations between structures, compositions, and morphologies of electrode materials with their charge storage mechanisms and to develop novel electrodes for electrochemical capacitors exhibiting significantly improved energy density while maintaining high power density and excellent cycling life. More specifically, the key objectives of this thesis are listed as follows:

1) To synthesize electrode materials with desired compositions, morphologies, and nano-architecture for high specific capacitance (F/g) and excellent rate-capability.
2) To characterize the structural features of these electrodes using advanced *ex-situ* and *in-situ* techniques such as synchrotron-based X-ray diffraction and absorption spectroscopy, electron microscopy and spectroscopy, and Raman spectroscopy.
3) To investigate the electrochemical behavior of these electrodes in an electrochemical capacitor using various electrochemical techniques, including impedance spectroscopy, CV, I-V characteristics.

4) To correlate the microscopic features (composition, nanostructure, morphology) of the electrode materials with their electrochemical behavior.
5) To gain insights into the charge storage mechanism of these electrode materials which will help the development of design strategies for enhanced electrochemical properties.

It is hoped that this dissertation will provide new insights into the capacitive energy storage process and help us to establish the scientific principles for rational design of novel electrodes for future-generation energy storage systems.

1.3. Organization of the Dissertation

Chapter 2 provides fundamental background information on electrochemical capacitors, various attributes of nanostructures or nano-architectures applicable to electrochemical capacitors.

Chapter 3 focuses on the fabrication of nanoscale, conformal and continuous coating of mixed-valent manganese oxides on carbon fiber papers (CFP) with extensive investigation of structural characterization. Various techniques such as synchrotron-based X-ray diffraction, gas absorption analysis, Scanning Electron Microscopy (SEM) and Transmission Electron Microscopy (TEM) are employed to reveal the unique composition, structure, and morphology of mixed-valent manganese oxides.

Chapter 4 presents electrochemical properties of nanostrutured, mixed-valent manganese oxides. The performance characteristics of the pseudocapacitors based on the mixed-valent manganese oxides are extensively examined using various electrochemical

techniques including cyclic voltammetry, galvanostatic charge-discharge test, electrochemical impedance spectroscopy, and iR-drop analysis. The effect of different cations on performance will be also discussed.

Chapter 5 discusses insights into the enhanced pseudocapacitance obtained by synchrotron-based X-ray absorption spectroscopy (XAS). A possible mechanism for the enhanced pseudocapacitance of this material is proposed based on both *ex-situ* and *in-situ* XAS analysis coupled with electrochemical measurements.

Finally, Chapter 6 lists conclusions of this dissertation and suggests potential research directions for development of future-generation energy storage devices with significantly improved performance to meet the ever-increasing demands of emerging technologies.

CHAPTER 2

BACKGROUND

2.1. Fundamentals of Electrochemical Capacitors

Electrochemical capacitors are devices that store electrical energy by charge accumulation on the surface or subsurface rather than by chemical reactions of bulk materials (i.e., batteries)[5]. There are two types of electrochemical capacitors depending on the charge storage mechanism: either ion adsorption (electrochemical double layer capacitors, EDLCs) or fast redox reactions (pseudocapacitors) on the surface or subsurface of electrodes[1,2]. EDLCs are currently commercialized and use high surface area carbon (typically activated carbons) as electrodes. Because of the high surface area of highly porous carbons and the ultra-thin double layer, EDLCs exhibit very high specific and volumetric capacitances that are several orders of magnitude higher than those of conventional (either electrolytic or electrostatic) capacitors. Therefore, electrochemical capacitors are commonly called as "supercapacitors" or "ultracapacitors."

The first electrochemical capacitor employing porous carbon was invented in 1957 by H. I. Becker at General Electric Company (U.S. Patent 2,800,616)[8]. However, this device was never commercialized until NEC, a Japanese company, introduced the SuperCapacitor™ in 1978. Since then, electrochemical capacitors have evolved through several generations of design. Initially, they were used as backup power devices for CMOS computer memory, but many other applications have since emerged. Presently, they are used for distributed power systems, and considered as back-up power sources for

electric vehicles and hybrid electric vehicles. In 1971, Trasatti and Buzzanca demonstrated that the electrochemical charging-discharging behavior of RuO_2 films was similar to that of capacitors. From this, Conway et al. developed RuO_2-based electrochemical capacitors which exploited fast redox reactions on the electrode surface. Since 1990, a great deal of scientific and technological effort has been devoted to the development of high-performance electrochemical capacitors. Overall, electrochemical capacitors exhibit several unique attributes that other energy storage/conversion devices, such as batteries or fuel cells, do not possess. In the following chapters, basic operational principles and unique attributes of electrochemical capacitors are briefly discussed.

2.1.1. Operation Principles of Electrochemical Capacitors

In order to understand the operation principles of "electrochemical capacitors," it is necessary to first review the features of ordinary "electrostatic (or dielectric) capacitors." In general, capacitors store electrical energy physically as equal amounts of positive and negative charge accumulated on plates on either side of an insulating (dielectric) material. When the two plates are connected by a conductor, current flows until charge is balanced between the plates. The capacitor can be returned to its previous charged state by applying a voltage across the plates. Capacitance is proportional to the area of the plates and the dielectric constant of the medium between the plates, and inversely proportional to the distance between the two plates. As only physical processes are involved, the charge-discharge cycle is highly reversible and can be repeated with virtually no limit on the number of cycles. The capacitance of electrostatic capacitors is very small, being on the order of microfarads or nanofarads for devices on the scale of

millimeters or centimeters. By incorporating very thin insulating films with a thickness of 10 to 100 nm in a two-electrode capacitor, considerably larger specific capacitances can be obtained. Such devices are often called "electrolytic capacitors" because thin dielectric oxide films are typically formed on the plates by an anodic electrolysis process which can be applied on the surface of metals such as aluminum, tantalum, niobium, etc. The high capacitance of electrolytic capacitors results from the high dielectric constant, the high breakdown field strength, and the very thin, uniform layer of anodically formed metallic oxide. Such capacitors are still dielectric type capacitors and should not be confused with the "electrochemical capacitor," which is the topic of this dissertation.

Electrochemical capacitors are a special type of capacitor based on charging and discharging the surfaces or subsurfaces of high specific-area materials such as porous carbon or oxides. They can store electric charge (thus energy) in a highly reversible way, similar to conventional capacitors, and hence can be operated at specific power densities substantially higher than most batteries. Their capacitance for a given device size is higher by a factor of 10,000 or so, than is achievable with conventional capacitors.

Three types of capacitors (which are commercially available) are compared in Table 2.1 for their mass, volume, cost, and response time assuming energy storage of 1 MJ (0.28 kWh). It is readily apparent that EDLCs are substantially lower in mass, volume, and cost than electrostatic and electrolytic capacitors. However, their significantly slower response time precludes their use in ac filtering applications; they are only useful as dc devices. Therefore, while EDLCs can readily replace electrolytic or electrostatic capacitors where pulse power is required, they are not useful where high-frequency response above 1 Hz is required. However, response times of EDLCs are much

faster than those of batteries, for which a 1 second discharge time is equivalent to a 3600C discharge rate. (Note: nC discharge rate means a device can be completely discharged in 1/n hour. Current batteries are operated, in general, at 1/5~1/10C rates, which is much slower than the discharge rate at which electrochemical capacitors can be operated.) Also, due to their very fast charging rate, electrochemical capacitors may be used to recover energy that is currently being wasted from repetitive processes (e.g., braking in cars or descending elevators). Large-scale electrochemical capacitors can aid power quality regulation of the electrical grid, which can avoid costly shutdowns of industrial operations due to intermittent outages and power fluctuations. They are also currently being explored as future power sources for electric vehicles.

Table 2.1. Comparison of different type of capacitors with 1 MJ of energy storage[8]

Capacitor type	Mass (kg)	Volume (m^3)	Cost ($)	Response time (seconds)
Electrostatic	200,000	140	700,000	10^{-9}
Electrolytic	10,000	2.2	300,000	10^{-4}
Electrochemical	100	0.1	15,000	1

The structure of electrochemical capacitors is quite different from electrostatic capacitors described above, as the latter is a single capacitor comprising two conductors separated by an insulator (dielectric media). In contrast, electrochemical capacitors

consist of two capacitors in series. Like conventional electrochemical systems, electrochemical capacitors have two electrodes immersed in an electrolyte which are separated by an ion-permeable membrane or electrolyte. Each electrode/electrolyte interface represents a capacitor; therefore, the complete cell comprises two capacitors in series, for which the equivalent circuit is shown in Figure 2.1.

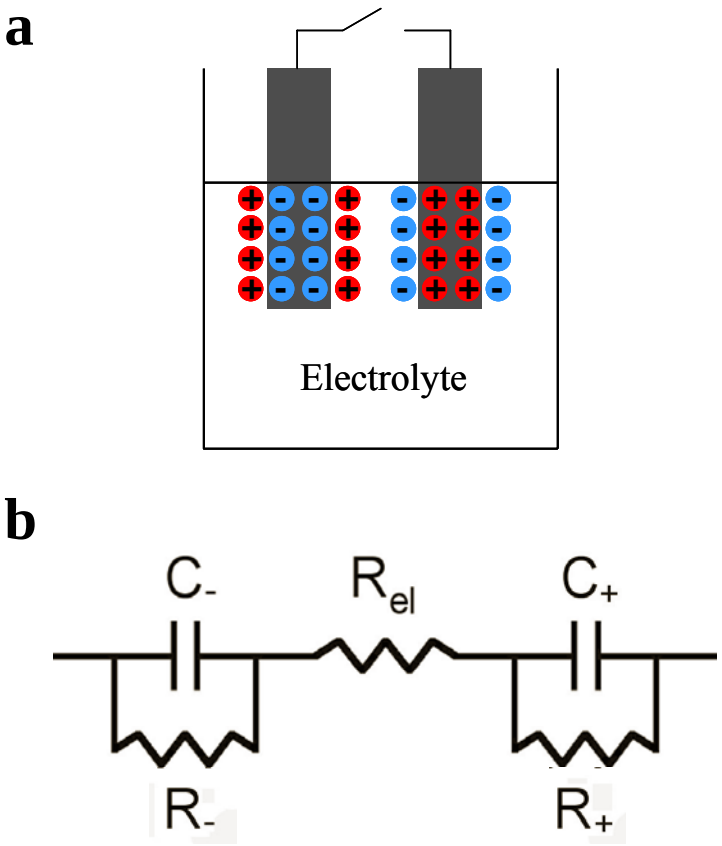

Figure 2.1. a, Schematic of a simple electrochemical capacitor made by immersing two carbon loads in a beaker containing electrolyte (e.g. salt water) and connecting them to a power source. Charged double layer persists after the power source is removed and energy is stored. **b,** Equivalent circuit diagram of a simple electrochemical capacitor.

In the Figure 2.1 (b), R+ and R− represent leakage resistances; and in the limit where they are large (which is almost always), the total capacitance, C_{total}, is given by equation (2.1), where C_+ and C_- are the respective capacitance of each half.

$$\frac{1}{C_{total}} = \frac{1}{C_+} + \frac{1}{C_-} \qquad (2.1)$$

The capacitance at each electrode interface (C_+ and C_-) is a double-layer capacitance, C_{dl}, which can be described by equation (2.2), where ε is the dielectric constant of the electrolyte, A is the electrode surface area accessible to electrolyte ions, and d is the thickness of the double layer.

$$C_{dl} = \frac{\varepsilon A}{d} \qquad (2.2)$$

To better understand double layer capacitance, it is helpful to review the double layer that forms at all electrode interfaces immersed in electrolyte solutions. The model of the double layer originated from the work of Helmholtz (1853) on the interfaces of colloidal suspensions and was subsequently modified by Gouy, Chapman and Stern, and later Grahame. Their models are presented in Figure 2.2, showing capacitor-like structures.

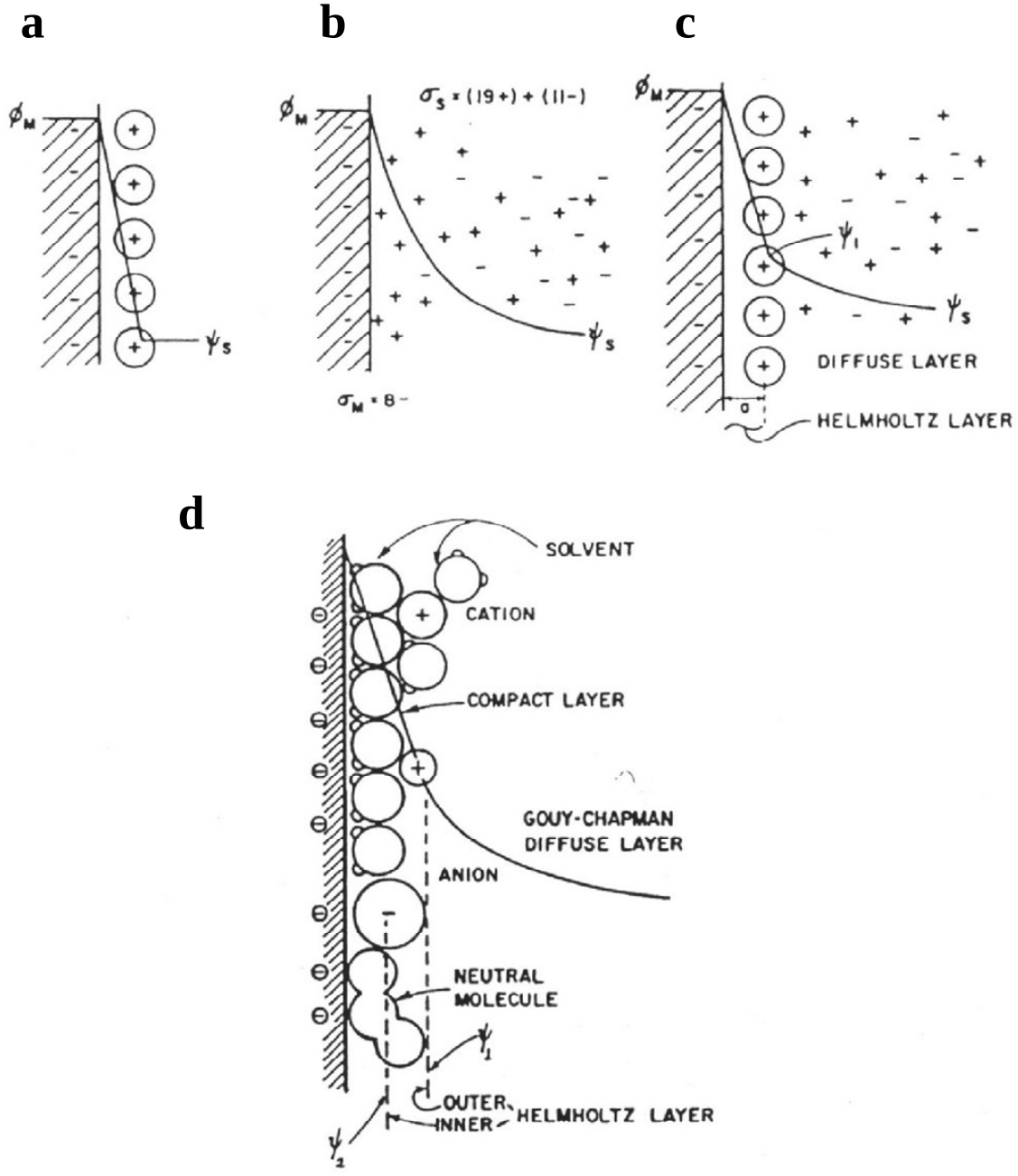

Figure 2.2. Schematic models of the double-layer structure[5]: **a,** Helmholtz model, **b,** Gouy-Chapman model of the diffuse layer, **c,** Stern's model combining Helmholtz model and Gouy-Chapman model and **d,** Grahame's model.

Helmholtz first proposed a capacitor-like separation of anionic and cationic charges across the interface of colloidal particles in the electrolyte. For electrode interfaces with an electrolyte solution, this concept was extended to model the separation of "electronic" charges residing at the metal electrode surfaces due to the corresponding potential difference between the electrode and the solution boundary at the electrode. This charge separation manifests as excess negative charge densities under negative polarization with respect to the electrolyte solution or as a deficiency of electron charge density under positive polarization. Relative accumulations of cations or anions develop in response to positive or negative electric polarization of the electrode respectively. Assuming no electron transfer across the interface, i.e. an ideally polarizable electrode, Grahame proposed that an electrical equilibrium can be established at the interface resulting in a "double layer" of separated charges (either electrons or an electron deficiency at the metal side and cations or anions at the solution side of the interface boundary), hence negative and positive, across the interface.

Electrochemical capacitors may have much higher capacitance than electrostatic and electrolytic capacitors because of the minute separation distance (d) and high specific surface area of their electrodes (e.g. nanoporous carbons for EDLCs). The maximum stored energy (E) and the peak power (P) of electrochemical capacitors are given by equations (2.3) and (2.4), respectively, where C is the capacitance in Farads, V is the operating voltage in volts, and R is the equivalent series resistance in ohms.

$$E = \frac{1}{2} C V^2 \qquad (2.3)$$

$$P = \frac{V^2}{4R} \qquad (2.4)$$

Cell voltage is also a very important operating parameter, which is apparent from equations (2.3) and (2.4), as both the energy and power density of an electrochemical capacitor are proportional to the square of the operating voltage. The operating voltage of the cell depends on electrolyte stability. Aqueous electrolytes, such as sulfuric acid (H_2SO_4), offer the advantage of high ionic conductivity, but suffer from a low breakdown potential of about 1.2 V. In contrast, organic electrolytes such as acetonitrile (CH_3CN) allow operation near 3 V without decomposition, but their electrical resistance is at least an order of magnitude higher than that of aqueous electrolytes.

Like other energy storage devices, high internal resistance limits the charge/discharge rate, thus power density, of electrochemical capacitors. This resistance is generally termed as equivalent series resistance (ESR), the technical term for the resistance of the device when it has a 0° phase angle between current and voltage for an applied ac signal, and therefore appears exactly like a resistor. Factors contributing to the ESR of electrochemical capacitors include the ionic resistance of the electrolyte, electronic resistance of the electrode materials, charge transfer resistance at interface of electrode/electrolyte.

2.1.2. Pseudocapacitors

In addition to EDLCs which store electrical energy through the formation of double layer at the interface between porous electrode (e.g. carbon) and electrolyte, a different type of capacitance can develop at electrodes when the Faraday charge depends linearly (or approximately linearly) on the applied voltage. In this case, the electrode shows a capacitor-like behavior (capacitance). This capacitance is faradaic and not

electrostatic in nature. This is an important distinction from double-layer capacitance, and therefore it is called "pseudo" capacitance. Pseudocapacitance can be as much as an order of magnitude greater than double layer capacitance, because electrochemical charge-transfer processes (faradaic reactions) occur. In other words, pseudocapacitors store energy in chemical reactants (or bonds) capable of generating charge, while EDLCs store energy directly as charge. As EDLCs store electrical energy physically without any chemical reactions or phase changes, the process is highly reversible and EDLCs show long lifetimes[6]. However, they suffer from very limited energy densities compared to conventional batteries. In this regard, pseudocapacitors have generated interest as they exhibit favorable features of EDLCs and batteries, having great potential to address critical gaps between chemical and capacitive energy storage devices.

Certain materials exist which undergo electron transfer reactions yet behave in a capacitive manner. Capacitors based on materials undergoing fast, reversible redox reactions at the electrode surface or subsurfaces with ions in the electrolyte are called pseudocapacitors as they store electrical energy via mechanisms other than formation of an electric double layer, but otherwise behave electrically like capacitors. Transition metal oxides (such as RuO_2) and conducting polymers (such as polyaniline) have been intensively studied for use in pseudocapacitors as they exhibit fast charge and discharge like a conventional double-layer capacitor, but with much higher specific capacitances than EDLCs. RuO_2-based electrodes provide one of the best examples of pseudocapacitance because they exhibit almost constant capacitance over a wide voltage range with excellent reversibility and cycle life. However, because surface redox reactions are involved and the conductivity of RuO_2-based electrodes is lower than that of

carbon in EDLCs, pseudocapacitors often suffer from poor cycling stability and rate capability. A further drawback of RuO_2 is that it is too expensive for commercial applications and has thus been employed only in military applications.

2.1.3. Comparison of Electrochemical Capacitors and Batteries

As mentioned above, the fundamental difference between batteries and EDLCs is that the former store energy through chemical bonds, whereas the latter store energy directly as charge. To demonstrate the major differences between rechargeable batteries, EDLCs, and pseudocapacitors, important parameters are compared in Table 2.2.

The discharge rate and power density of batteries is primarily limited by the kinetics of electrode reactions and the mass transport of the reactants. In contrast, EDLCs have virtually no reaction kinetics to limit the rates of charge/discharge and thus can exhibit remarkably high power density. Furthermore, because EDLCs store charge physically rather than chemically, they experience no volume or phase changes during the charge/discharge process, leading to highly reversible charge storage and excellent cycling performance. As noted in Table 2.2, pseudocapacitors exhibit features of both batteries and EDLCs in terms of their charge storage mechanism. As pseudocapacitors involve charge-transfer reactions (i.e., faradaic reactions), their power delivery capabilities are limited by reaction kinetics and mass transfer, although they are much faster than conventional batteries; pseudocapacitors can be described as high-power rechargeable batteries.

Table 2.2. Comparison of batteries, EDLCs, and pseudocapacitors[8]

Property	Battery	EDLC	Pseudocapacitor
Charge storage mechanism	Chemical	Physical	Chemical + Physical
Limitation of power density	Reaction kinetics, Mass transport	Ionic conductivity of electrolyte	Reaction kinetics, Mass transport
Limitation of energy density	Electrode mass	Electrode surface area	Electrode mass + Electrode surface area
Output voltage	Contant value (plateau)	Changing value (linear)	Changing value (linear)
Limitation of charge rate	Reaction kinetics, Mass transport	Ionic conductivity of electrolyte (very high, same as discharge rate)	Reaction kinetics, Mass transport
Limitation of cycle life	Physical stability, Chemical reversibility	Side reactions	Physical stability, Chemical reversibility

An important difference between the discharge (or charge) behavior of EDLCs and batteries is that EDLCs always exhibit a linear increase in voltage on charging and a linear decrease in voltage on discharging. On the contrary, an "ideal" battery has a constant voltage plateau during discharge/charge except as the state of charge approaches 0 or 100%. Although pseudocapacitors involve charge transfer reactions, most reactions take place on or near the electrode surface, so they behave like a capacitor. Their charge-discharge behavior resembles that of EDLCs; their voltage changes linearly as charge is stored or released.

Another major difference between batteries, EDLCs and pseudocapacitors is in their energy density and power density. Chemical reactions in the battery offer high

energy density, whereas physical charge storage in EDLCs does not. The reason for this major energy difference can be attributed to the fact that most of the bulk material in a battery electrode contributes to energy storage (thus capacity), but only the surface area of porous carbon electrodes contribute to energy storage (thus capacitance) in EDLCs.

A convenient way to compare the operational characteristics of batteries and electrochemical capacitors is to plot their power density as a function of energy density, the so-called Ragone plot as shown in Figure 2.3. The capacitors shown on the low-energy-density end are dielectric and electrolytic types widely used in power and consumer electronic circuits. These conventional capacitors can deliver very high power with ultra fast response time and virtually unlimited life. However, their energy density is very low; they can store only very small amounts of energy and are not useful for applications in which considerably large energy storage is needed. Conversely, electrochemical capacitors can exhibit a fairly broad range of energy and power densities. In particular, the high discharge/charge rates of EDLCs have led to their use in various applications requiring high power. However, their low energy densities have prevented more widespread applications. In contrast, batteries demonstrate high energy densities with slow charge/discharge rates and limited life.

In summary, as previously discussed in the Introduction chapter, the performance of current electrical energy storage systems (both batteries and electrochemical capacitors) are not capable of meeting tomorrow's energy storage requirements for advanced transportation, commercial, and residential applications. For instance, new energy storage systems with substantially higher energy and power densities and faster

recharge times must be developed if electric vehicles are to be widely adopted as replacements for gasoline-powered vehicles.

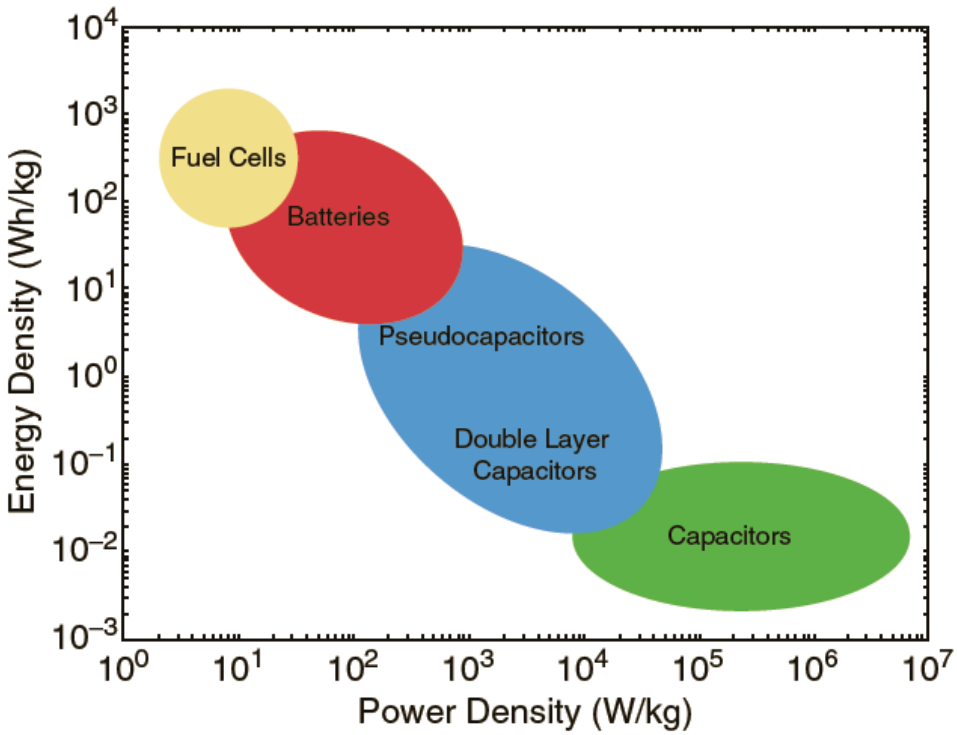

Figure 2.3. Comparison of the energy density and power density for fuel cells, batteries and capacitors[4].

The author strongly believes that such development would be only possible when we take full advantage of EDLCs, especially their extraordinarily high discharge/charge capabilities and capacity for repeated cycling, together with the large energy storage capabilities of batteries. In this regard, pseudocapacitors should receive more attention as they exhibit favorable features of EDLCs and batteries, thus having high potential to

address critical gaps between chemical energy storage devices (i.e. batteries) and capacitive energy storage devices (i.e. capacitors).

To achieve this ambitious goal, it is necessary to design novel electrodes which can exploit both chemical and surface charge storage mechanism. We also need to increase the fundamental understanding of both EDLCs and batteries, which will provide a vital background for the development of such devices. Many complex and interrelated chemical and physical processes occur in both EDLCs and batteries. However, our knowledge of these processes at present is quite limited. Although EDLCs and batteries have been intensively studied for many years, there remain many fundamental gaps in understanding the atomic- and molecular-level processes governing the operation and performance limitations of pseudocapacitors. Fundamental research is urgently needed to unravel the underlying principles of these complicated and interrelated processes. To realize the full potential of pseudocapacitors, new materials and novel physical/chemical processes are needed to improve both their energy and power densities. Incremental changes in existing materials will not produce the breakthroughs needed to realize these improvements. The major challenges in realizing this vision are described in the next chapter.

2.1.4 Challenges and Opportunities facing Electrochemical Capacitors

To develop revolutionary concepts, it is necessary to develop a more fundamental understanding of the physical and chemical processes that occur in pseudocapacitors. For example, novel electrode materials which can simultaneously exploit multiple charge storage mechanisms need to be identified. To do so, charge storage mechanism first

needs to be fully understood to facilitate the design of suitable materials for high-performance pseudocapacitors. New continuum, molecular, and quantum mechanical models are needed to predict new material chemistries and architectures, and to discover new phenomena at the electrochemical interfaces. Only with advances in fundamental science will pseudocapacitors emerge as an important future energy storage device. More specifically, three primary technical approaches are identified[8] and briefly discussed as follows.

(1) *In-situ* Characterization of the Capacitive Energy Storage Process

The development of electrochemical capacitors with high energy densities while maintaining excellent power delivery capabilities will require a profound understanding of charge transfer and transport processes during the capacitive energy storage process. The interfaces between electrodes and electrolytes are very complex and even less understood for pseudocapacitors. The dynamic nature of these interfaces complicates a sophisticated characterization that is likely necessary to reveal the paths of electrons and ions during the operation.

To understand the change of composition and structure at the interface during charge transport and transfer processes, it is necessary to use more powerful characterization tools. With this fundamental knowledge, completely novel materials or electrode architectures may be designed and new insights into the physicochemical phenomena that underlie the operation of pseudocapacitors can be obtained. New synchrotron-based spectroscopic and scattering techniques combined with microscopic

imaging capabilities at femto-second time resolution and spatial resolution at atomic scales would be required to unravel the complex capacitive charge storage process.

In particular, *in-situ* characterization of the electrolyte/electrode interface at molecular and atomic levels is critical to understanding the fundamental processes of capacitive energy storage. This will require the combination of various electrochemical characterization techniques and advanced analytical tools, so that chemical information can be obtained in real time with high spatial resolution. This *in-situ* characterization will be critical to unraveling materials and novel architectures that exhibit exceptionally high performance. The information obtained through such tools will help us identify the principal causes leading to failure and recommend remedies for them.

(2) Advances in Modeling and Simulation

Understanding how electrode materials store and transport charge in pseudocapacitors is very important for further development, and calls for fundamental study of the charge transfer at the interface and transport mechanisms within the electrodes. In this regard, computational models can provide unique opportunities for understanding the complexities of processes and materials, the understanding of which is required to make revolutionary discoveries that can lead to the next generation of electrochemical capacitors. By modeling and simulation efforts, it would be possible to complement experimental efforts by obtaining better insights into mechanisms, identifying fundamental trends, and discovering new materials and new electro-physical/chemical phenomena at the interfaces. Advances in computational

methodologies can guide experiments and test our fundamental understanding of the various processes involved in capacitive energy storage.

Up until now, however, very few models of pseudocapacitors have been developed, although various modeling and simulation approaches used for battery materials could be applicable. Topics which are important to capacitive energy storage processes include phase changes in electrode materials, ion transport in electrolytes, charge transfer at interfaces, and mixed ionic/electronic transport within electrodes. New computational approaches may allow nanoscale design and modeling of active materials and electrochemical processes occurring across different length and time scales. Computational predictions based on these models will point to new directions in both materials and electrode architectures.

(3) Design of Nanostructured, Multifunctional Electrodes

The performance of electrochemical capacitors is mainly restricted by the performance of the constituent materials including active materials, conductive additives, and insulating binders. It is expected that sophisticated control of an electrode such as pore size, composition, morphology, and architectures can lead to a significant improvement in electrochemical performance. A new generation of electrochemical capacitors may require novel electrode materials with unprecedented levels of power and energy density combining double layer capacitance and pseudocapacitive processes. For instance, novel materials which simultaneously exploit multiple charge storage mechanisms need to be identified. To achieve this objective, a more fundamental understanding of the physical and chemical processes that occur in electrochemical

capacitors is necessary to realize these revolutionary concepts and to enable the design of such novel materials for the next generation of electrochemical capacitors.

Recent advances in nanoscience and nanotechnology may offer exciting possibilities for the development of revolutionary nano-architectures that simultaneously optimize the transport of ions and electrons, thus dramatically improving pseudocapacitor performance. However, little is known about the physicochemical nature of pseudocapacitance, especially at nanoscale dimensions. The capability to synthesize nanostructured electrodes with tailored, high-surface area architectures may offer the potential for storing multiple charges at a single site, dramatically improving capacitance. The addition of surface functionalities could also contribute to high capacitance and reversible charge storage, as well as fast charge-discharge capabilities. This could be achieved through a variety of strategies such as a thin, conformal coating of nano-porous multiphase active materials on three-dimensional porous architectures. In the following chapter, the unique attributes of nanostructure or nano-architectures applicable to electrochemical capacitors are presented.

2.2. Unique Attributes of Nanostructures and Nano-architectures

2.2.1. Why do Nanomaterials Behave Differently?

(1) Fast transport of mobile species: To understand why nanomaterials show unique properties, it is first important to appreciate the characteristic length and time scales of energy carriers. It is well known that when the dimensions of materials, grains, or domains become comparable to (or less than) the characteristic length scale (such as the mean free path) of phonons, photons, electrons, ions, and molecules, many physical

phenomena change significantly, often leading to new modes for transport of charge, mass, and energy and for chemical and energy transformation processes. As shown in Table 2.3, the length scales of mobile species in pseudocapacitors (electrons, ions, and molecules) fall generally in the order of 0.1 to 100 nm, suggesting that some unique physicochemical properties of materials and novel reaction pathways may become operative in the nanoscale regime. Thus, materials with proper nano-scale dimensions and architectures (with reduced length scale and characteristic time scale of physical phenomena) have the potential to dramatically enhance the transport of electrons, ions, and molecules associated with the cycling of pseudocapacitors, significantly accelerating the rate of chemical and energy transformation processes.

Table 2.3. Characteristic length and time scales for electrons, molecules, and ions under ambient condition[9].

Energy carriers	Wavelength / nm	Mean free path / nm	Relaxation time / ns
Electrons			
- in semiconductors/dielectrics	~ 1 - 50	~ 1 - 500	~ 10^{-3} - 10^{-2}
- in conductors/metals	~ 0.1 - 1	~ 1 - 10	~ 10^{-5} - 10^{-4}
Molecules/Ions			
- in gas/plasma	~ 10^{-2} – 1 [a]	~ 10^{3} - 10^{7}	~ 1 - 100
- in liquid/electrolyte	-	~ 0.1 - 1	~ 10^{-3}
- in solid/electrolyte	-	~ 0.1 - 1	~ 10^{-3}

[a] refers to de Broglie wavelength.

(2) Enhanced surface reactivity: From a structural point of view, nanomaterials are quite unique when compared to bulk materials, arising from the fact that nanomaterials

structurally consist of only 100 – 10,000 atoms. In nanomaterials, as shown in Figure 2.4, the ratio of the number of surface atoms to that of bulk atoms for a nanomaterial is far greater than that for a bulk material (a bulk material is any >100 nm). Surface atoms have fewer neighbors than interior atoms, leading to lower coordination numbers and more unsatisfied bonds, quite unlike bulk material behavior. The large surface free energy, surface defects, and surface states may critically influence the chemical reactivity of materials[10]. For example, there could be a higher density of corner or edge atoms, which have even lower coordination numbers and greater affinity towards other atoms and molecules. Vacancies or other defects not seen in bulk materials may exist on the surface of nanostructures, which may greatly enhance the rate of electrochemical reactions.

The large surface free energy and stress/strain relations of nanomaterials may fundamentally influence their phase stability and structural transformations, which in turn influence their electrochemical and catalytic activity. The surface free energy of nanomaterials can be estimated as

$$\mu^o(r) = \mu^o(r = \infty) + 2(\gamma/r)V \qquad (2.5)$$

Here $\mu^o(r)$ and $\mu^o(r = \infty)$ refer, respectively, to the chemical potential of nano and bulk materials, γ is the effective surface tension, r is the effective grain radius, and V is the partial molar volume.

Clearly, surface energy increases dramatically with decreasing particle size. As a result, phases that may not be stable in bulk materials can become stable in nanostructures and vice versa. This association of structural stability with size has been observed in many oxide systems such as TiO_2[11,12] and Al_2O_3[13]. Size-induced modification of lattice parameters has been observed in many oxide nanoparticles including Fe_2O_3[14] and CeO_2[15].

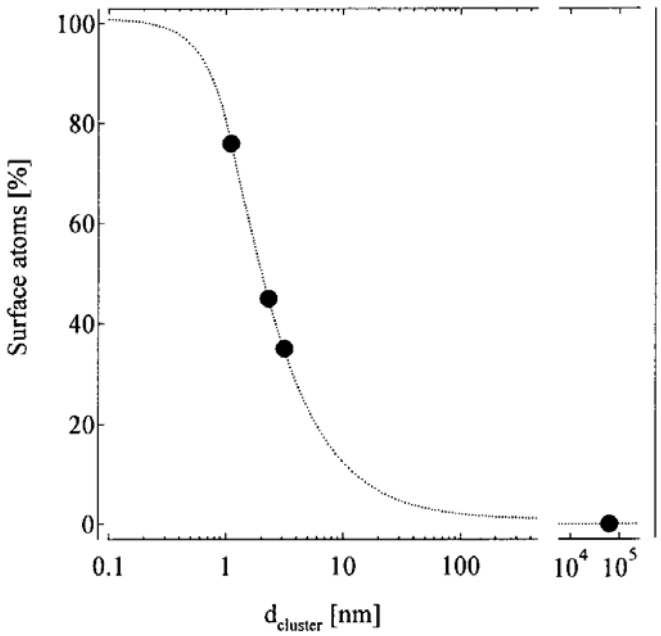

Figure 2.4. The percentage of surface atoms as a function of palladium cluster diameter. The percentage is calculated with respect to the total number of atoms[16].

(3) Modified electronic structure: The other important effect of nanostructures is related to the change of their electronic structures in the nanoscale regime between bulk materials and isolated atoms or molecules. As illustrated in Figure 2.5, the nanostructure induces the so-called "confinement effect" which originates from discrete electronic states of isolated atoms[10,17]. Thus, the dimension change from large bulk structures to small nanostructures can lead to changes in the band gap size[18] or a redistribution of atomic charges[19,20], which alters the chemical properties of materials. It was reported that decreasing particle size indeed changes the magnitude of the band gap, influencing chemical reactivity[21]. For oxide nanostructures in particular, another important factor accounting for enhanced chemical reactivity is the long-range Madelung field[22]. The

Madelung field is not present or greatly reduced in nanostructures; there could be variations in the oxygen/metal ratio compared to that of bulk materials, affecting chemical and electronic properties[10].

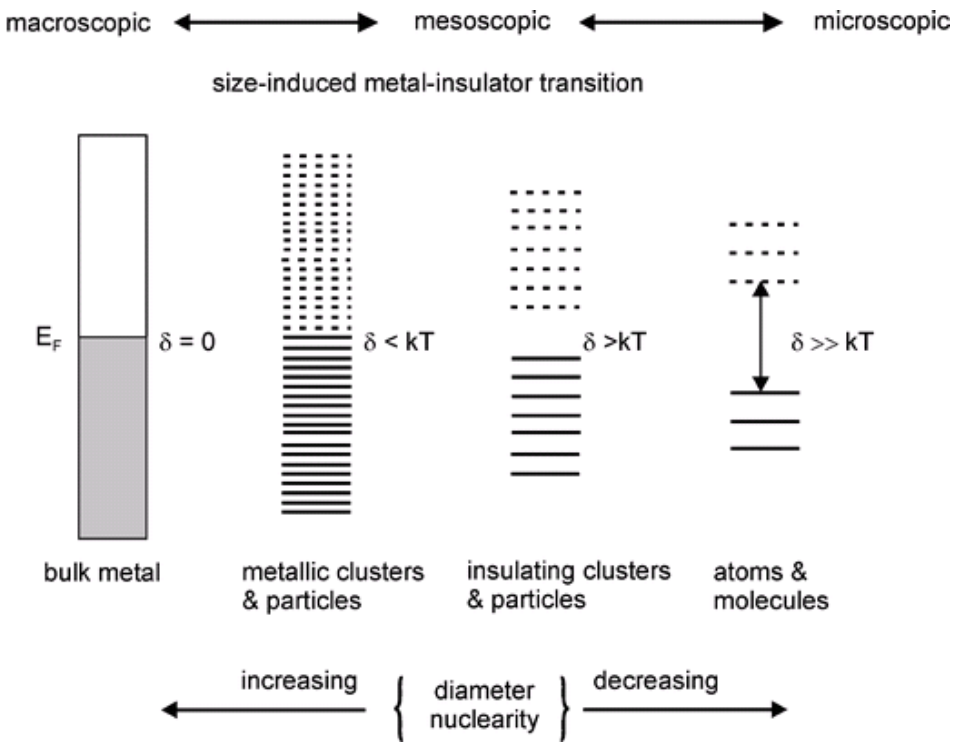

Figure 2.5. Example of quantum confinement effects in materials with delocalized electron states: the density of states as a function of the numbers of atoms in a system[17].

2.2.2. Unique Advantages of Nanostructured Electrodes for Pseudocapacitors

Materials with a wide variety of nanostructures or nano-architectures can help overcome several difficulties facing the development of novel electrodes for high-

performance pseudocapacitors. The benefits of electrode materials with nanostructures and nano-architectures are briefly summarized as follows.

(1) Large surface area (or surface to volume ratio) increases the contact area between electrode and electrolyte and hence the number of active sites for electrode reactions. This in turn reduces electrode polarization loss and improves power density (or rate capability), energy efficiency, and usable energy density especially with the increased utilization of active electrode materials. Further, it offers increased flexibility for surface modification to achieve multi-functionality including enhanced surface reactivity for the intended electrode reactions, improved surface transport of electro-active species, and tailored surface passivity against undesired electrode-electrolyte reactions by formation of a desired solid-electrolyte interphase (SEI). This advantage is especially important for pseudocapacitors, where chemical reactivity for insertion of cations is vital to reduce charge-transfer losses, to enhance cycling rates, and to improve usable energy density. For electrode materials with very low electronic conductivity (e.g., transition metal oxides), a large surface to volume ratio increases the contact area between electrode and distributed current collectors to make efficient use of the electrode materials, which in turn increases the usable energy density and reduces electrode polarization loss [23].

(2) Short diffusion length associated with the nano-sized dimensions of nanostructured electrodes effectively reduces the distance that inserted ions and electrons must travel through electrode materials during cycling in the solid state. Often, electrode materials with other desirable characteristics have limited ionic and/or electronic conductivity, which can limit the power density (or the rate of operation), the usable

energy density (due to limited utilization of active electrode materials), and energy efficiency (due to mass transport limitation in the solid state). This can be effectively mitigated by the use of nanomaterials. For solid-state diffusion of ions in electrode materials, the characteristic time constant for diffusion (equilibration time), τ, is determined by the diffusion constant, D, and the diffusion length, L, according to:

$$\tau = L^2/D \qquad (2.6)$$

The time for intercalation of ions, τ, decreases with the square of the diffusion length, L, illustrating the remarkable effect of manipulating nanostructures: fast charge storage and high rate capability (thus high power density). For example, the diffusion length would be reduced to the diameter of nano-wires, -tubes, and –rods and the thickness of thin films if they are properly dispersed in the electrolyte (ionic conductor) and the current collector (electronic conductor). Several unique architectures have been developed using low-dimension nanostructured components to achieve fast mass transport and high power density.

(3) Enhanced ionic and electronic conductivity can also be achieved by thin film deposition of a low resistance electronic or ionic conductor, or by the formation of nano-composites, in which the surface of each phase or the interfaces between phases support fast transport of ionic and electronic species. The process of enhanced ionic and electronic transport is still not fully understood. While electro-neutrality should be obeyed in bulk of a homogeneous materials, a space-charge zone can be created at the interface of nanomaterials[24]. These narrow charged interfaces can provide fast pathways for ionic and electronic species, leading to enhanced energy storage processes. Furthermore, nanomaterials may have more ionic and electronic defects not only on the

surface and interfaces but also in the bulk phase, which could affect the ionic and electronic conductivity as well.

(4) Nanostructured materials are known to exhibit significantly enhanced mechanical strength, toughness, and structural integrity [25-28], although the underlying mechanisms are not yet fully understood [26,27,29]. Nanocrystalline materials with grain size less than 100 nm are still a subject of active research[28,30-33]. Improved mechanical strength and structural integrity represent other unique advantages of well-designed nanomaterials in energy storage systems such as batteries and pseudocapacitors. It is well known that low-dimensional nanomaterials (e.g., nano-wires, -tubes, -belts) can be engineered to allow volume change only in certain directions or dimensions. For example, the internal small pores in nano-porous composite electrodes can accommodate the large volume expansion and contraction associated with charge-discharge cycling without mechanical damage or deterioration in microstructure. This attribute ensures the structural integrity of the electrodes, minimizing or eliminating performance fading due to electrical isolation of active electrode materials originated from pulverization of electrodes. As another example, while the bulk form of layered $LiMnO_2$ often suffers from structural instability, nanocrystalline $LiMnO_2$ shows better accommodation of the lattice stress caused by Jahn-Teller distortion, suggesting that nanostructures can also lead to better structural stability[34]. In nanoparticles, charge accommodation can occur mostly at or near the surface and greatly reduces the need for diffusion of inserted cations through bulk materials[35]. This substantially reduces the volume changes and stresses associated with insertion and removal of cations.

(5) The hierarchical architecture of nano-porous structures can improve surface reactivity and stability because of enhanced transport of reactants to (or products away from) the nano-sized pore surfaces, the high surface areas for surface modifications to improve chemical reactivity, and the robust structure for durability. Enhanced chemical reactivity is due to the increased number of active reaction sites and facile transport of electro-active species to the reaction sites. Nanopores with higher surface area per unit mass enhance dispersion of active materials, thus increasing the number of active sites and improving utilization of all catalyst particles.

(6) Nanostructured materials can have charge storage mechanisms other than conventional redox mechanisms, enabling higher capacitances, thus leading to unprecedented levels of energy density. For example, recent studies show that lithium ions can be stored on the surface [36], interface [24,37,38], and in nanopores [39,40] without causing any mechanical crumbling in the electrode, thus leading to excess lithium storage. In particular, surface/interfacial charge storage mechanisms will play more important roles in electrodes comprised of nanostructured transition metal oxides and newly emerging graphene-based materials as shown in Figure 2.6.

(7) In the literature, it has been reported that electrode materials which are inactive towards Li insertion in bulk form become active on the nanoscale [7]. These findings have led to revisiting electrode materials previously thought to have little promise. Examples include nano-sized transition metal binary oxides with conversion reactions. Similarly, multielectron conversion reactions with metal oxyfluorides which perform poorly in bulk form become promising in the nanoscale regime[41]. This

observation may hold some important messages in the development of next-generation pseudocapacitors.

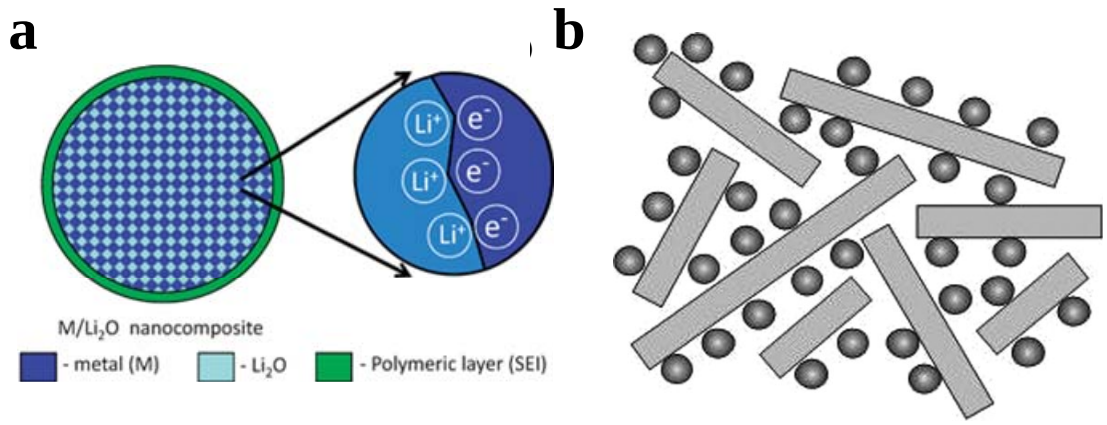

Figure 2.6. Schematic illustration of interfacial storage mechanism in (a) transition metal oxides [38] and (b) graphene sheets [40].

2.2.3. Disadvantages of Nanostructured Electrodes

It should be noted, however, that use of nanomaterials entail high fabrication cost due to complex synthesis processes, low volumetric energy density due to reduced packing density of nanoparticles, and undesired side reactions between the electrode and electrolyte due to large surface areas. Also, nanomaterials tend to form agglomerates during the electrode fabrication process, making it difficult to uniformly disperse them in the electrodes, and their nanoscale dimensions are rather difficult to control. Nanoparticles can suffer from thermodynamic instability when exposed to electric fields, critically affecting their long-term durability and preventing their commercialization.

These shortcomings can be mitigated if the nanostructure and fabrication process are properly designed, offering significantly improved pseudocapacitor performance.

CHAPTER 3

SYNTHESIS AND CHARACTERIZATION OF NANOSTRUCTURED MIXED-VALENT MANGANESE OXIDES

In the previous chapter, background information was provided on operation principles of electrochemical capacitors, the challenges faced by development of energy storage systems and why nanostructures and nano-architectures may help transcend these challenges. In this chapter, a brief description of the technical approach and experimental results are presented and discussed for synthesis of nanoscale, conformal and continuous coating of mixed-valent manganese oxides on carbon fiber paper (CFP) with extensive investigation of structural characterization.

3.1. Why Manganese Oxides?

As previously discussed, a dramatic increase in energy density while maintaining excellent power density and long cycling life would represent a breakthrough in the development of a new generation pseudocapacitors. While considerable efforts have been devoted to the creation of new materials for such devices, progress has been hindered by the lack of a profound understanding of the complex charge storage mechanisms related to intercalation of ions into electrode materials (with layered or channeled structures), reaction of ions with active electrode materials (to form new phases), and/or electrochemical adsorption of ions on electrode surfaces. Traditionally, it is believed that pseudocapacitive behavior is associated primarily with redox reactions of the cations (or changes in oxidation states of the cations) in electrode materials during operation[5]. A

suitable electrode material for high-performance should promote fast, reversible redox reactions on the surface or subsurface[1,2].

Recently, among many materials investigated, MnO_2 has attracted much attention because it is abundant, inexpensive, and environmentally benign[42,43]. While MnO_2 has high theoretical capacitance[44] (~1,390 F/g as the oxidation state of Mn ion is changed from 4+ to 3+ over a potential window of 0.8V), its poor electronic conductivity often limits the electrode utilization; only the surface layers may participate in redox reactions. To overcome this limitation, MnO_2 has been mixed with carbon particles or loaded onto carbon supports[43,45-47]. To date, however, the reported specific capacitance of MnO_2 varies from ~150 to ~940 F/g, still far inferior to what is considered as a reasonable replacement for RuO_2. Moreover, the cycling stability of MnO_2 still needs further improvement. Although higher specific capacitance (~1,145 F/g) has been reported[48], the MnO_2 was deposited on nanoporous gold and, thus, could be less competitive economically for practical applications. Further, the rate capability of MnO_2 is still unsatisfactory for large-scale applications such as electric vehicles. Although higher capacitance (~1,380F/g) has been reported for MnO_2[44], it was prepared as an ultra-thin film on a flat current collector, making it infeasible for practical applications.

The ground-state electronic configuration of Mn is $1s^2 2s^2 2p^6 3s^2 3p^6 3d^5 4s^2$. With several oxidation states and a wide range of phases, manganese is a vital component in photosynthetic systems due to its unique ability to cycle between various oxidation states.[49] Manganese compounds are known to exhibit various oxidation states ranging from -3 to +7 as shown in Table 3.1.

Table 3.1. Representative manganese compounds and their oxidation state

Oxidation state	Geometry	Example
Mn^{3-}	Tetrahedral	$Mn(NO)_3CO$
Mn^{2-}	Square	$[Mn(phthalocyanine)]^{2-}$
Mn^{-}	Trigonal bipyramid	$Mn(CO)_5^{-}$
Mn^{0}	Octahedral	$Mn_2(CO)_{10}$
Mn^{+}	Octahedral	$[Mn(CN)_6]^{5-}$
Mn^{2+}	Tetrahedral	$MnCl_4^{2-}$
Mn^{3+}	Octahedral	MnF_3
Mn^{4+}	Octahedral	MnO_2
Mn^{5+}	Tetrahedral	MnO_4^{3-}
Mn^{6+}	Tetrahedral	MnO_4^{2-}
Mn^{7+}	Tetrahedral	MnO_4^{-}

Both very low and high oxidation state can be stabilized by the formation of metal complex (or coordination complex), a structure consisting of a central atom or molecule weakly bonded to surrounding atoms or molecules (i.e. ligands). The special feature of high valence Mn is the abundance of disproportionation reactions; they are simultaneously reduced and oxidized so as to form two different products.

$$2Mn^{3+} \rightarrow Mn^{2+} + Mn^{4+}$$

$$2Mn^{5+} \rightarrow Mn^{4+} + Mn^{6+}$$

$$3Mn^{6+} \rightarrow Mn^{4+} + 2Mn^{7+}$$

In particular, manganese oxides can assume many different crystal structures upon accommodation of other metal cations. The basic building block for most manganese oxide structures is the MnO_6 octahedron, which can be assembled into a large assortment of different structures by various patterns of sharing edges and/or corners[50]. These complex features often give rise to unusual properties of manganese oxide. For example, it was reported that the mixed-valence of manganese oxides provided semiconducting properties as well as dramatic enhancement of catalytic activities towards oxidation of various organic compounds[51,52]. Other suggested potential applications of mixed-valent transition metal oxides included adsorption, electrochemical sensor, and oxidation catalysis[53].

In this dissertation, the author attempts to synthesize nanostructured, mixed-valent manganese oxides and explore their unique properties as electrodes for pseudocapacitors. A brief background on unique properties and structure of mixed-valent compounds is provided in next chapter.

3.2. Theory of Mixed-Valent Compounds

The investigation of mixed-valent compounds has a long and interesting history. Since Prussian blue, a complex Fe(II)/Fe(III) cyanide, was first discovered in 1704, the study of mixed-valent compounds has had significant impacts in chemistry, physics, and biology. In particular, from the late 1960s, molecular mixed-valent compounds began to receive great attention due to their unique optical properties arising from significant electron transitions between donor and acceptor sites. The intense blue color of Prussian blue is related to the energy of the electron transfer from Fe(II) to Fe(III). Many mixed-

valent compounds can absorb specific wavelengths of visible light via inter-valence charge transfer. Prussian blue changes from blue to colorless upon reduction of Fe(III) to Fe(II), eliminating the inter-valence charge transfer that results in Prussian blue's color.

By definition, mixed-valent compounds contain an element which is present with more than one oxidation state. Mixed-valent compounds contain donor (D) and acceptor (A) sites separated by a bridge (B) as shown in Figure 3.1. These two redox sites does not necessarily have to be a metal; pure organic mixed-valent compounds have been also identified[54]. To date, compounds of group 8-11 transition metals have been most intensively studied. In particular, compounds of iron, ruthenium, platinum and copper have been widely studied[55]. For example, many mixed-valent copper-based oxides have been developed as superconductors. The compound $YBa_2Cu_3O_7$ has mixed-valent Cu(II) and Cu(III). Also, a number of rare-earth compounds, with atomic-like f levels coexisting with wide s-d band at the Fermi level, have shown very unique thermal and magnetic properties[56]. However, mixed-valence chemistry has not yet been fully understood and a fundamental understanding of the relationship between mixed-valent structure and properties is still lacking. The electronic structure of some mixed-valent compounds have been under debate for more than 30 years[54].

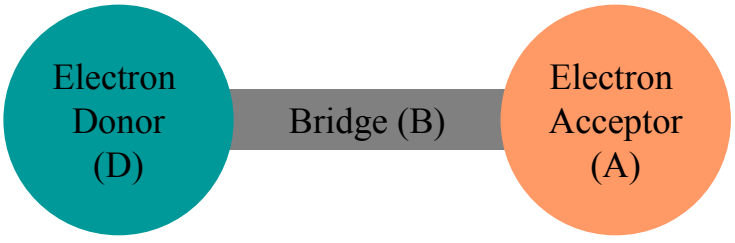

Figure 3.1. Basic building block of mixed-valent compounds

Two key factors (and their interaction) which determine their unique properties are the "electronic coupling" between the two redox sites, and the "reorganization energy" associated with electron transfer between them[54]. Charge localization or delocalization has been a central issue in mixed valence chemistry. For one-electron mixed valence compounds comprised of two redox sites R (Donor and Acceptor) connected by a bridging unit b, two extreme states can be formed. They are described by R^{n+}-b-$R^{(n+1)+}$ (complete localization), and $R^{(n+0.5)+}$-b-$R^{(n+0.5)+}$ (full delocalization); anything between these two states are also possible[57].

The first comprehensive study of mixed-valence compounds was done by Robin and Day in 1967[58]. They proposed a classification scheme that has been generally adopted by the scientific community[58]. Completely localized systems belong to class I, fully delocalized molecules are class III, and systems in between belong to class II. In other words, mixed-valent compounds are categorized as class I, II or III depending on the strength of the electron interaction between the oxidized and reduced sites, ranging from essentially zero (class I), to moderate (class II), to very strong electron coupling (class III).

The properties of class I compounds are essentially coming from the separate sites. Class II compounds can exhibit novel optical and electronic properties in addition to those from the separate sites. However, the interaction between two sites is sufficiently weak that valence electrons are trapped or localized. Class III compounds have such a high degree of interaction between the donor and acceptor sites that two separate minima are no longer discernible. The electron is fully delocalized and the compound can exhibit

unique properties. More detailed features of different class compounds are described as follows.

Class I: The compounds have metal atoms of the same element in two different valence states, but there is no electron exchange between them. This is because two different types of cations have different coordinations by anions or other ligands. Verwey's Rule states that the cations in mixed-valent compounds must be located in equivalent crystallographic sites for any valence electrons to be exchanged[59]. A good example of this class is Mn_3O_4 which consists of octahedrally coordinated Mn(III) and tetrahedrally coordinated Mn(II). As different cations are in distinct sites, the valence electrons are trapped or localized at a single site.

Class II: These mixed-valent compounds have cations in similar coordination. When metal atoms have similar coordination by ligands, their valence electron orbitals can overlap properly, forming a channel through which the electrons can resonate between the metal centers. Their characteristics fall in between class I and class III. There is some degree of localization, but inter-valent electron exchange can occur with low levels of activation energy. Thermal activation can induce electron transfer from one site to another via the anion (or ligand) bridge. The best example of this type compound is Prussian blue, which contains octahedrally coordinated iron atoms. There is an iron(II) atom surrounded by six carbon atoms of six cyanide ligands bridged to an iron(III) atom by their nitrogen ends. An inter-valent electron-transfer reaction occurs through the cyanide ligands.

Class IIIA: These are metal cluster compounds with direct metal-metal bonds. Their mixed valence is not distinguishable by spectroscopic methods as the valence is completely delocalized. Niobium oxide, NbO (which is apparently monovalent, not mixed-valent), is a good example of a metal cluster compound. It is a grey solid with metallic conductivity[60]. It has an unusual defect rocksalt structure with 25% ordered vacancies. The niobium atoms are arranged in octahedral sites and there is a structural similarity to the octahedral niobium clusters. The Nb-Nb bond length is 298 pm which compares to 285 pm in the metal[60]. Researchers reported that there are very strong and nearly covalent metal-metal bonds due to a special hybridization between Nb p and d orbitals around the O vacancy sites[61]. Niobium oxide is a superconductor at 1.38 K. The bridging ligands need to support electron transfer and conjugation, and be easily reduced.

Class IIIB: These compounds are often called the "synthetic metals" with metal-metal bonds in an extended atomic lattice. The best example of a synthetic metal is a platinum compound, $K_2Pt(CN)_4Br_{0.3}3H_2O$ (KCP). At room temperature, the mixed-valences (Pt^{2+}, Pt^{4+}) in KCP are perfectly mixed (proportionated) to form the non-integral oxidation state of Pt (2.3+). X-ray diffraction studies of KCP and related compounds revealed that they are composed of stacks of square planar platinum(II,IV) cyanide molecules. While the term “mixed valence” is also used for class III compounds, the electron transitions do not involve net charge transfer, and the two redox centers have an averaged valence state.

Most redox systems studied to date are assigned to class II. Transitions between these classes are possible, and an additional class at the borderline between classes II and

III, the so-called "almost delocalized" mixed-valent compound has been identified[62,63]. Unfortunately, the characterization of such compounds has proven very difficult, and a profound understanding of their behavior has posed a formidable challenge. It is expected that novel donor–acceptor systems located at the borderline between class II and III would have unique properties.

It should also be noted that the mixed-valence chemistry of the early transition metals is considerably less well established, yet a remarkable variety of structurally diverse mixed-valence compounds can be formed from these elements. Their wide range of oxidation states, coordination numbers and geometries can offer great potential for the formation of unique mixed-valent compounds, and many of these may exhibit distinctive bonding, chemistry and properties suitable for various applications. In particular, although early transition elements such as titanium, vanadium and manganese are important in biology, catalysis, and energy storage/conversion science, the controlled synthesis of their mixed-valent compounds and their unique properties have not yet been explored. In this dissertation, the author will demonstrate the controlled synthesis of nanostructured, mixed-valent manganese oxides and explore their unique properties as electrodes for high-performance pseudocapacitors.

3.3. Nanoscale, Conformal and Continuous Coating of MnO_x onto Three-dimensional Porous Carbon Fiber Papers

In addition to synthesis and exploration of mixed-valent manganese oxides as novel electrode materials, the author made an effort to achieve the increase in the energy

density of electrochemical capacitors while maintaining their high rate capabilities and cycling performance by tailored architectures of composite electrodes.

Electrochemical energy storage devices (e.g. batteries and electrochemical capacitors) contain many components (in addition to active materials) that are critical to performance but that do not contribute to the energy or power density; they instead reduce both gravimetric and volumetric capacities (or capacitance). Such components include the conductive additives, insulating binders and bulky current collectors.

However, we cannot simply remove those components from the electrodes as it is very important to ensure a continuous electronic conductive pathway so that the electron can be rapidly inserted or removed from active materials. For instance, since transition metal oxides such as MnO_2 has inadequate electronic conductivity (~10^{-5} S/cm), carbon black (or other highly conductive particles) are often added to the electrode for effective current collection. Usually, carbon and particles of active electrode materials are uniformly mixed and bound to a metal foam/mesh current collector using a binder such as polyvinylidene fluoride (PVDF). To make effective use of all active electrode materials, carbon and the particles of electrode materials must be in intimate contact. At the same time, all carbon particles must maintain continuity to the metal foam/mesh to efficiently collect (or inject) electrons from (or to) active electrode materials during cycling. Degradation of electrode performance originates often from some unfavorable changes in electrode microstructure during cycling. For example, deterioration in connectivity between carbon particles or between carbon and the particles of active electrode materials may lead to gradual performance loss due to electrical isolation of active electrode materials, and reduced rate of cycling.

In addition to electronic pathways, the accessibility of the electrolyte to active materials is also very important. One simple approach to ensure effective ionic transport is to develop porous electrodes to increase surface areas and shorten the diffusion path lengths of ions to the reaction sites. However, as shown in Figure 3.2, the reactions would be still limited on or near surface of porous electrodes especially when very high rates of discharge or charge are used. The distribution of these reaction sites inside a porous electrode would be strongly dependent on the ionic conductivity of electrolyte and electrode microstructure such as porosity, pore size and tortuosity (or interconnectivity) of those pores.

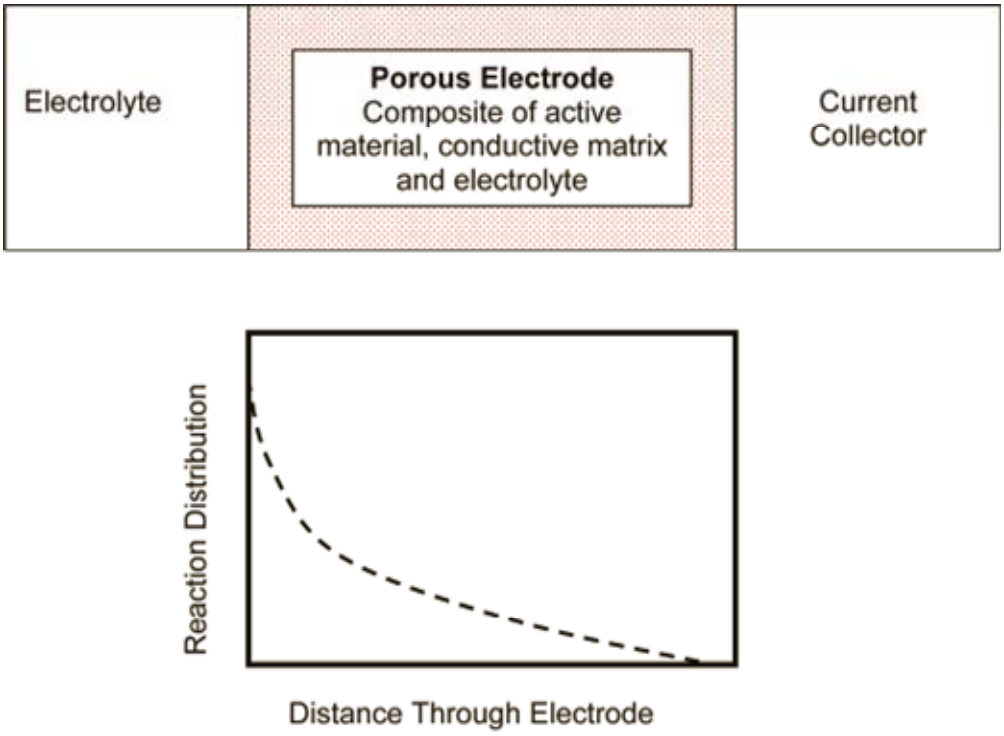

Figure 3.2. Schematic of conventional porous electrode structure and the reaction distribution as a function of distance from the surface of electrode[64].

Therefore, a key challenge is to design novel electrodes in such a way that each component preferably performs more than one function while ensuring the ionic and electronic pathways. This multifunctional or multipurpose approach is even more important for pseudocapacitors as they are designed to deliver and store energy very fast.

In this study, conductive and porous carbon fiber paper (CFP) was used as both the current collector and the electrode (backbone) for thin, conformal coating of nano-porous mixed-valent MnO_x as the active electrode material for pseudocapacitors as shown in Figure 3.3. With the advantages of the tailored architecture of electrodes including (1) efficient ion diffusion between porous carbon fibers, (2) improved electrical contact between manganese oxides and current collectors without any insulating binders, and (3) high surface area of nano-porous manganese oxides, it is hoped that pseudocapacitors constructed from novel MnO_x/CFP composite electrodes will have improved rate capability, enhanced cycling ability and higher specific capacitance.

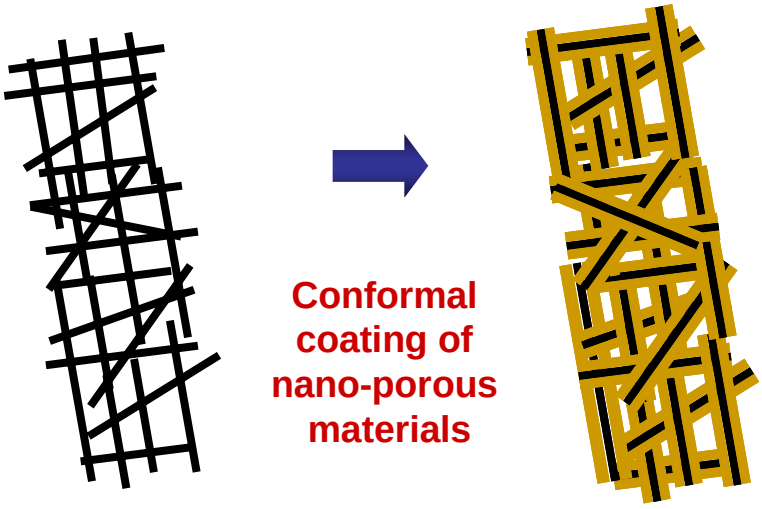

Figure 3.3. Proposed electrode architecture: porous carbon fiber paper before and after thin, conformal and continuous coating of active materials.

3.4. Experimental Methods

Synthesis of novel electrodes. All chemicals were of analytical grade and used without further purification. In a typical synthesis procedure, several pieces of carbon fiber paper (~60 cm^2) were added into 100 ml of 2M sulfuric acid (H_2SO_4 solution), pre-heated to a given temperature (e.g., 65^oC, 75^oC or 85^oC) in a water bath with vigorous magnetic stirring with cool water fluxing in about 30 min. One gram of $KMnO_4$ was subsequently added to the solution which was kept for a predetermined period of time with vigorous stirring. The as-synthesized electrodes were then taken out, ultrasonically cleaned for several times with DI water and ethanol, dried at 80^oC for about an hour, and annealed for 2 hours at different temperatures (200, 350, 400, 450^oC) in different atmospheres (air, N_2, 4% H_2).

Electron microscopy. Scanning electron microscope (SEM Leo/Zeiss 1530) was operated at an accelerating voltage of 3 kV and the high resolution transmission electron microscope (JEOL 4000 EX) was operated at an accelerating voltage of 400kV. For TEM analysis, the MnO_x coated CFP sample was rigorously pestled in a mortar to a fine powder form. The fine powders were dispersed in isopropyl alcohol, and subsequently loaded on a lacey carbon film on a Cu grid.

Synchrotron-based X-ray Diffraction. Synchrotron X-ray diffraction analyses, including glancing angle and time-resolved X-ray diffraction, were carried out with the beamline X14A of the National Synchrotron Light Source (NSLS) at Brookhaven National Laboratory. Diffraction patterns were collected with a high resolution Si strip

detector of 640 pixels, with each pixel corresponding to 0.005°. For in-situ XRD studies, each as-synthesized sample was loaded into a quartz capillary (inner diameter 0.7 mm) of a flow cell and air was admitted into the cell at a rate of 10 mL/min. The resistive heating of the capillary was program-controlled by a temperature controller (Eurotherm 818) and monitored with a 0.5-mm type K thermocouple inside the capillary. Phase identifications were performed using software Jade 6.5 (Materials Data INC).

Other characterization. The thermogravimetric analysis (TGA) was performed in air with heating rate of 25°C/min to determine the weight of the MnO_x loaded to CFP. Typical area of single electrode was 1.98cm^2 and weight of active materials ranged from ~0.32 to 2.8 mg. The thicknesses of the MnO_x coatings were determined from microscopy. Gas adsorption analysis (BELSORP-max, BEL JAPAN, INC) was performed to evaluate the specific surface area (Brunauer-Emmett-Teller, BET), specific pore volumes, average pore size and nitrogen adsorption/desorption isotherm.

3.5. Results and Discussion

Figure 3.4 (a) and (b) shows the SEM images of CFP before coating. Individual carbon fibers in the CFP are well-connected and the pores are sufficiently large to allow efficient ion access to all surface area of the electrode. Without using any insulating binders, a thin, uniform coating of nanostructured MnO_x was directly deposited onto porous CFP using a simple precipitation method in an aqueous solution at 75°C. To achieve conformal coating onto the surface of carbon fibers, the rapid autocatalytic nature of permanganate decomposition under an acidic condition (2M H_2SO_4) was employed[65].

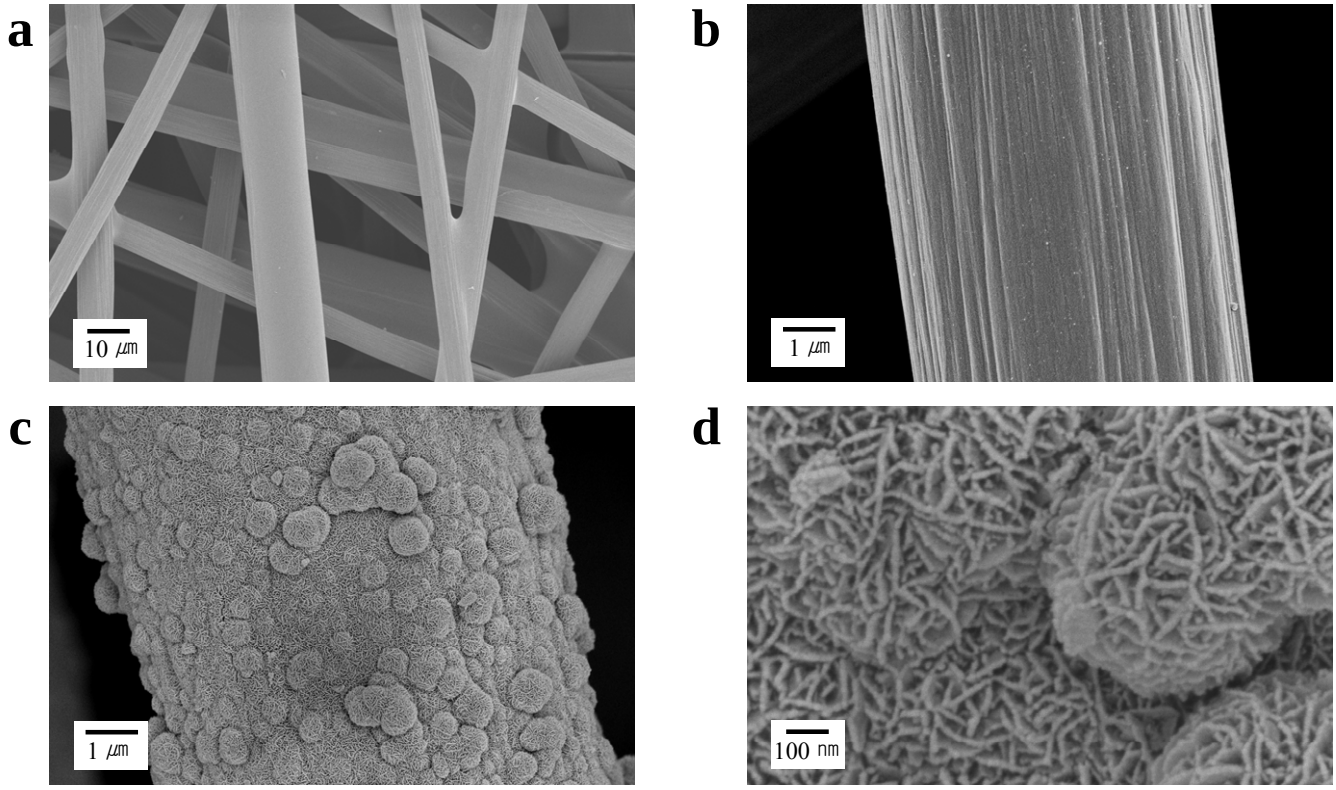

Figure 3.4. a, SEM images of carbon fiber paper (CFP) before coating showing 3D interconnected, porous structures. **b,** SEM image of a carbon fiber before coating. **c,** SEM image of a carbon fiber after conformal coating of MnO_x for 30 minutes. **d,** SEM image of the MnO_x coating annealed at 400^oC in air for 2h.

An SEM image of the electrode after coating deposited at 75^oC for 30 minutes is shown in Figure 3.4 (c). The porous network structure of the CFP is retained because the conformal MnO_x coating is relatively thin, as revealed by microscopy. The cross-sectional SEM image revealed that the MnO_x coatings were uniformly distributed

throughout the electrodes and nanostructured manganese oxides were grown on the carbon fiber (Figure 3.4 d).

The MnO_x coated CFP were then heat-treated at 200 to 450^oC in different atmospheres (air, N_2, and 4% H_2). TEM analysis of the samples annealed at 400^oC in air for 2h revealed that the MnO_x films consist of many low aspect-ratio crystals as well as clustered and needle-shaped crystals, whose diameters vary from a few nm to ~10 nm (Figure 3.5. and 3.6). Figure 3.6 (a) reveals the size of low aspect-ratio particles are in the range of tens of nanometers; in addition, there are many smaller crystals of a few nanometers lit up. The SAED pattern shown in Figure 3.6 (b) shows many discrete and conspicuous diffraction spots, all of which can be indexed with the crystalline α-Mn_2O_3 with a lattice constant of 0.94 nm. The needle-shaped crystals were identified as Mn_3O_4 (Hausmannite) based on lattice images as shown in Figure 3.5 (c) and Figure 3.6 (c). The lattice fringes reveal the axes of the two needle-shaped Mn_3O_4 crystals are parallel to the (101) lattice planes. Since both the (101) and (011) spacing are the largest lattice spacing in the Mn_3O_4 lattice, it is expected that such an orientation may facilitate the incorporation and transport of ions along this direction.

The thickness of MnO_x coating varied from ~70 to ~800 nm (Figure 3.7-3.9) depending on the deposition time (2 to 30 minutes). The cross-sectional views of MnO_x-coated CFP with different loading of MnO_x (by deposition for a period of 2, 5, 15, and 30 minutes) were carefully examined. Shown in Figure 3.7 are some typical TEM (deposition of MnO_x for 2 min) and SEM (deposition of MnO_x for 30 min) images of MnO_x-coated CFP electrodes.

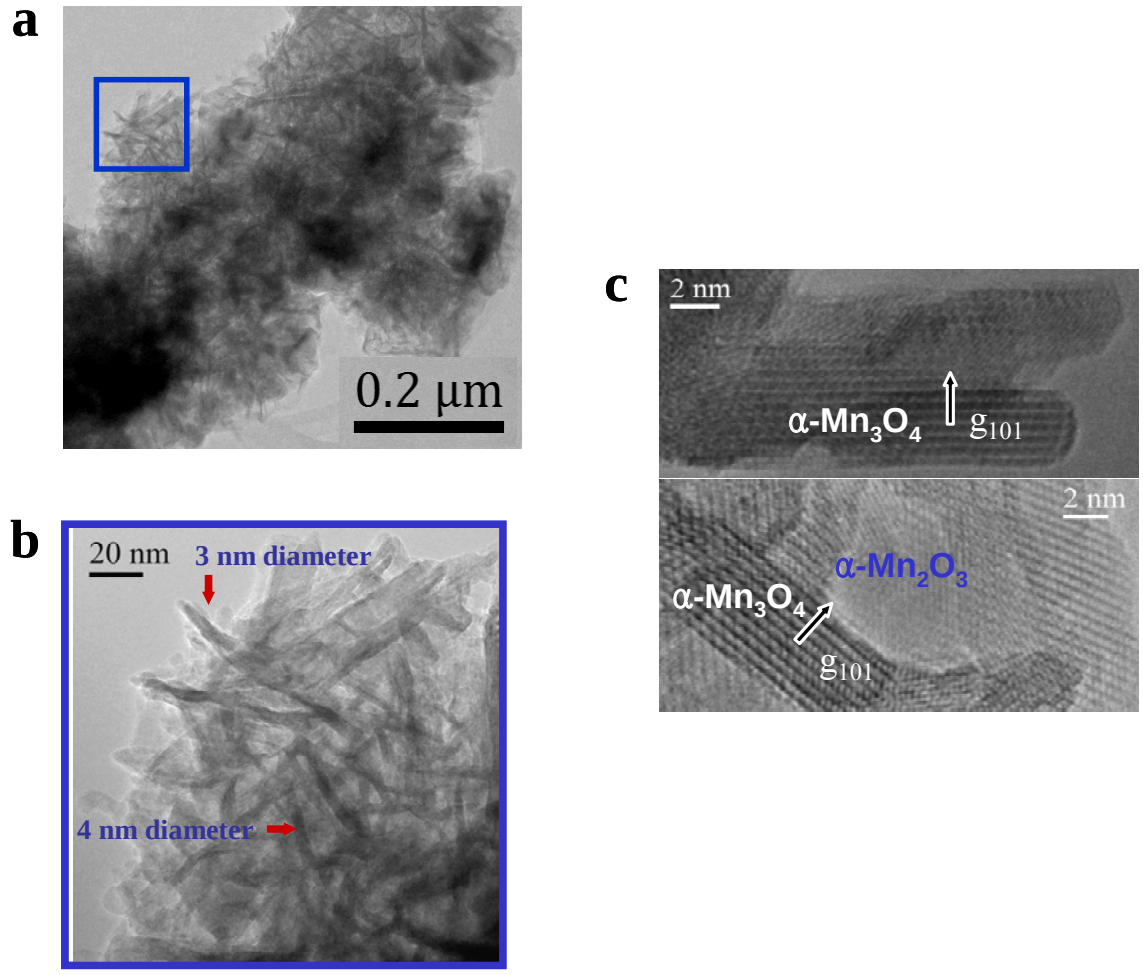

Figure 3.5. a, TEM image of MnO_x coating annealed at 400°C in air for 2 h. **b,** A zoomed-in view of the blue square area in (a) showing a cluster of the needle-shaped crystals with diameters of ~3 to ~4 nm. **c,** High resolution TEM images showing the fringes of Mn_3O_4 and α-Mn_2O_3 phase.

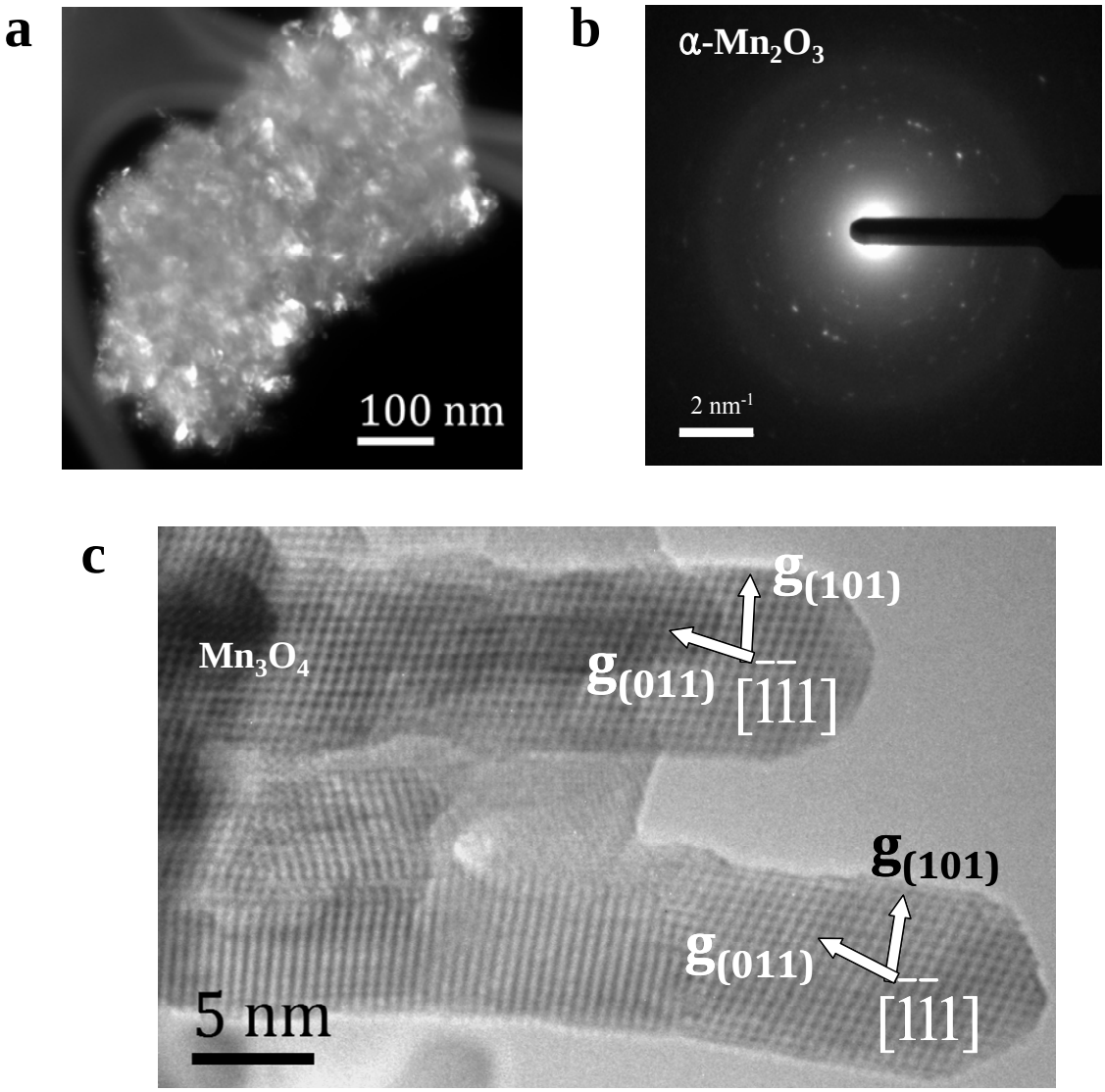

Figure 3.6. a, A dark-field image of a portion of a crushed MnO_x coated CFP after annealing in air at 400°C for 2h. **b,** Selected area electron diffraction (SAED) pattern of the sample shown in (a). **c,** High resolution TEM image showing the $[\bar{1}\bar{1}1]$ zone-axis fringes of two Mn_3O_4 nano-needles, whose diameters are on the order of a few nanometers.

The thicknesses of the MnO_x coatings can be readily seen from these images. Figure 3.7 (a) shows a low-magnification cross-sectional view of a MnO_x coating deposited for 30 minutes on a carbon fiber of 8-10 μm in diameter. The average thickness of the MnO_x coating is ~800 nm. Figure 3.7 (c) reveals the porous structure of the MnO_x coating. For the sample prepared by deposition of MnO_x for 2 min, a very thin coating of porous MnO_x was observed along the perimeter of the carbon fibers, as seen in Figure 3.7 (d); the average thickness was determined to be about 70 nm.

The thermogravimetric analysis (TGA) was employed to determine the total weight of each MnO_x-coated CFP sample (the initial weight of the sample at room temperature after heat-treatment at 400^{o}C for 2 h) and the weight of the MnO_x loaded to CFP (the final weight of the sample above 800^{o}C when all carbon were removed). We repeated the measurements many times and the standard deviation in specific capacitance was ~ 2.8%.

As shown in Figure 3.8 (a), while bare CFP was totally burned out above 800^{o}C, TGA curve of as-synthesized electrode (prepared by deposition of MnO_x for 30 minutes) indicated the weight of remaining MnO_2 is 14.3 wt.% of total electrode. The combustion (i.e. oxidation) of carbon started earlier (at ~530^{o}C) for the as-synthesized sample than for the bare CFP (at ~630^{o}C) due to catalytic combustion caused by manganese oxide. Interestingly, the TGA curve appears quite different for the samples annealed at 400^{o}C in air for 2 h, which led to formation of mixed-valent MnO_x on the CFP. The catalytic combustion of carbon started even earlier (at ~430^{o}C) than the amorphous MnO_2 and showed a two-step oxidation process. The first dramatic weight loss is attributed to the oxidation of thin carbon layer in the proximity to the MnO_x coating.

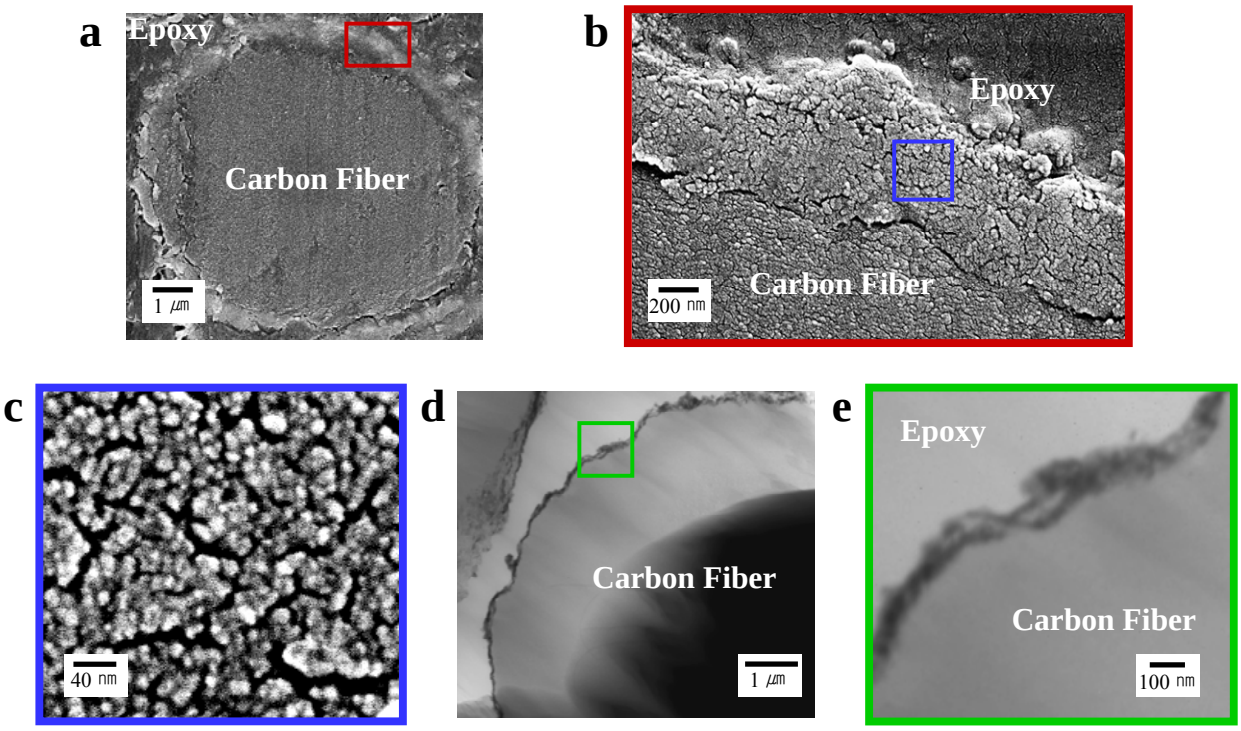

Figure 3.7. a, Cross-sectional SEM image of MnO_x/CFP deposited for 30 minutes, **b,** an enlarged view of the area highlighted with a red rectangle in (a) showing the details of the MnO_x coating, **c,** an enlarged view of the area highlighted with a blue square in (b) showing the porous morphology of the MnO_x layer, **d,** a cross-sectional TEM image of MnO_x/CFP deposited for 2 minutes, **e,** an enlarged view of the area highlighted with a green square in (d) showing the thin MnO_x coating.

The TGA curves of MnO_x/CFP electrode deposited for 2, 5, 15 and 30 minutes are shown in Figure 3.8 (b). The best performance (~3,900 F/g) was achieved with the MnO_x/CFP electrode prepared by deposition of MnO_x for 2 min.

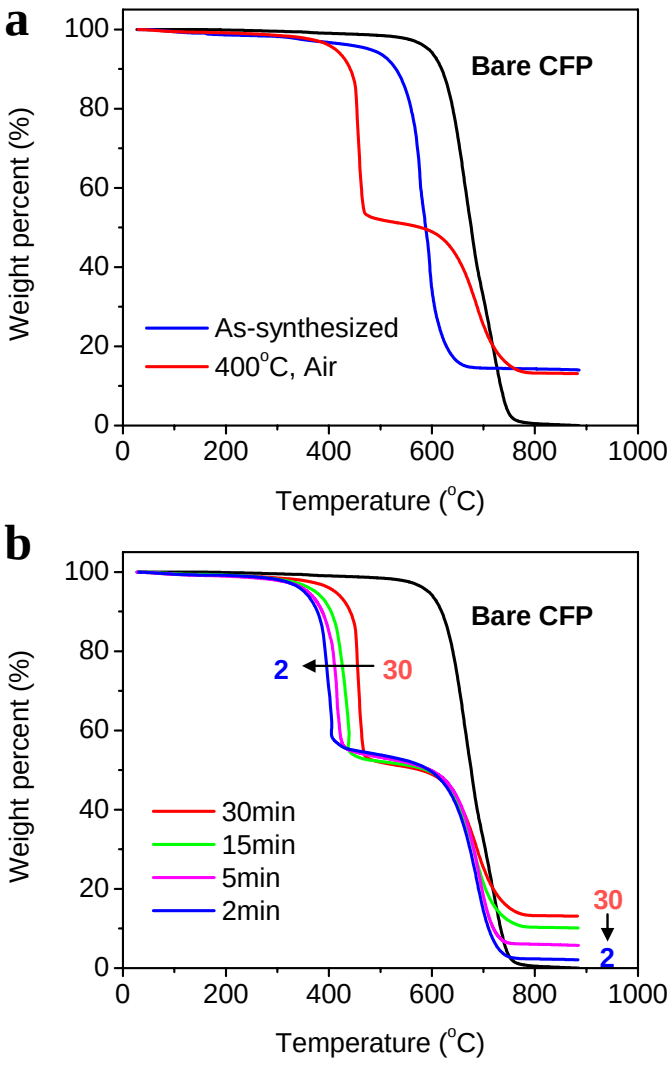

Figure 3.8. a, TGA curves of bare CFP, as-synthesized MnO_2 on CFP, and mixed-valent MnO_x after heat-treatment at 400°C for 2 h. Both samples were prepared by deposition of MnO_x for 30 minutes. **b,** TGA curves of mixed-valent MnO_x deposited for different time (2~30 minutes).

The weight % of MnO_x deposited for 2, 5, 15, and 30 minutes were determined to be ~2.3%, ~4.8%, ~10.3% and ~13.3%, respectively. Accordingly, the loading amount of MnO_x was determined as ~0.16 mg/cm^2 for 2 min's sample and ~1.4 mg/cm^2 for 30 min's samples. The thicknesses of the MnO_x coatings (determined from microscopy), together with the corresponding weights of MnO_x (determined from TGA), are plotted as a function of the deposition time in Figure 3.9.

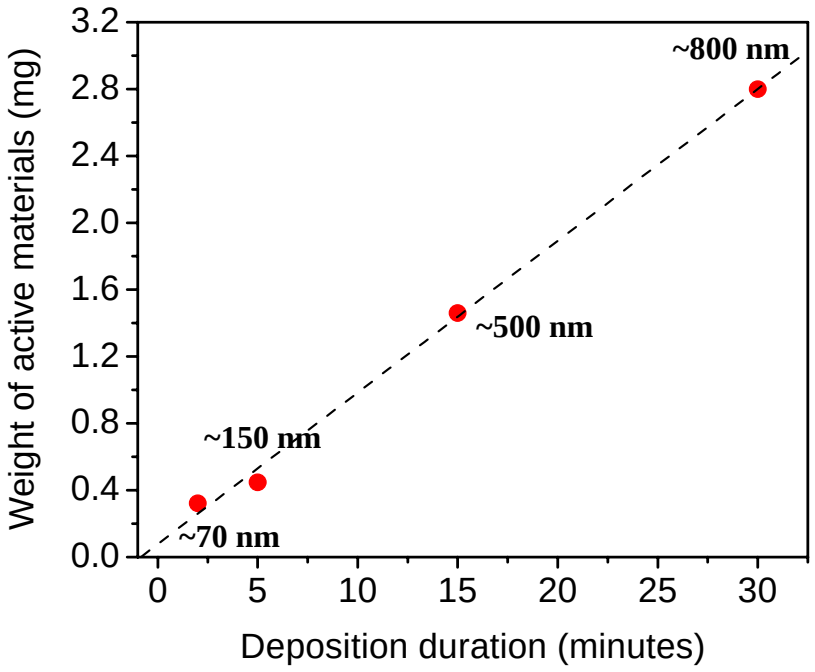

Figure 3.9. The thickness and the weight of the MnO_x coating deposited on each piece of carbon fiber paper (CFP) with a superficial area of ~1.98 cm^2. The weights of MnO_x were determined using TGA whereas the thickness was determined by electron microscopy.

To further characterize the structural features of the MnO_x coatings formed on CFP, both laboratory and synchrotron-based X-ray diffraction (XRD) analysis were used. Figure 3.10 shows the synchrotron-based XRD patterns (transmission mode) of samples (deposited for 30 minutes) before and after annealing in air at different temperatures. The very broad characteristic peaks in the XRD patterns indicated that the as-deposited MnO_2 coating was amorphous and remained so after annealing at 200°C in air for 2h, which is consistent with previous studies under similar synthesis conditions[66,67]. The amorphous phase of MnO_2 has been studied intensively and suggested by other researchers as good candidates for electrode materials for pseudocapacitors[67-69].

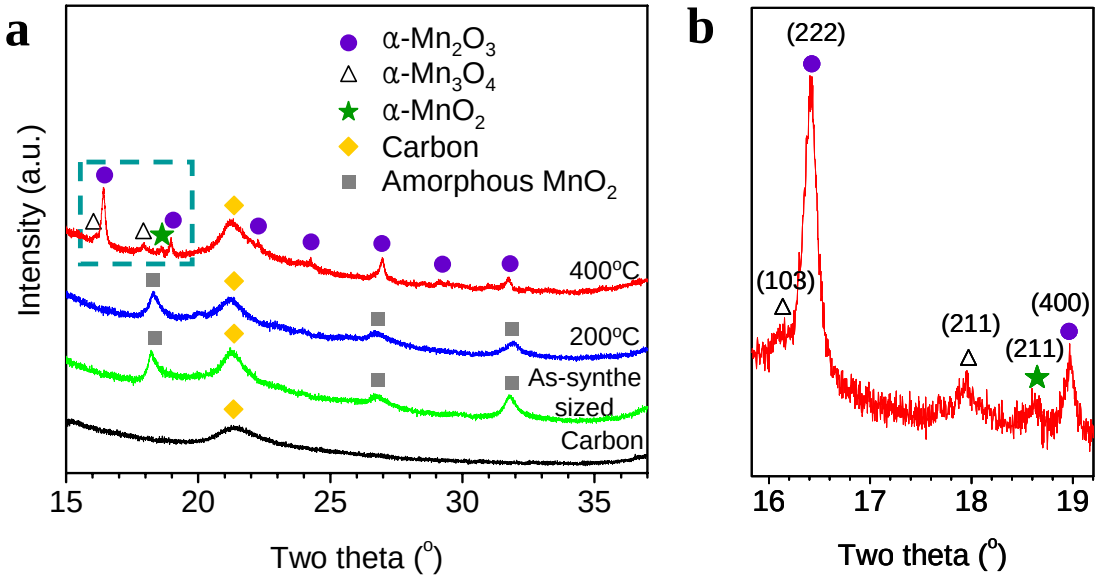

Figure 3.10. a, Synchrotron X-ray diffraction (transmission mode) patterns: bare carbon paper before coating, MnO_x electrodes before and after annealing at different temperatures (200 and 400°C) in air for 2h. **b,** Enlarged view of XRD pattern between 16~19° of XRD pattern of MnO_x annealed at 400°C in air for 2h and highlighted in (a).

When annealed with CFP at 400°C in air for 2h, the amorphous MnO_2 was converted to crystalline α-Mn_2O_3 with small amount of Mn_3O_4 (Hausmannite) and α-MnO_2, as evident from the XRD patterns shown in Figure 3.10 (a) and (b). These crystalline phases started to appear at ~360°C when the temperature was raised from 200 to 400°C in air, as revealed by the *in situ* XRD analysis (Figure 3.11).

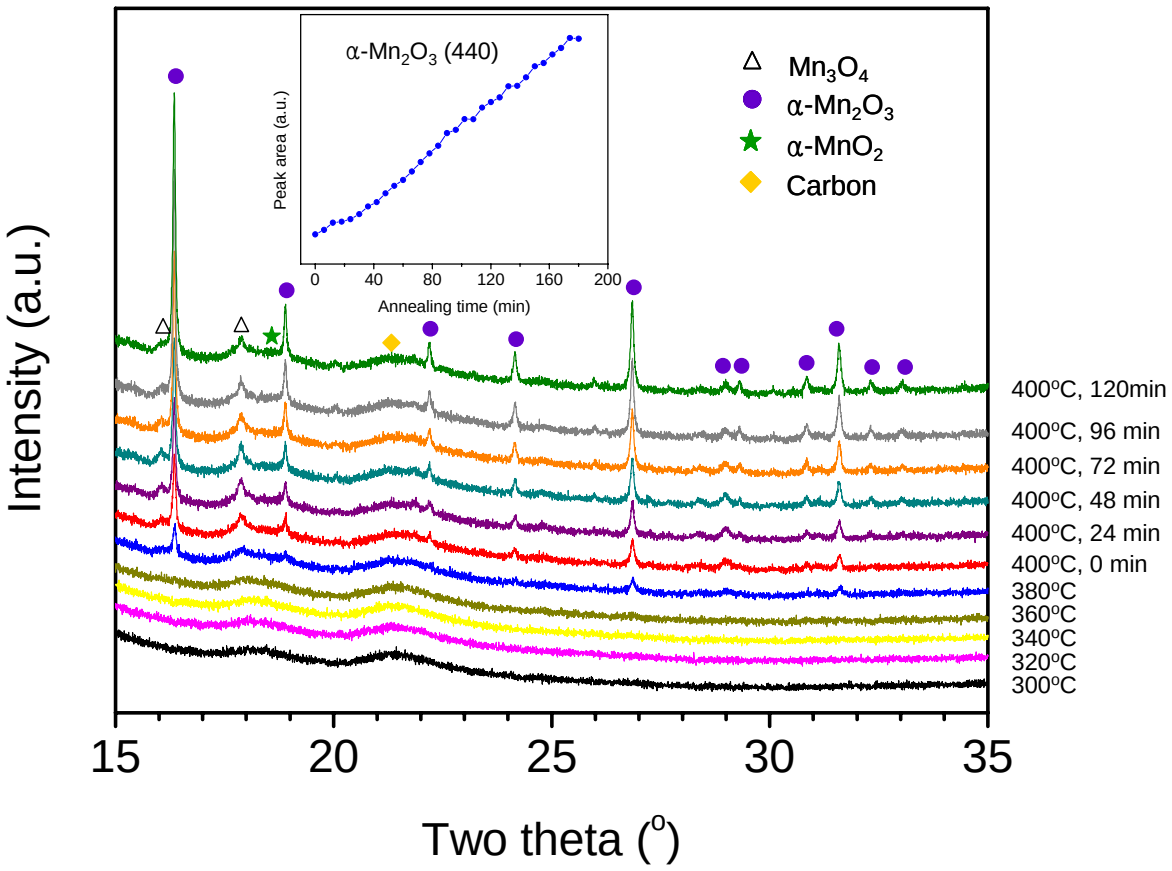

Figure 3.11. *In-situ* synchrotron-based XRD patterns (transmission mode) of MnO_x coating measured at different temperatures and annealing times.

The patterns reveal that small crystalline phases started to form above 360°C. At 400°C, sharp peaks of crystalline α-Mn_2O_3 appeared with small amounts of Mn_3O_4 and α-MnO_2. The α-Mn_2O_3 peak intensities grow with annealing time as shown in the insert, indicating that the volume fraction of the phase increased with annealing time. In contrast, the intensities of the Mn_3O_4 peaks decreased slightly with annealing time at 400°C. It is noted, however, that the transmission-mode XRD pattern is quite different from those collected at a small glancing angle (Figure 3.12), suggesting that the phases on the surface are very different from those in the bulk.

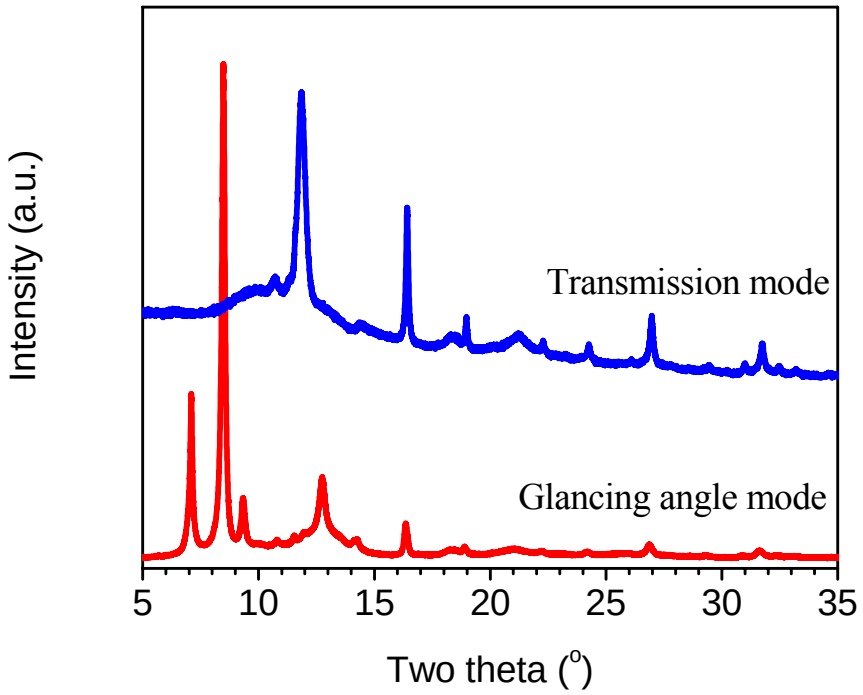

Figure 3.12. Synchrotron-XRD patterns of MnO_x deposited for 30 minutes and annealed at 400°C in air for 2h. The differences between the patterns acquired in a transmission mode and a glancing angle (0.1°) mode suggest that the phases on the surface are very different from those in the bulk.

To gain some insights into the structures of the surface layer, XRD patterns at different glancing incident angles were collected (Figure 3.13). A lower incident angle corresponds to a shallower penetration depth of the X-ray, allowing us to probe the structure of a layer closer to the surface.

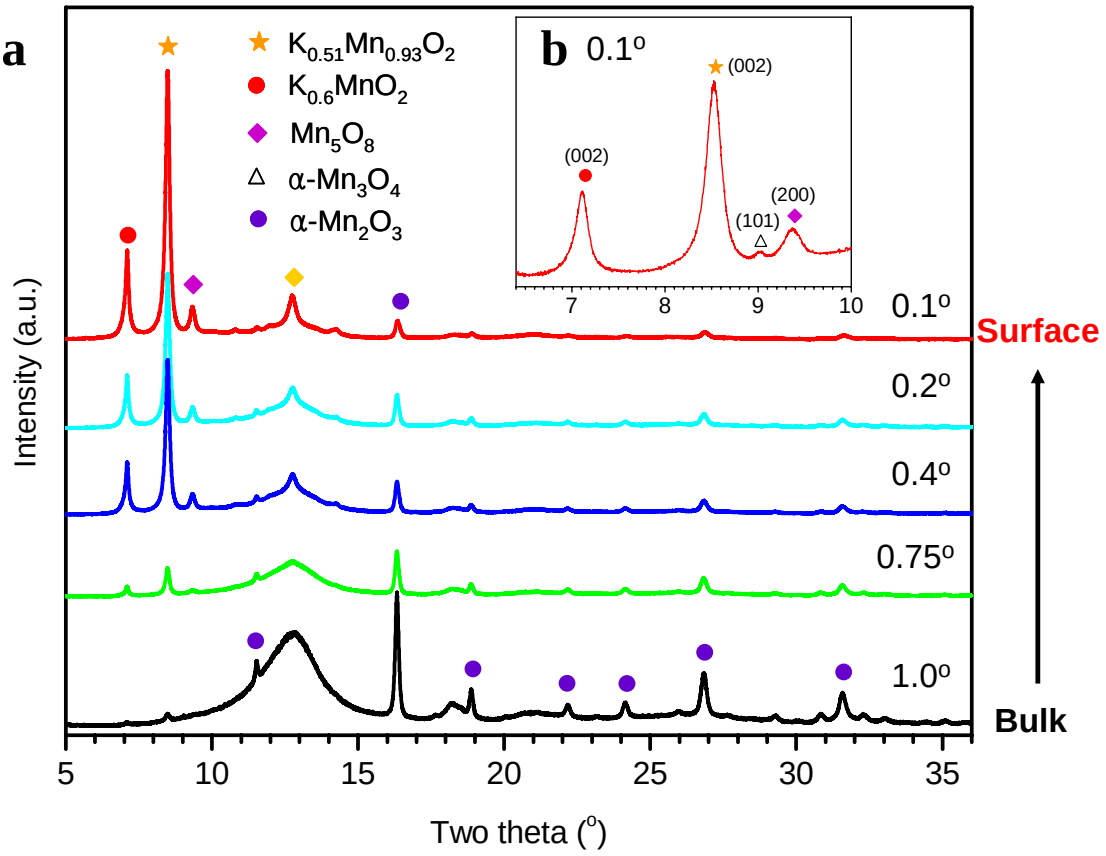

Figure 3.13. a, XRD pattern at of MnO_x annealed at 400°C in air for 2h measured at different incident angle (0.1~1°). **b,** XRD pattern at incident glancing angle of 0.1° of MnO_x annealed at 400°C in air for 2h showing the representative surface species.

When the incident angle was varied from 1 to 0.1°, the α-Mn_2O_3 peaks decreased gradually while the peaks corresponding to K-incorporated MnO_2 ($K_{0.6}MnO_2$ and $K_{0.51}Mn_{0.93}O_2$) and Mn_5O_8 increased considerably, suggesting that α-Mn_2O_3 is present predominantly in the bulk whereas the K-incorporated MnO_2 and Mn_5O_8 are formed mostly near the surface (Figure 3.13 b). It is noted that small peaks corresponding to Mn_3O_4 were observable in both transmission-mode and glancing angle mode XRD patterns, implying that small amount of Mn_3O_4 is present in the bulk and on the surface. This is consistent with TEM observation (Figure 3.5 and 3.6). The surface phases (K-incorporated MnO_2, Mn_5O_8, and Mn_3O_4,) were formed at 400°C, as indicated by the low glancing angle XRD analysis at different temperatures (Figure 3.14).

More careful analysis using synchrotron XRD (transmission mode) was performed on the mixed-valent MnO_x with different loading. While Mn_2O_3 was identified as the predominating phase of the MnO_x deposited for 30 minutes, the predominant phase of the mixed-valent MnO_x prepared for 2 minutes was Mn_3O_4, which showed the best performance. As the thickness was reduced (Figure 3.15), the predominating "bulk" phase was changed from α-Mn_2O_3 to a phase similar to Mn_3O_4. This is anticipated because the degree of MnO_x reduction (by the carbon substrate) decreases in the direction away from the carbon substrate surface, considering that the sample was exposed to air.

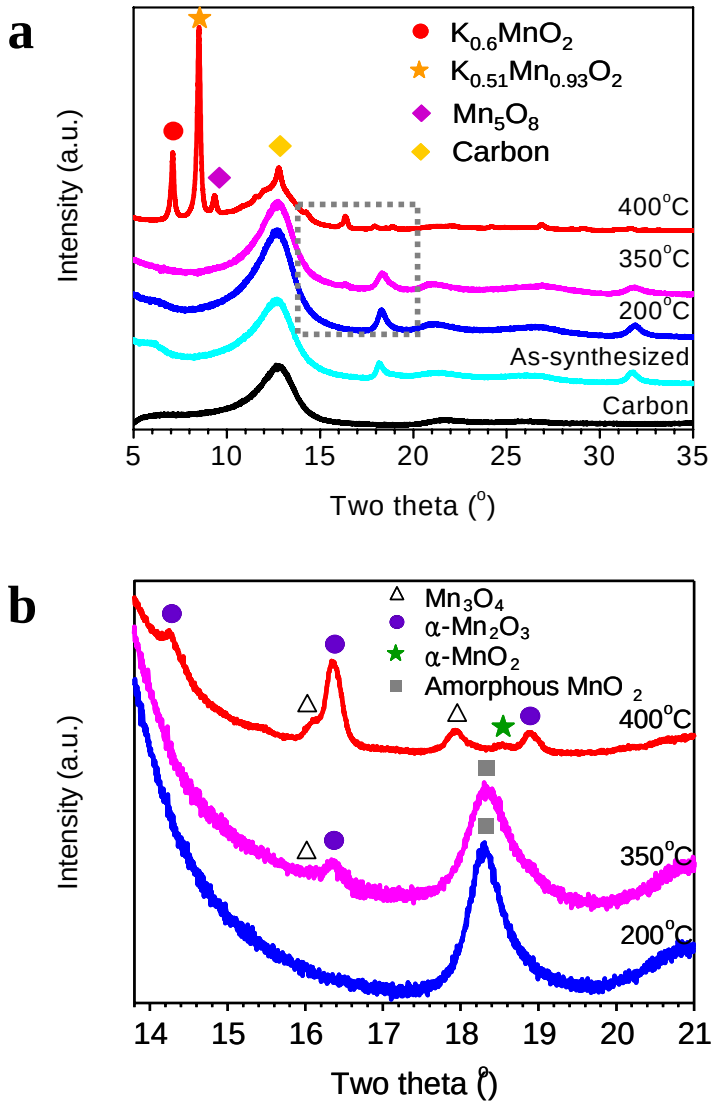

Figure 3.14. a, Synchrotron-XRD patterns acquired at an incident glancing angle of 0.2° for different samples of carbon, as-coated electrode, and coated electrode annealed at different temperatures in air for 2h. It appears that the surface phases (K-incorporated MnO_2, Mn_5O_8, and Mn_3O_4,) were formed at ~400°C. **b,** Enlarged view of the XRD pattern in the range of 14~21° as highlighted in (a), confirming that crystalline α-Mn_2O_3 appeared at ~400°C with small amounts of Mn_3O_4 and α-MnO_2. Also, it is noted that small α-Mn_2O_3 peaks started to appear at 350°C.

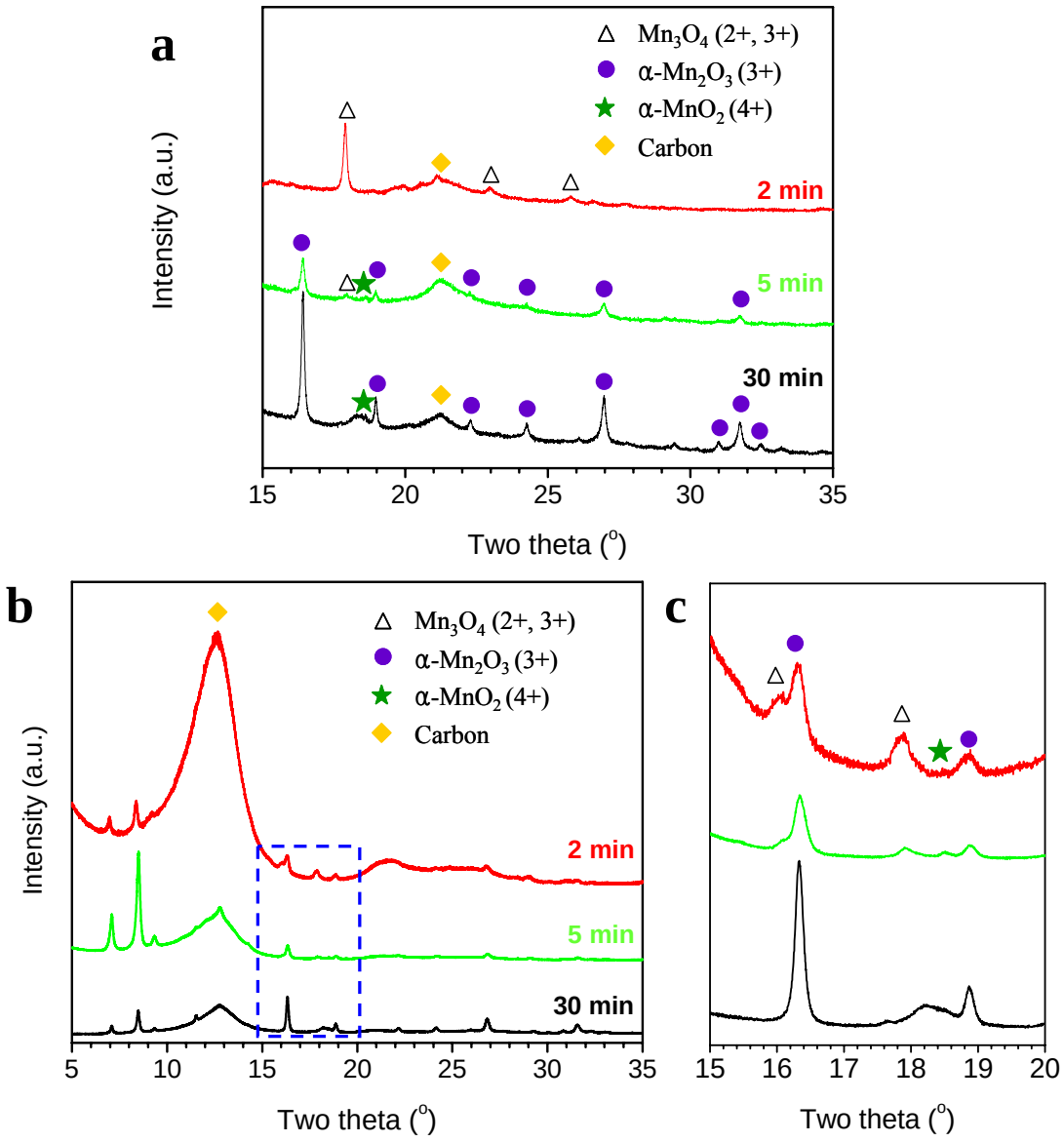

Figure 3.15. Synchrotron X-ray diffraction (XRD) analysis. **a,** Transmission mode XRD pattern of MnO_x electrodes deposited for 2, 5, and 30 minutes followed by annealing at 400°C in air for 2h. **b,** Glancing angle mode (0.2°) XRD pattern of MnO_x electrodes deposited for 2, 5, and 30 minutes followed by annealing at 400°C in air for 2h, **c,** Enlarged view of XRD pattern between 15~20° of XRD pattern of MnO_x highlighted in b.

The annealing condition created a gradient in oxidation state of Mn ion along the thickness direction; thinner MnO_x films deposited on carbon fiber were more reduced. However, they were still mixed-valent MnO_x and there is more Mn_3O_4 phase in a thinner film as shown in Figure 3.15-3.16. It is noted that all electrodes deposited for 2, 5, 15 and 30 minutes have the same surface phases; the graded oxidation state remained largely the same.

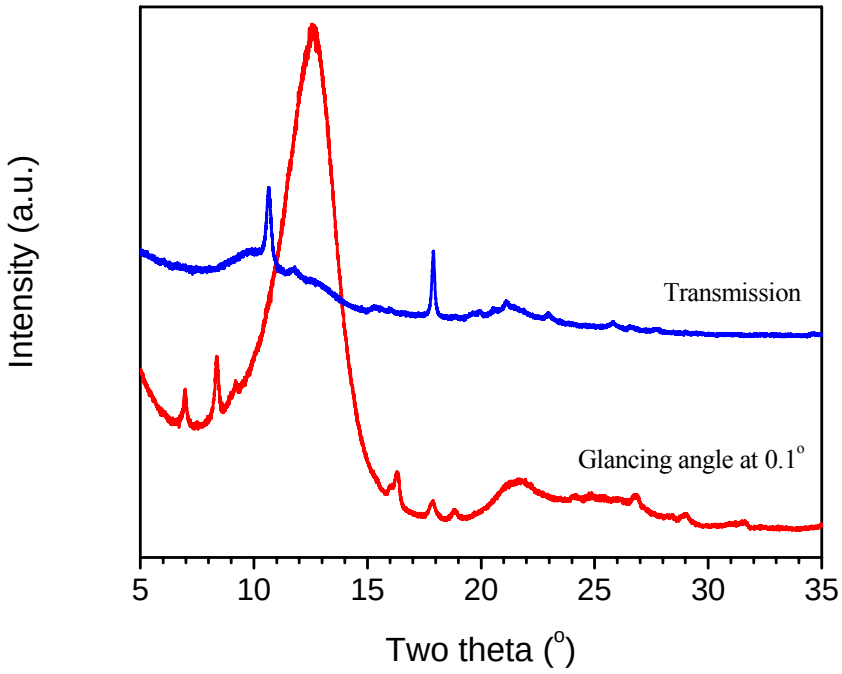

Figure 3.16. Synchrotron-XRD patterns of MnO_x deposited for 2 minutes and annealed at 400°C in air for 2h. The differences between the patterns acquired in a transmission mode and a glancing angle (0.1°) mode suggest that the phases on the surface are very different from those in the bulk.

Gas adsorption/desorption analysis implied that the microstructure of MnO_x underwent a dramatic rearrangement during the annealing process, producing porous, nano-structured MnO_x (Figure 3.17). The specific surface area increased from 5.21 m^2/g for amorphous MnO_2 to 261.8 m^2/g for the multi-valent $MnO_{x,}$ as the pore volume increased from 0.021 to 0.149 cm^3/g at the same time. The formation of tunneled structure of K-incorporated MnO_2 on the surface may partially account for enlarged surface area and pore volume[49,70]. The porous, nanostructured multi-valent MnO_x is ideally suited for fast mass and charge transfer associated with energy storage processes.

To get more quantitative information about porosity and to see whether the pores are interconnected, cross-sectional SEM image of MnO_x-coated CFP (annealed at 400^oC for 2 h in air) were obtained and quantitative analysis of the microstructures were performed. The image shown in Figure 3.18 (a) clearly reveals that the pores are open and well interconnected, allowing electrolyte to penetrate through the MnO_x films and make good use of surface sites. Quantitative analysis on the cross-sectional SEM image of MnO_x film using image analysis software (Scanning Probe Image Processor, Version 4.3.4.0, from Image Metrology) offered quantitative information about porosity. After image processing to separate the pores from MnO_x electrode, the area fraction of pores in the 2D cross-sectional image of MnO_x film was estimated to be 13.2%. It should be noted that this image analysis can include only the pores which can be resolved by SEM. Many nano-pores/channels (e.g., as revealed by TEM images shown in Figure 3.6) can not been counted here, but make important contributions to the enhanced capacitance. This image analysis confirmed the porous features of MnO_x electrode, although the actual porosity could be much higher.

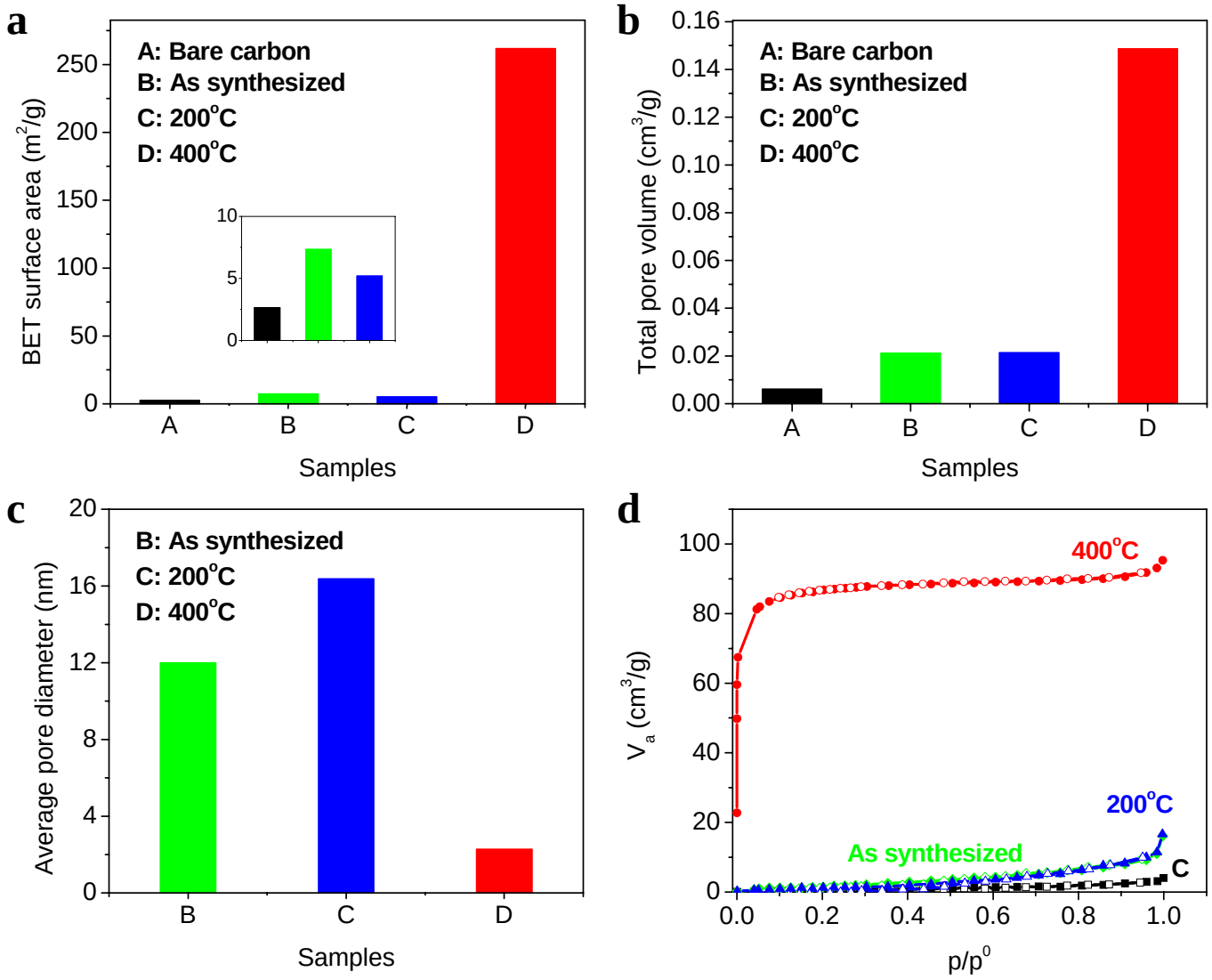

Figure 3.17. Gas adsorption/desorption analysis of carbon, as-synthesized MnO_x sample, and MnO_x samples annealed at 200 and 400°C in air for 2h. **a,** BET surface areas, **b,** Total pore volumes, **c,** Average pore diameters, and **d,** Nitrogen adsorption/desorption isotherm. These results suggest that the microstructure of the MnO_x underwent a dramatic rearrangement during annealing at 400°C in air for 2h, producing porous, nano-structured multi-valent MnO_x.

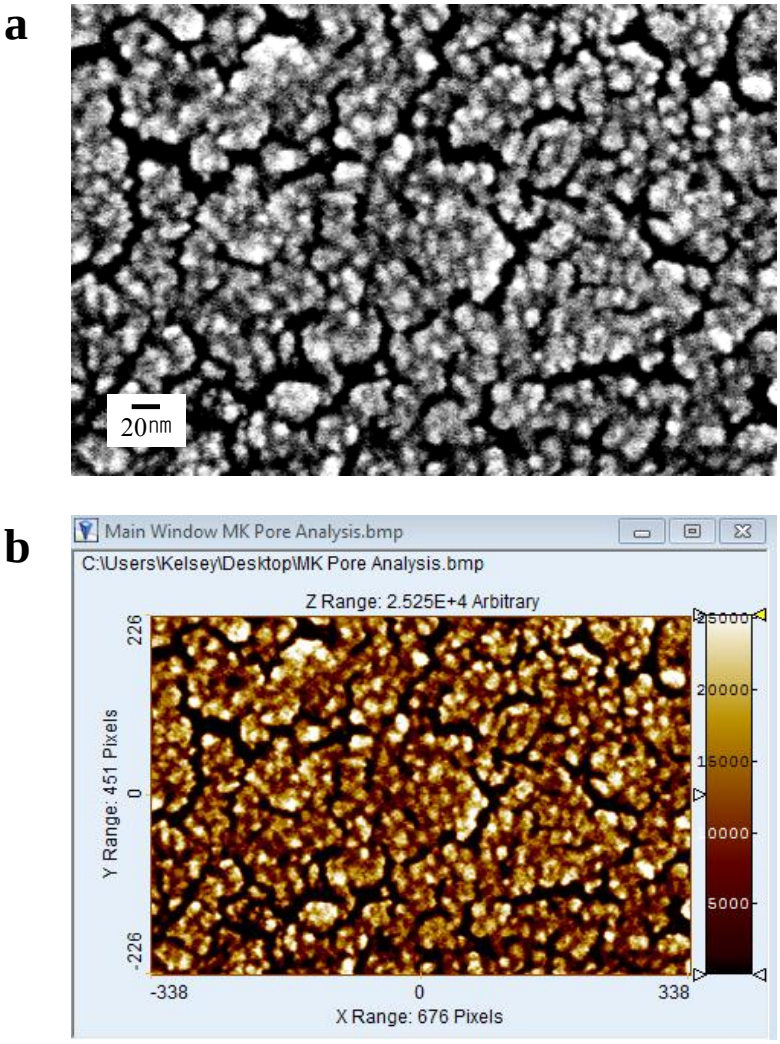

Figure 3.18. a, a cross-sectional SEM image of MnO_x/CFP deposited for 30 minutes, **b,** processed image by a software (Scanning Probe Image Processor, Version 4.3.4.0, from Image Metrology) to separate the pores (black area) from the electrode.

3.6. Summary

In this chapter, nanostructured mixed-valent manganese oxides were successfully deposited onto porous CFP using a simple precipitation method in an aqueous solution at low temperature (75^{o}C) followed by a controlled annealing process to obtain the desired composition and microstructure.

Synchrotron-based X-ray diffraction and advanced electron microscopy were used to characterize the unique structural features of mixed-valent manganese oxides. The thickness of the MnO_x coating varied from ~70 to ~800 nm, depending on the deposition time (2 to 30 minutes). It was demonstrated that when annealed with CFP at 400^{o}C in air for 2h, the amorphous MnO_2 was converted to crystalline α-Mn_2O_3 with small amounts of Mn_3O_4 and α-MnO_2. Also, the phases on the surface were found to be very different from those in the bulk. Low glancing angle XRD analysis at different temperatures showed that the surface phases (K-incorporated MnO_2, Mn_5O_8, and Mn_3O_4,) were formed at 400^{o}C. While Mn_2O_3 was identified as the predominant phase of the MnO_x deposited for 30 minutes, the predominant phase of the mixed-valent MnO_x prepared for 2 minutes was determined to be Mn_3O_4.

Gas adsorption/desorption analysis showed that the microstructure of MnO_x was dramatically rearranged during the annealing process, producing porous, nano-structured MnO_x. The unique mixed-valent (2+, 3+, and 4+) manganese oxides with porous nano-architecture are ideally suited for fast mass and charge transfer associated with energy storage processes.

CHAPTER 4

ELECTROCHEMICAL PEROFRMANCE OF NANOSTRUCTURED MIXED-VALENT MANGANESE OXIDES

In the previous chapter, controlled synthesis of nanoscale, conformal and continuous coating of mixed-valent manganese oxides was demonstrated and their structural features were discussed in detail. In this section, the performance characteristics of pseudocapacitors fabricated based on mixed-valent MnO_x/CFP composites are established and their unique electrochemical properties are determined using various electrochemical characterization techniques. The effects of different cations on performance are also discussed.

4.1. Experimental Methods

4.1.1. Fabrication of Symmetric Pseudocapacitors

To evaluate the electrochemical performance of the mixed-valent MnO_x, symmetric-type pseudocapacitors were assembled using lab-made button cells made of stainless steel (SUS316L) as shown in Figure 4.1. Two identical MnO_x/CFP composite were used as electrodes, separated by porous glass microfiber filter paper (GF/D grade). Typical area of single electrode was 1.98cm^2 and weight of active materials (MnO_x) ranged from ~0.32 to ~2.8 mg. The electrolyte (1M Na_2SO_4, 1M $Ca(NO_3)_2$, or 1M H_2SO_4) was then added into the cells, followed by tightening the cell with Nylon clamp. To ensure good electrical contact and uniform pressure, a metal spring (Belleville washer, SUS304) and a spacer were inserted into the cell.

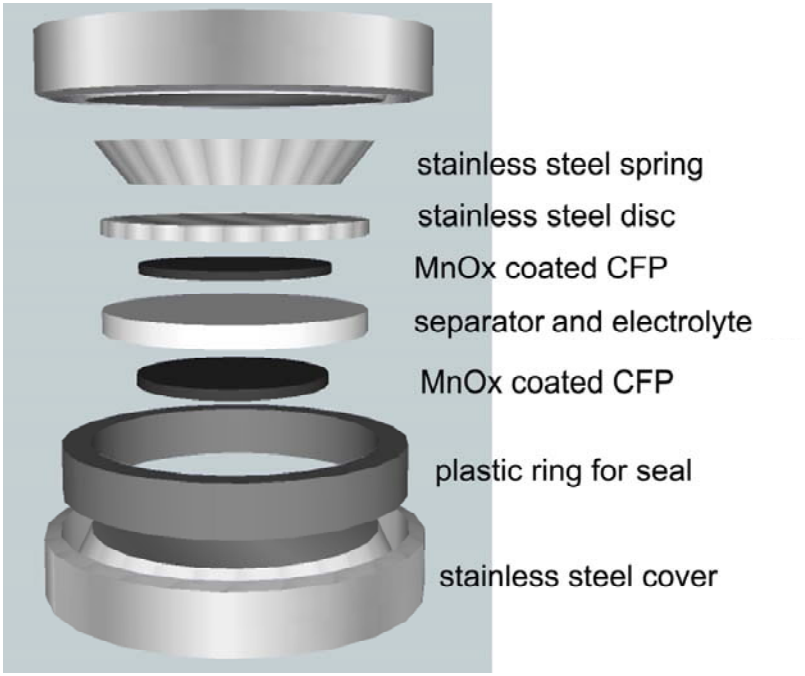

Figure 4.1. Schematic of lab-made symmetric pseudocapacitors based on nanostructured, mixed-valent MnO_x conformally deposited on CFP.

4.1.2. Electrochemical Characterization

Cyclic voltammetry (CV) curves and galvanostatic charge-discharge curves were recorded at room temperature in a symmetric-cell configuration containing different (1M Na_2SO_4, 1M $Ca(NO_3)_2$, or 1M H_2SO_4) electrolyte solution. The potential and current were controlled by an Electrochemical Interface (Solartron, SI 1286) and the electrochemical impedance spectroscopy (EIS) analysis was conducted using a Frequency Response Analyzer (Solartron SI 1255) and SI 1286 with an applied ac voltage of 10 mV in the frequency range of 0.001 Hz to 1 MHz.

The cell capacitance was calculated from the slope of the discharge curve from equation 4.1:

$$C = \frac{A}{\left(\frac{dV}{dt}\right)} \qquad (4.1)$$

where C is the capacitance of symmetric cell in Farad (F), I the discharge current in Ampere (A) and dV/dt the slope of the discharge curve in Volts per second (V/s).

The specific capacitance of active material (F/g) per single electrode is related to the capacitance of the symmetric cell, C, by:

$$C_{m,AM} = \frac{2C}{m_{AM}} \qquad (4.2)$$

where m_{AM} is the weight (g) of the active material (MnO_x).

4.2. Enhanced Pseudocapacitance of Mixed-Valent MnO_x electrodes

To evaluate the characteristic behavior of the mixed-valent MnO_x electrodes for electrical energy storage, several electrochemical measurements were performed in a 1M Na_2SO_4 solution. The mixed-valent MnO_x electrode showed excellent "square-shape" cyclic voltammograms at 50 mV/sec (Figure 4.2), with current densities being almost one order of magnitude higher than those of the amorphous MnO_2 electrode. The symmetric shape and the instant response upon the reversal of voltage indicate that surface reactions are highly reversible and very fast. It is noted that the contribution of the porous carbon fiber substrate to the capacitance is negligible.

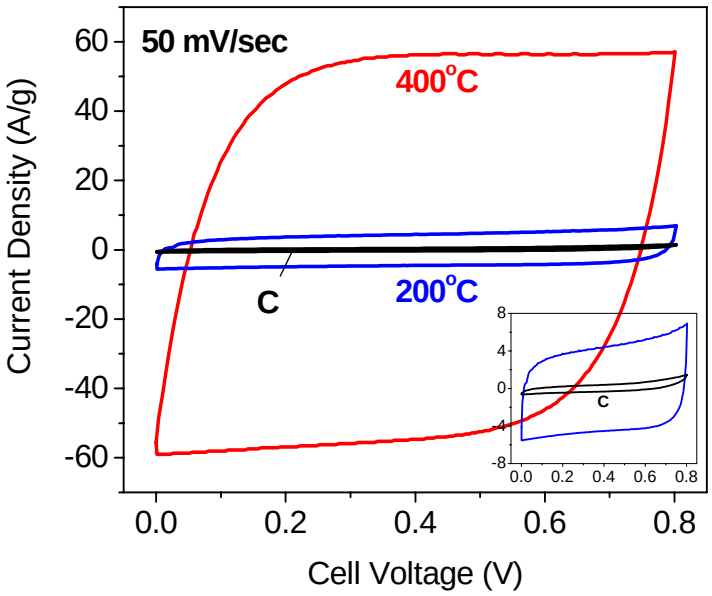

Figure 4.2. Electrochemical performance of symmetric pseudocapacitors constructed from amorphous MnO_2 and mixed-valent MnO_x electrodes. Cyclic voltammograms were measured between 0~0.8V at a scan rate of 50mV/sec.

The iR drops of the electrochemical capacitors were also measured when the potentials were reversed (Figure 4.3) and plotted as a function of applied current densities in Figure 4.4 (a). The slopes of the plots correspond directly to the equivalent series resistances (ESR) of the capacitors. This internal resistance critically influences the power density (or rate capability) of electrochemical capacitors. In general, low capacitance and deviation from ideal capacitor behavior are usually associated with large ESR. It is clearly shown that the mixed-valent MnO_x displayed much smaller ESR than the amorphous MnO_2 at a given current density, due most likely to enhanced rates of the surface redox reactions.

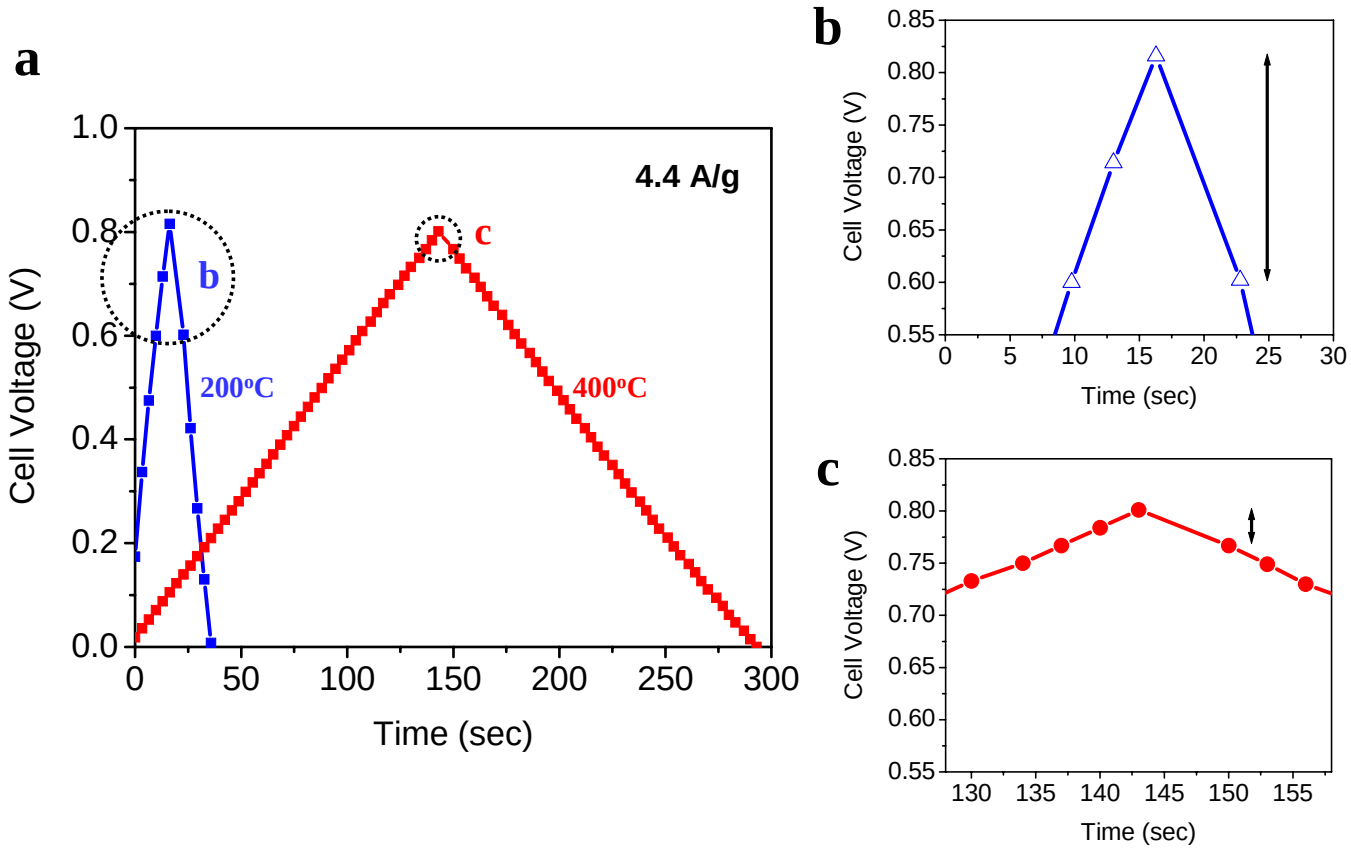

Figure 4.3. a, Typical charge-discharge curves of symmetric pseudocapacitors constructed from amorphous MnO_2 and mixed-valent MnO_x electrodes at a constant current of 4.4 A/g. **b,** Enlarged views of iR drop of amorphous MnO_2 highlighted in (a). **c,** Enlarged views of iR drop mixed-valent MnO_x electrodes highlighted in (a).

This observation was further confirmed by the impedance measurements as shown in Figure 4.4 (b). The charge-transfer resistance (the diameter of the semicircle in the impedance spectrum) of the mixed-valent MnO_x was much smaller than that of the amorphous MnO_2. The long tail at low frequencies of the mixed-valent MnO_x is closer to a vertical line for an ideal capacitor, another indication that the mixed-valent MnO_x has higher capacitance and lower resistance than the amorphous MnO_2.

Typical charge-discharge curves at a constant current of 0.61 A/g are shown in Figure 4.5 (a). The "linear" and symmetrical charge-discharge curves indicate again high coulombic efficiency or excellent reversibility. When calculated from the discharge curve in Figure 4.5 (a), the specific capacitance of the amorphous MnO_2 was 333 F/g, comparable to the values reported in the literatures[67,71]. In contrast, shown in Figure 4.5 (b), the specific capacitance for the mixed-valent MnO_x electrode was ~2,534 F/g, almost eight times higher than that of the amorphous MnO_2.

Because high rate capability is the most important feature of electrochemical capacitors, the performance was measured at very high cycling rates. Typically, the capacitance of a pseudocapacitor may decrease with operating current density due to mass transport limitations, especially when insertion (or removal) of ions into (or from) the electrode sub-surface is involved. Surprisingly, however, the capacitance of the mixed-valent MnO_x was not kinetically limited even at very high cycling rates (Figure 4.5 and 4.6), demonstrating 2,425 F/g at 122.7 A/g.

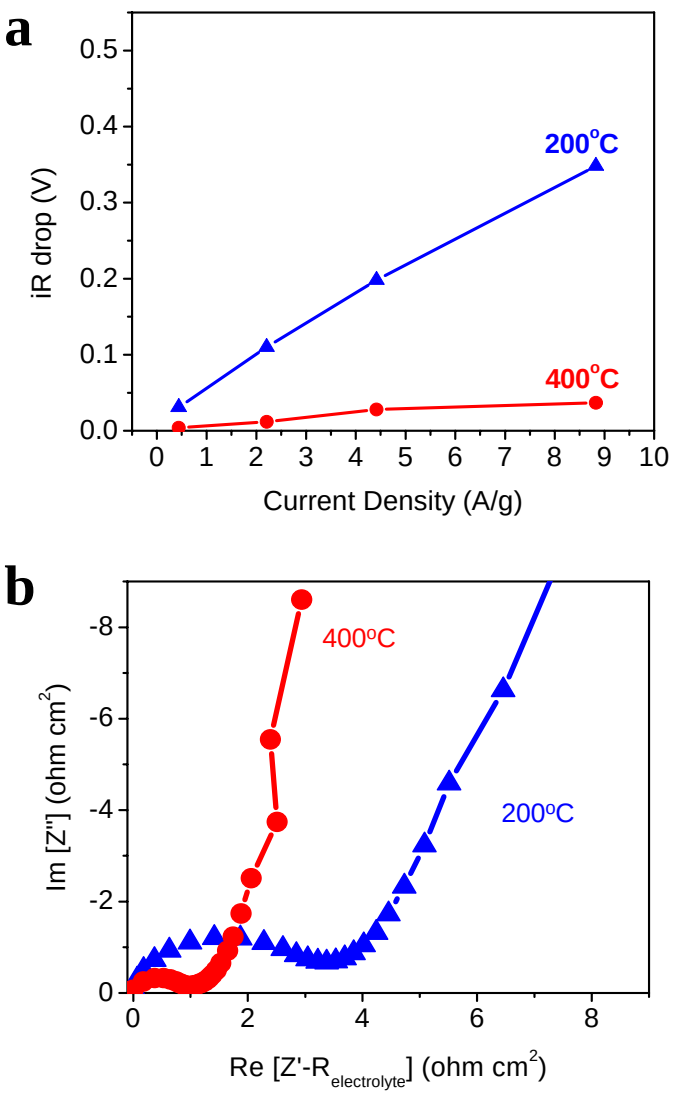

Figure 4.4. a, iR drop of the cells measured at different current densities. **b,** Electrochemical impedance spectra collected at open circuit voltage (OCV) under the influence of an ac voltage of 10 mV.

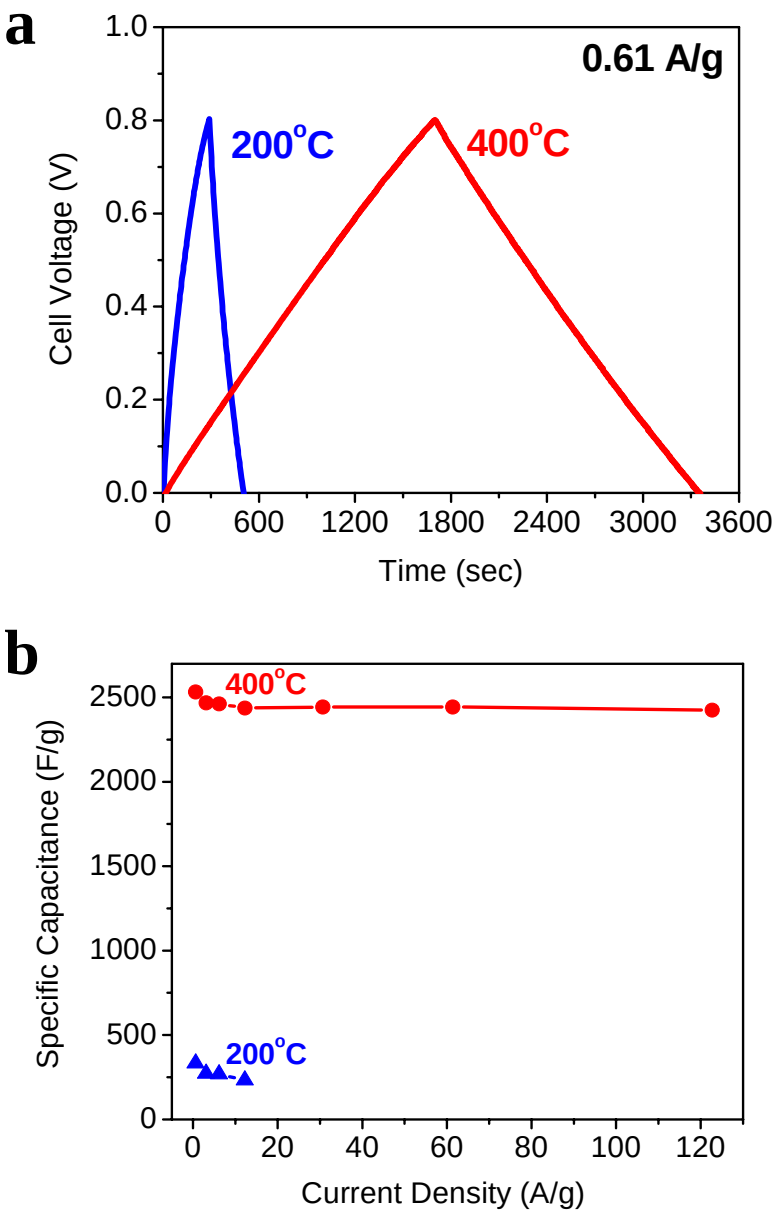

Figure 4.5. a, Typical charge-discharge curves of amorphous MnO_2 and mixed-valent MnO_x electrodes at a constant current density of 0.61A/g. **b,** Specific capacitance at different current densities demonstrating superior rate-capability.

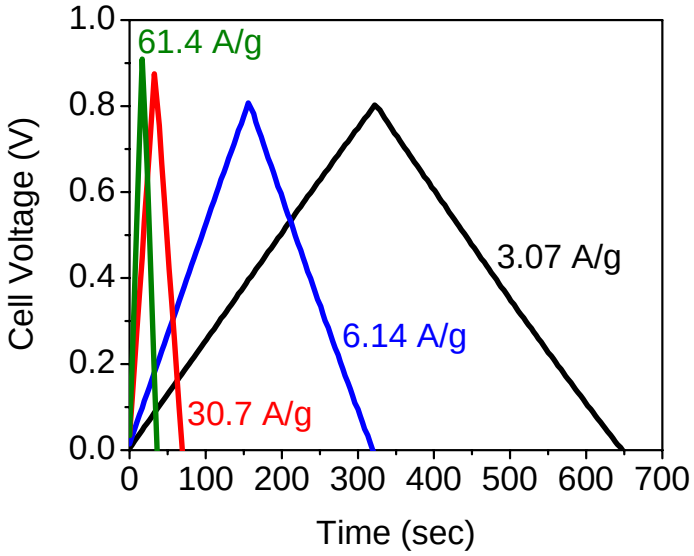

Figure 4.6. Typical charge-discharge curves of symmetric pseudocapacitors constructed from mixed-valent MnO_x electrodes with Na^+ at different constant currents. The "linear" and symmetrical charge-discharge curves imply that surface reactions are highly reversible and very fast.

The superior rate-capability can be attributed to (1) high surface area of the nanostructured manganese oxides, and (2) more facile redox reactions promoted by the presence of mixed phase MnO_x, (3) improved electrical contacts between manganese oxides and current collectors (without any insulating binders), and (4) the efficient ion diffusion within the pores of the electrode.

While the measured currents (A) increased with the loading of MnO_x, the highest specific capacitance was achieved with a coating of ~70 nm thick, implying that the nano-porous surface phases make dominating contributions to the observed capacitance. In Figure 4.7, the potential was measured versus a Saturated Calomel Electrode (SCE)

and the measured currents (A), not the normalized current with respect to the loading amount of MnO_x (A/g), are presented. The mixed-valent MnO_x/CFP electrode with different loadings of MnO_x all showed excellent "square-shape" cyclic voltammograms at 50 mV/sec in 1M Na_2SO_4 solution. The measured currents (A) increased with the loading of MnO_x. For instance, at 0.4V (vs. SCE), the measured current (A) of MnO_x deposited for 5, 15, and 30 minutes showed the 10.7%, 26.9% and 40.9% increase, compared to current (A) from MnO_x deposited for 2 minutes. It is noted that even the sample with the thickest MnO_x coating (deposition of MnO_x for 30 minutes) showed symmetric shape and instant response upon the reversal of voltage, indicating that surface reactions are highly reversible and very fast as shown in Figure 4.8.

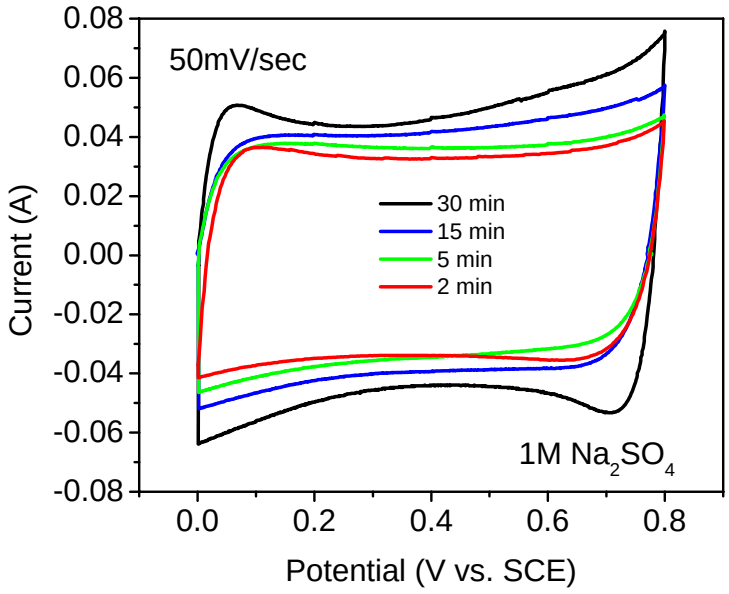

Figure 4.7. Cyclic voltammograms of mixed-valent MnO_x/CFP composite electrodes with different loading amounts of manganese oxide tested in cells with a three-electrode configuration.

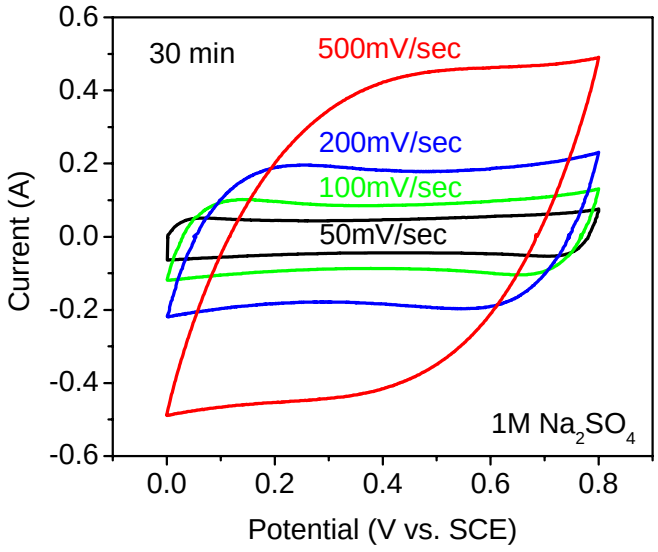

Figure 4.8. Typical cyclic voltammograms of the MnO_x/CFP composite electrodes prepared by deposition of MnO_x for 30 minutes in 1M Na_2SO_4 solution measured at different scanning rates (50~500 mV/sec) using a 3-electrode configuration.

Long cycling test was also performed to evaluate the stability of amorphous MnO_2 and the mixed-valent MnO_x electrode. The mixed-valent MnO_x electrode displayed remarkable long-term cycling stability; cyclic voltammograms collected after 100,000 and 200,000 cycles (Figure 4.9) showed little change, demonstrating the practical importance of these electrodes. However, the capacitance of the amorphous MnO_2 degraded considerably during cycling (Figure 4.10). It should also be noted that interconnectivity of CFP is particularly important to achieve good mechanical robustness and durability, since any failure of some individual fibers would have minimal impact on the overall performance of the electrode.

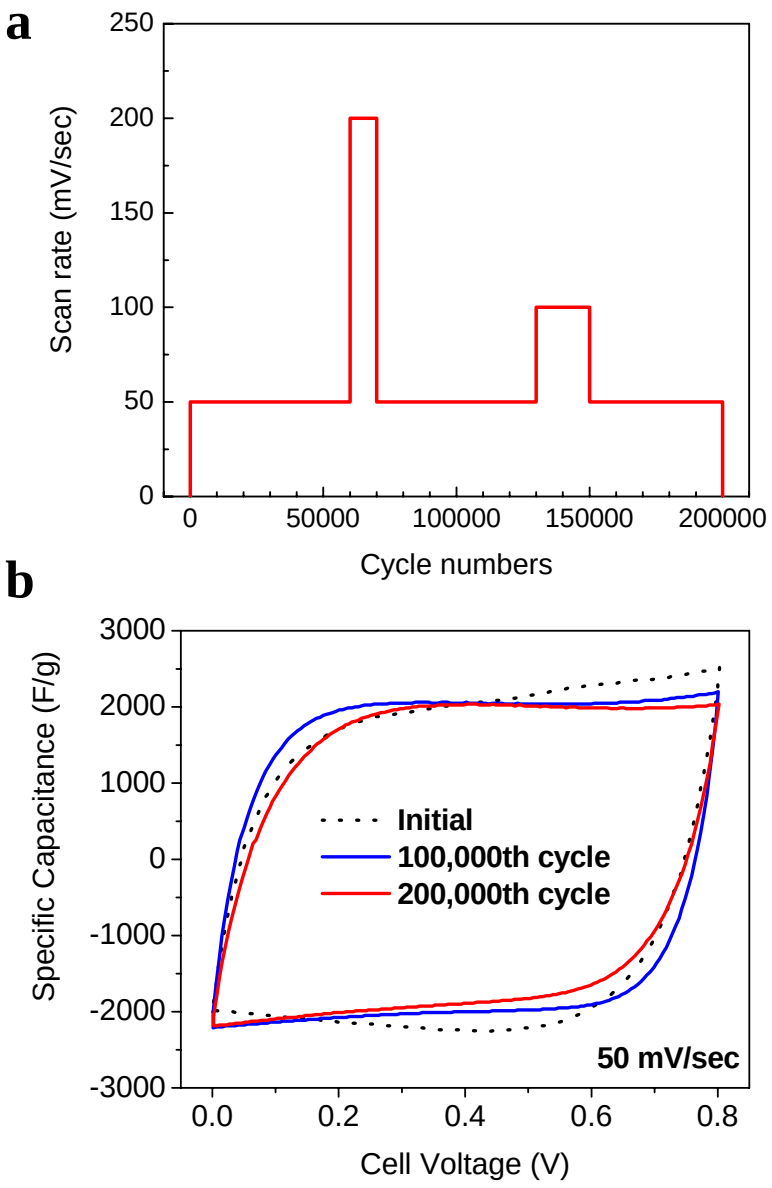

Figure 4.9. a, Voltage scan rates used in the long-term cycling tests operated continuously for 200,000 cycles performed for a mixed-valent MnO_x electrode. **b,** Cyclic voltammograms before and after long-term cycling at a scan rate of 50mV/sec showing excellent cycling stability.

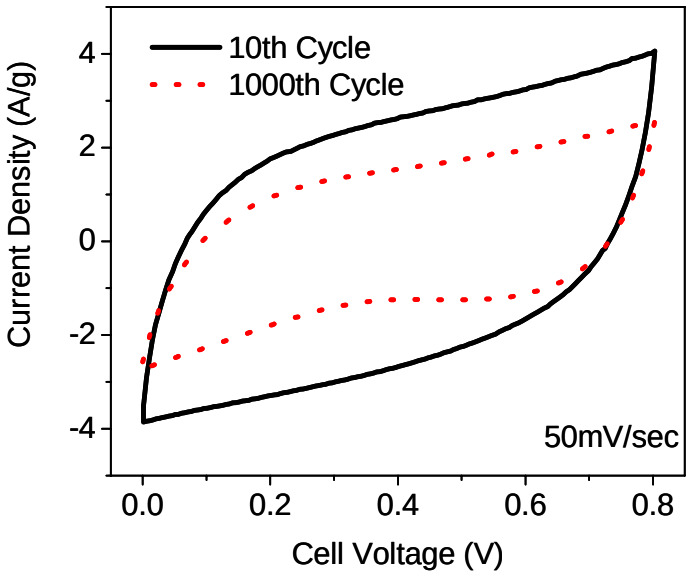

Figure 4.10. Cyclic voltammograms of amorphous MnO_2 electrode: initial and after 1,000th cycle at a scan rate of 50 mV/sec showing notable degradation in performance during cycling.

It is noted that the local atomistic structure and electronic structure of the main bulk phase in the mixed-valent MnO_x is similar, but not identical, to those for Mn_3O_4, as revealed by XAS analysis, which will be discussed in more details later. The electrochemical behavior of Mn_3O_4 in the mixed-valent MnO_x is quite different as well. While it is reported in the literature that Mn_3O_4 often involves irreversible phase change to MnO_2 during cycling[72,73], synchrotron XRD analysis of the mixed-valent MnO_x electrodes suggested that the mixed-phases (Mn_3O_4, Mn_2O_3 and MnO_2) were retained after 2,000 cycles, implying that the phases changes are highly reversible (Figure 4.11).

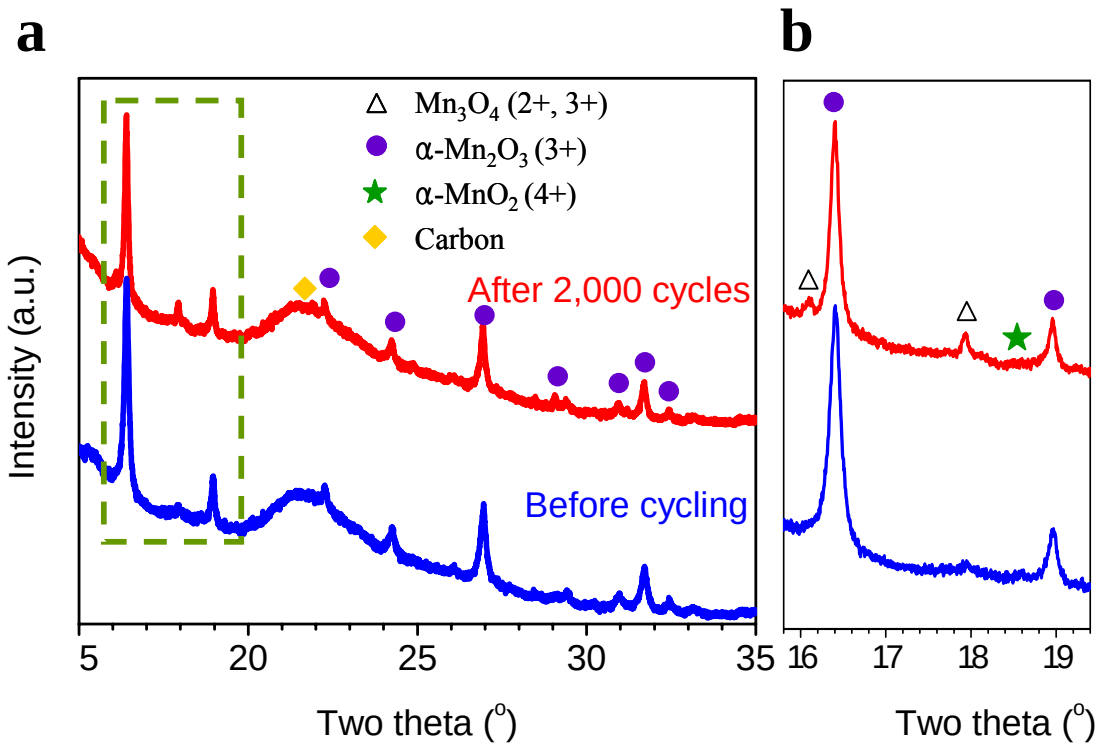

Figure 4.11. a, Synchrotron X-ray diffraction (XRD) pattern (Transmission mode) of MnO_x electrodes before and after 2,000 cycles, **b,** Enlarged view of XRD pattern of MnO_x highlighted in (a). The mixed-phases (Mn_3O_4, Mn_2O_3 and MnO_2) were retained after 2,000 cycles and the peak intensity of Mn_3O_4 slightly increased.

4.3. Effect of Different Cations in Electrolytes on the Pseudocapacitance

The effect of different cations (Na^+, H^+ and Ca^{2+}) in the electrolyte was also investigated. In particular, the mixed-valent MnO_x electrode showed the best performance in 1M H_2SO_4 solution (Figure 4.12). Based on the charge-discharge curves at a constant current of 3.07 A/g, the calculated specific capacitance of the mixed-valent MnO_x electrodes with H^+ was about 3,859 F/g, the highest capacitance ever reported

among all known pseudocapacitor materials, including MnO_2 (1,145 F/g)[48], $Ni(OH)_2$ (1,335 F/g)[74], and RuO_2 (1,340 F/g)[75].

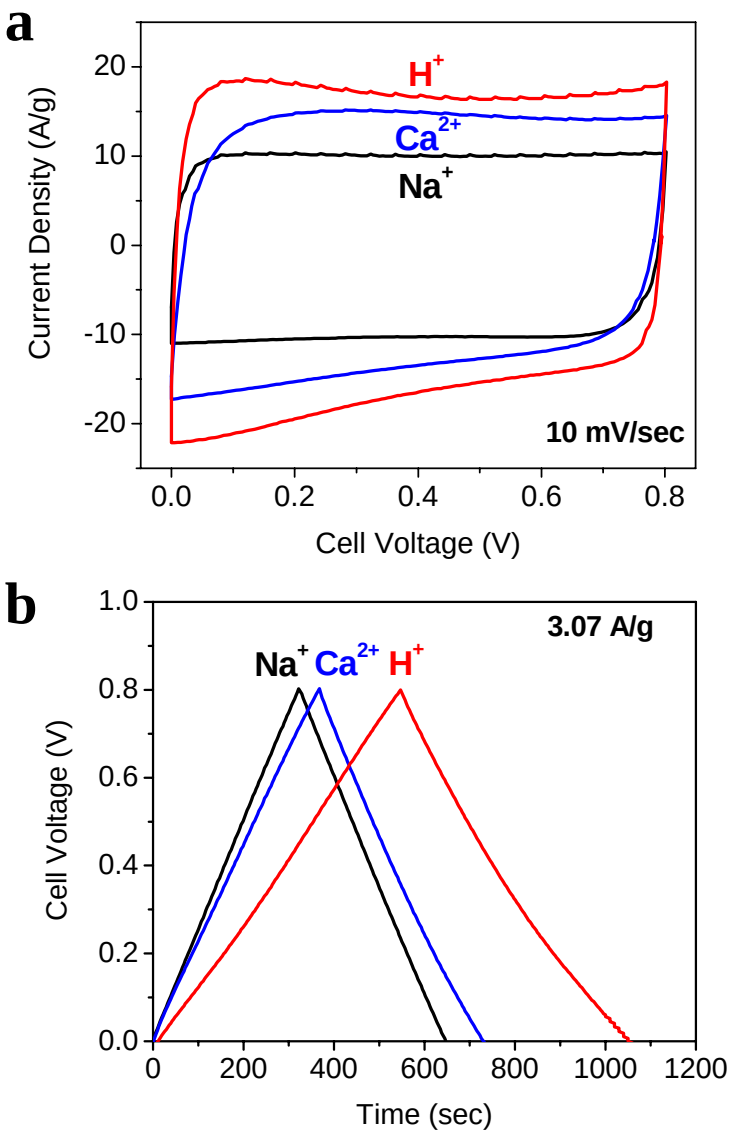

Figure 4.12. a, Comparison of cyclic voltammograms of symmetric pseudocapacitors constructed from mixed-valent MnO_x electrodes in different electrolytes containing H^+, Na^+ and Ca^{2+} measured between 0 and 0.8V at a scan rate of 10 mV/sec. **b,** Typical charge-discharge curves of mixed-valent MnO_x electrodes tested in different electrolytes containing H^+, Na^+ and Ca^{2+} at a constant current of 3.07 A/g.

Interestingly, the mixed-valent MnO_x electrode also showed very high performance in the electrolyte containing divalent ion Ca^{2+} (3,016 F/g) as shown in Figure 4.13. In addition, the mixed-valent nature of Mn_5O_8 (4+, 2+)[76] formed on the surface may allow efficient insertion of cations, as suggested in a previous study of Mn_5O_8 for multi-electron intercalation (M^{2+}) electrodes for batteries[77]. Further, the mixed-valent MnO_x also showed excellent rate capability with H^+ and Ca^{2+}, as evidenced by the square shape of the cyclic voltammograms and symmetrical charge-discharge curves, suggesting that both mass and charge transfer processes are fast and highly reversible (Figure 4.13-4.15).

In general, these effects can be attributed to many factors, including the size of the cation, the size of the hydration sphere of the cation in the aqueous electrolyte, the mobility of the cation, and the rate of adsorption/desorption at the surface sites. The dehydration/hydration rate of the ion may influence the rate of adsorption/desorption at the surface reaction sites. In fact, some of the factors may be inter-related. For instance, an increase in energy associated with lattice distortion would favor insertion of smaller cations. In contrast, an increase in energy associated with the removal of water molecules from a solvated cation may favor larger cations of smaller charge density with fewer solvated water molecules. Also, one may think it would be more difficult for large hydrated sphere of cation to be inserted into an oxide than smaller ones, but one has to consider the rate of desolvation (i.e. dehydration) together.

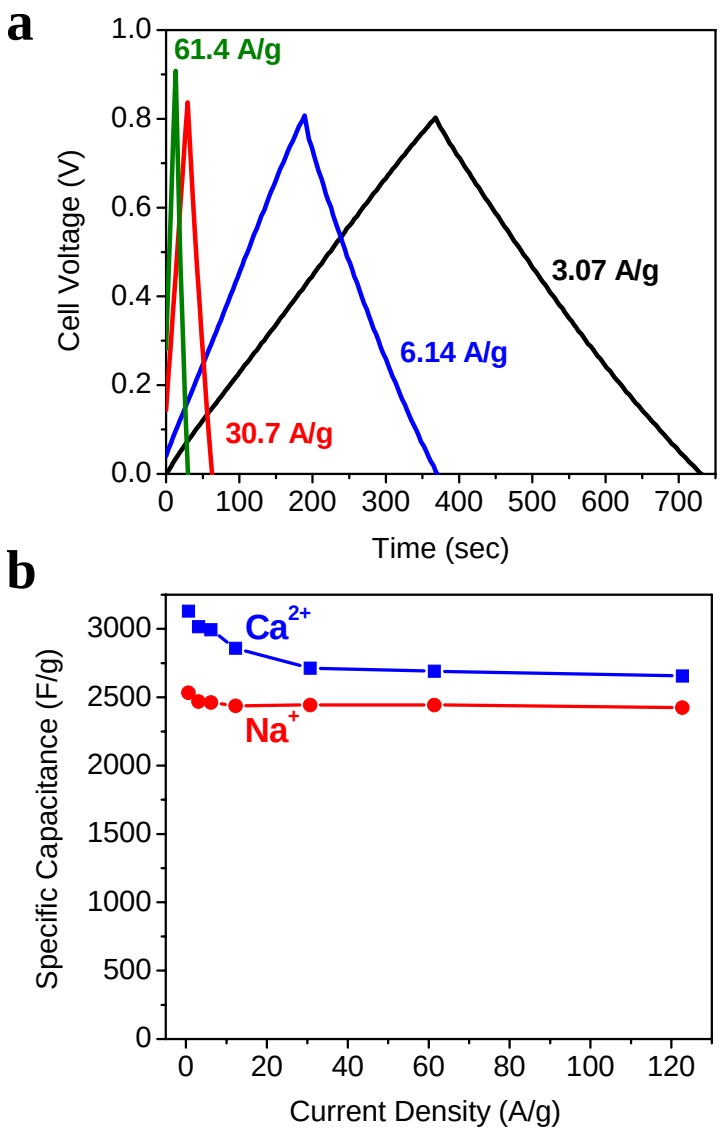

Figure 4.13. a, Typical charge-discharge curves of symmetric pseudocapacitors constructed from mixed-valent MnO_x electrodes in 1M $Ca(NO_3)_2$ solution at different current densities showing ideal capacitor behavior. **b,** Specific capacitance at different current densities demonstrating superior rate-capability with Ca^{2+}. Only the weight of the active electrode material (MnO_x, ~0.16 mg/cm^2) was considered in the specific capacitance calculations.

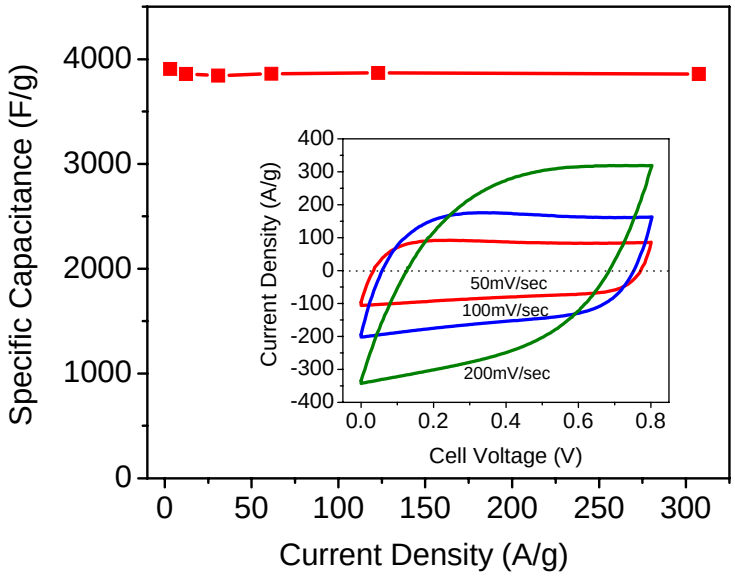

Figure 4.14. Specific capacitance at different current densities, demonstrating superior rate capability with H^+. Insert shows cyclic voltammograms acquired at different scan rates. Only the weight of the active electrode material (MnO_x, ~0.16 mg/cm^2) was considered in the specific capacitance calculations.

In addition, the charge storage mechanism may also play an important role. Since α-MnO_2 has a tunnel structure, not only monovalent but also divalent cations can be inserted, depending on the size of the tunnels and that of the cations. A good match between the size of the cations and that of the pores/tunnels is important to fast insertion, although it is rarely discussed in pseudocapacitors.

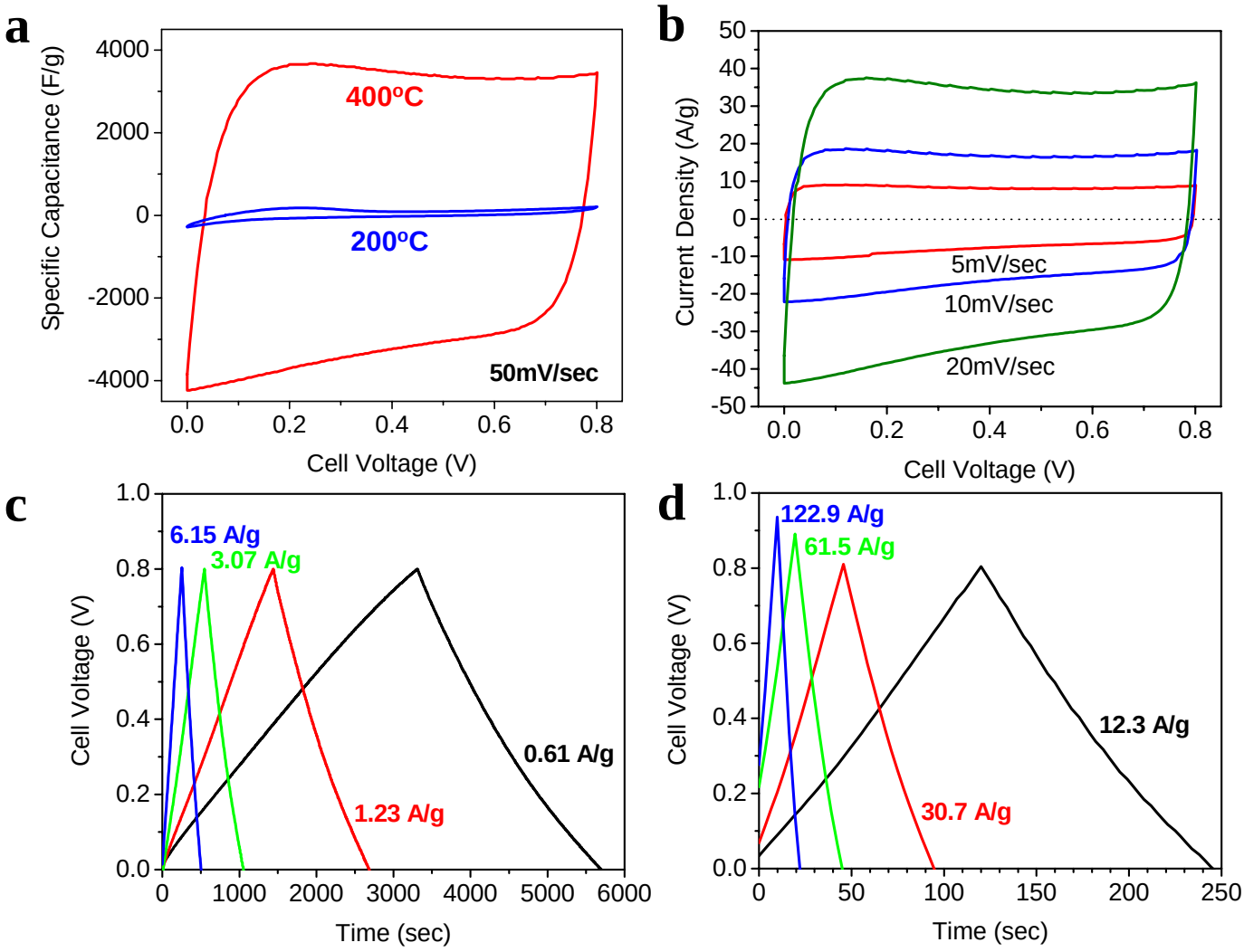

Figure 4.15. a, Cyclic voltammograms of symmetric pseudocapacitors constructed from amorphous MnO_2 and mixed-valent MnO_x electrodes in 1M H_2SO_4 solution at a scan rate of 50 mV/sec. **b,** Cyclic voltammograms for mixed-valent MnO_x electrodes with H^+ in 1M H_2SO_4 solution at different scan rates (5~20 mV/sec). **c,** Typical charge-discharge curves of mixed-valent MnO_x electrodes in 1M H_2SO_4 solution measured at low current densities (0.61~6.15 A/g) and **d,** measured at high current densities (12.3~122.9 A/g). Only the weight of the active electrode material (MnO_x, ~0.16 mg/cm^2) was considered in the specific capacitance calculations.

To rule out the effect of counter-anions, cyclic voltammograms of the MnO_x/CFP composite electrodes were collected in electrolytes with different cations (H^+, Na^+, and Ca^{2+}) using a 3-electrode configuration. The potential was measured versus a Saturated Calomel Electrode (SCE) and the measured currents (A), not the normalized current with respect to the loading amount of MnO_x (A/g), are presented in Figure 4.16. The results from 3-electrode configuration agree very well with our experimental results in symmetric configurations; the mixed-valent MnO_x electrode showed the best performance in 1M H_2SO_4 solution. The mixed-valent MnO_x electrode also showed higher performance with Ca^{2+} than with Na^+. Further, the mixed-valent MnO_x showed excellent rate capability in all electrolytes (especially with H^+) up to 500 mV/sec, suggesting that both mass and charge transfer processes are fast and highly reversible.

From the fundamental point of view, the divalent cations such as Ca^{2+} may have the advantage of offering higher energy density. There are experimental evidences that divalent cations such as Ca^{2+} can be inserted into oxides. Using X-ray Photoelectron Spectroscopy (XPS), Xu et al. showed that the Ca^{2+} ions are involved in the charge storage process of MnO_2 in an aqueous system[78], demonstrating that the specific capacitance of MnO_2 is higher in the electrolyte containing Ca^{2+} than that with Na^+. Also, divalent cations can be stored in the tunnels of α-MnO_2. In nature, various tunnel structures of MnO_2 (such as α-MnO_2) are abundantly found with foreign cations (including monovalent and divalent cations) filled in their tunnels[49], indicating that it would be possible to utilize these tunnels for insertion of divalent cations. In this study, the presence of mixed-valence (2+, 3+ and 4+) in the porous, nano-architectured MnO_x layer with a graded oxidation state may allow cycling between various oxidation sates of

manganese, thus facilitating facile redox reactions responsible for larger specific capacitance. Further, mixed-valent phase Mn_5O_8 (4+, 2+) formed on the surface may allow accommodation of divalent cations, as suggested in a previous study of Mn_5O_8 for multi-electron intercalation (M^{2+}) electrodes for batteries[77].

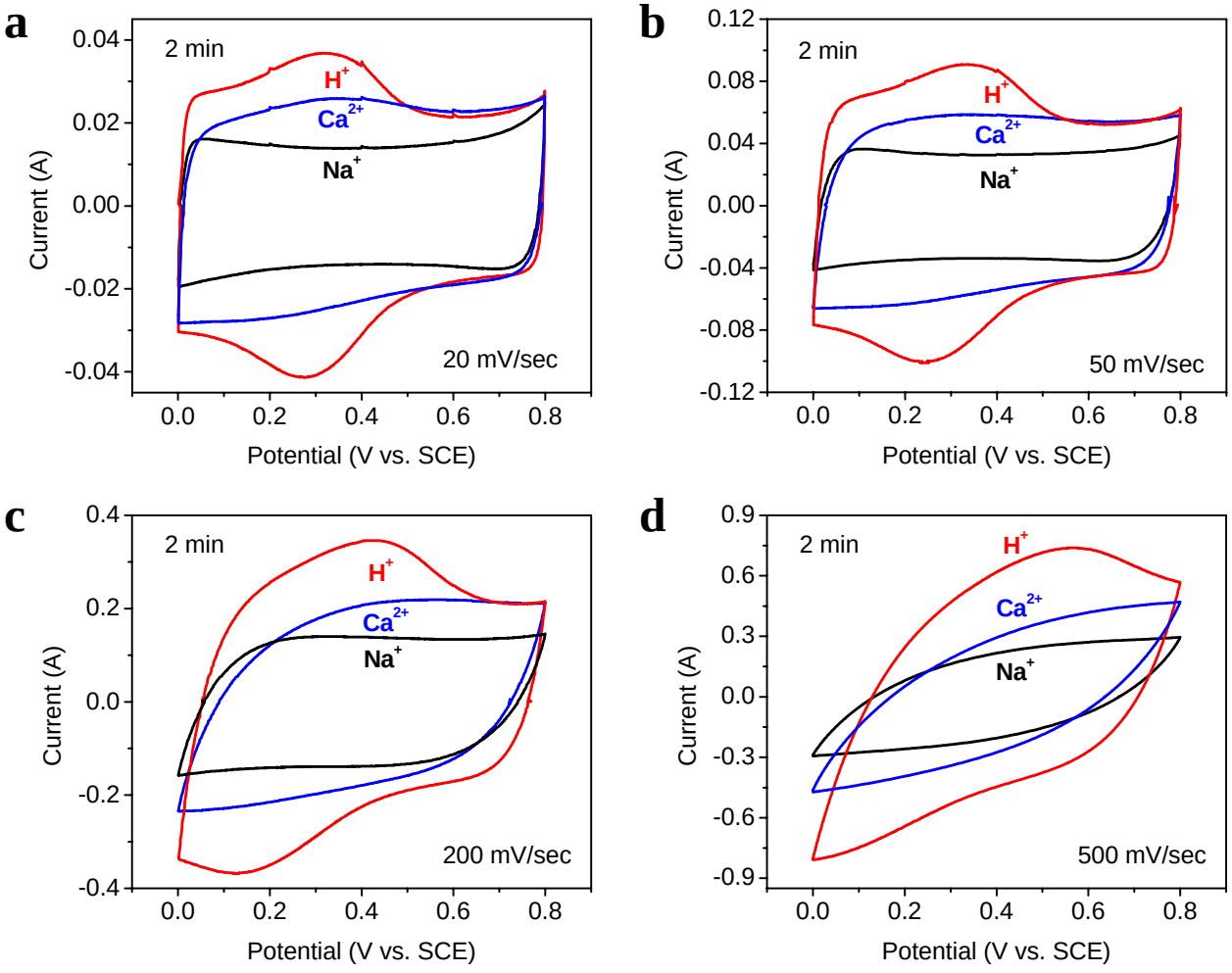

Figure 4.16. Comparison of cyclic voltammograms of the MnO_x/CFP composite electrodes acquired in aqueous electrolyte containing H^+, Na^+ and Ca^{2+} using a 3-electrode configuration at different scanning rates of **a,** 20 mV/sec**, b,** 50 mV/sec **c,** 200 mV/sec, and **d,** 500 mV/sec.

While the cyclic voltammograms with Ca^{2+} showed similar rectangular shape as those with Na^{+} at higher current densities, it is noted that the shape of the cyclic voltammograms with H^{+} is quite different. As shown in Figure 4.16, there are additional reversible reduction/oxidation peaks, which might indicate the reversible incorporation of protons into the mixed-valent, nanoporous MnO_x. There are many experimental evidences that protons can be inserted into MnO_x. For example, when MnO_2 is used as the active cathode material in a primary Zn/MnO_2 alkaline battery (1.5V), insertion of protons from the aqueous electrolyte is accompanied by the reduction of Mn[79]. As another example, when Toupin et al. reported high capacitance (1,380 F/g) for MnO_2, they found that the valence of Mn varied between +4 and +3 using *ex situ* XPS[44]. However, the amount of charge corresponding to Na ions was far less than the total amount of charge observed, suggesting that protons (in addition to Na^{+}) are important part of the counter ions for balancing the charge[44]. Kuo et al.[80] also reported that bulk insertion/extraction of H_3O^{+} occurs into/from the crystalline MnO_2. The higher mobility of proton in an aqueous electrolyte than those of other cations could be an important factor contributing to larger capacitance as well since the charge/discharge process of pseudocapcitors are often limited by the kinetics. Also, the ionic conductivity of the incorporated cations in the solid electrode is important.

To gain some insights into the roles of different cations, electrochemical impedance spectroscopy (EIS) was performed in a 3-electrode configuration. As shown in Figure 4.17, EIS data clearly show much smaller charge transfer resistance (smaller diameter of the semicircle in the impedance spectrum) with H^{+}, an indication of facile proton incorporation into the mixed-valent MnO_x, although the size of solvated protons

may be bigger than those of other hydrated Na^+ and Ca^{2+} as shown in Table 4.1. Also, the long tail at low frequencies of the mixed-valent MnO_x with H^+ is closest to a vertical line for a perfect capacitor, another implication that the mixed-valent MnO_x has higher capacitance and lower diffusion resistance with H^+ than with other cations (Na^+ and Ca^{2+}).

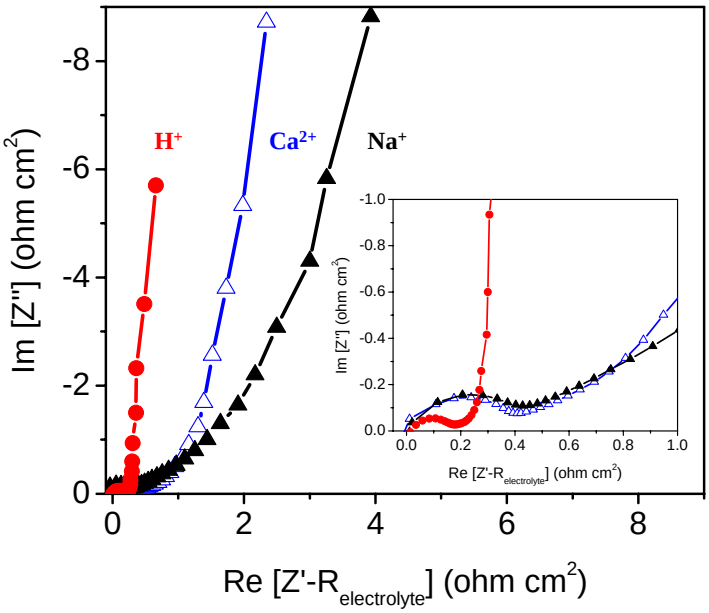

Figure 4.17. Electrochemical impedance spectra of the MnO_x/CFP composite electrodes acquired in aqueous electrolyte containing H^+, Na^+ and Ca^{2+} at open circuit voltage (OCV) perturbed by an ac voltage of 10 mV in a wide frequency range.

Table 4.1. Ion size and radius of hydrated sphere of cations relevant to this study[78,81,82].

Ion	Size / Å	
	in crystals	in aqueous solution
H^+	-	9
Na^+	1.02	4
K^+	1.38	3
Li^+	0.69	6
Ca^{2+}	0.99	5

To put the performance of the mixed-valent MnO_x electrode in context, its energy and power densities (calculated from the charge-discharge curves) were compared with those of other electrical energy storage systems in Figure 4.18. When normalized to the weight of active materials, the energy density of the mixed-valent MnO_x (single electrode) reached ~347 Wh/kg at a power density ~2,458 W/kg and showed little dependence on cycling rate, still retaining 343 Wh/kg at power densities up to ~245,845 W/kg (Figure 4.17). Only the weight of the active electrode material (MnO_x, $Ni(OH)_2$, or MnO_2) was considered in the specific energy and power density calculations. For the mixed-valent MnO_x electrode, the weight of active electrode material was ~0.16 mg/cm^2. It is expected that, if matched with proper counter electrodes (such as lithium metal and lithium-containing compounds) in asymmetric cells, the energy density and power density of this electrode can be further improved.

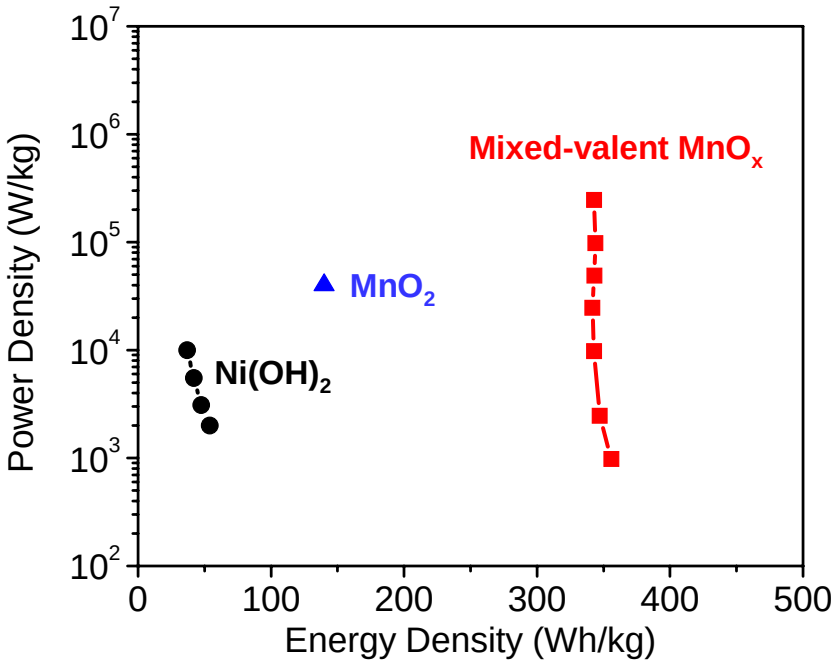

Figure 4.18. Ragone plot showing high energy and power densities for the mixed-valent MnO_x electrode (single electrode) with H^+ in comparison with the results from recent publications[48,74].

In addition to the demonstrated energy and power densities far superior to those ever reported for electrochemical capacitors, it was demonstrated that the reversible specific capacities (Figure 4.19) were even larger than those for conventional batteries, reached ~431mAh/g at 3.07 A/g and still retained 427 mAh/g at a very fast cycling rate of 307.3 A/g or 720C rate (i.e., full charge or discharge within ~5 seconds). The specific capacity (mAh/g), calculated from the discharge curves shown in Figure 4.15 c and d (the constant current density in mA/g multiplied by the discharging time in h in the cell

voltage range from 0.8V to 0V), reached ~431 mAh/g at 3.07 A/g and still maintained 427 mAh/g at a very fast cycling rate of 307.3 A/g, corresponding to full charge or discharge within ~5 seconds (equivalent to ~720C rates for batteries).

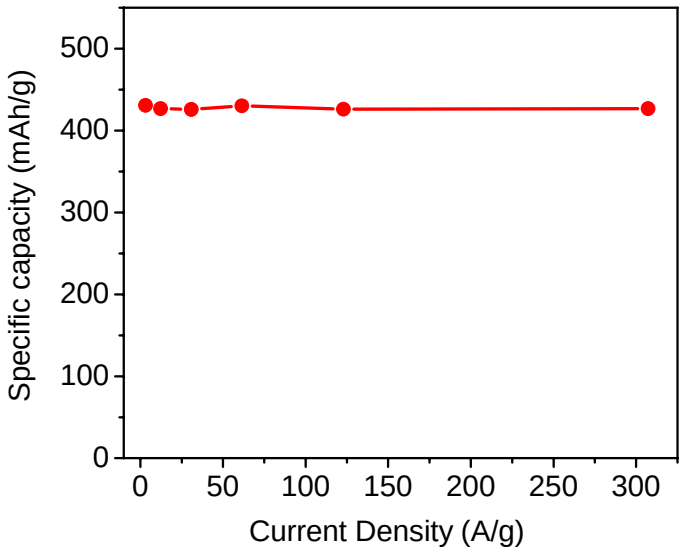

Figure 4.19. Specific capacity (mAh/g) of the mixed-valent MnO_x electrodes at different current density. Only the weight of the active electrode material (MnO_x, ~0.16 mg/cm^2) was considered in the specific capacity calculations.

4.4. Correlation of Structural Information with Electrochemical Properties

The phase composition and nanostructure of the electrode material is very sensitive to the annealing conditions. For example, when the annealing temperature was increased from 400 to 450^{o}C (but still in air for 2h), XRD analysis suggested that the Mn_3O_4 phase was converted to α-Mn_2O_3. Figure 4.20 shows the α-Mn_2O_3 peaks grew at 450^{o}C while Mn_3O_4 peaks disappeared. It agrees well with our observation with *in-situ*

Synchrotron XRD results. Interestingly, performance dropped significantly with increased charge transfer resistance as shown in Figure 4.20 (b) and (c).

Similarly, when the annealing atmosphere was changed from air to N_2 and 4% H_2 balanced with Ar (still at 400^{o}C for 2 h), Figure 4.21 (a) shows that as-synthesized amorphous MnO_2 converted to pure Mn_3O_4 when annealed in N_2 and even reduced further to form a mixture of MnO/Mn_3O_4 in 4% H_2, respectively. The mixed-valent MnO_x demonstrated excellent "square-shape" cyclic voltammograms at 50 mV/sec and superior rate-capability in 1M Na_2SO_4, indicating that surface reactions are highly reversible and very fast. However, with the same thickness of manganese oxide coating, when the annealing atmosphere was changed from air to N_2 and 4% H_2 balanced with Ar (still at 400^{o}C for 2h), the electrochemical performance of these electrodes dropped significantly compared to electrodes annealed in air at 400 ^{o}C for 2h as shown in Figure 4.21 and 4.22. Electrodes made of these phases performed poorly, far inferior to those of the electrodes made of the multi-valent MnO_x created by annealing in air at 400^{o}C for 2h.

Further, the amorphous MnO_2 powder sample (synthesized under the same conditions but without carbon support) remained amorphous when annealed at 400^{o}C, but transformed to crystalline α-Mn_2O_3 when annealed at 500^{o}C, in air for 2 h in the absence of carbon (Figure 4.23).

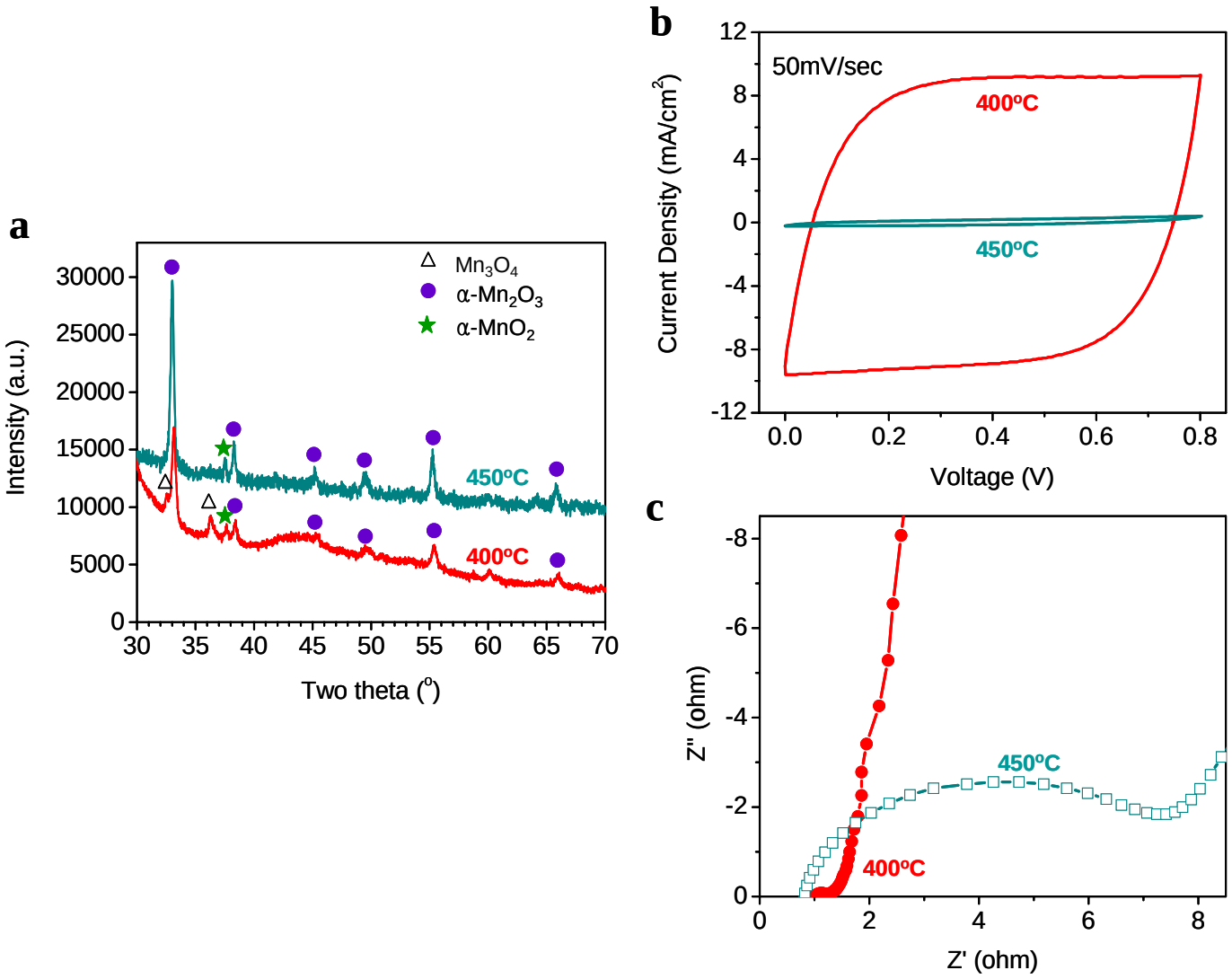

Figure 4.20. a, Laboratory XRD pattern of MnO_x electrodes annealed at 400 and 450°C in air for 2h. **b,** Cyclic voltammograms measured at a scan rate of 50mV/sec of electrochemical capacitors constructed from electrodes annealed at 400 and 450°C in air for 2h. **c,** Electrochemical impedance spectra collected at open circuit voltage (OCV) under the influence of an ac voltage of 10 mV.

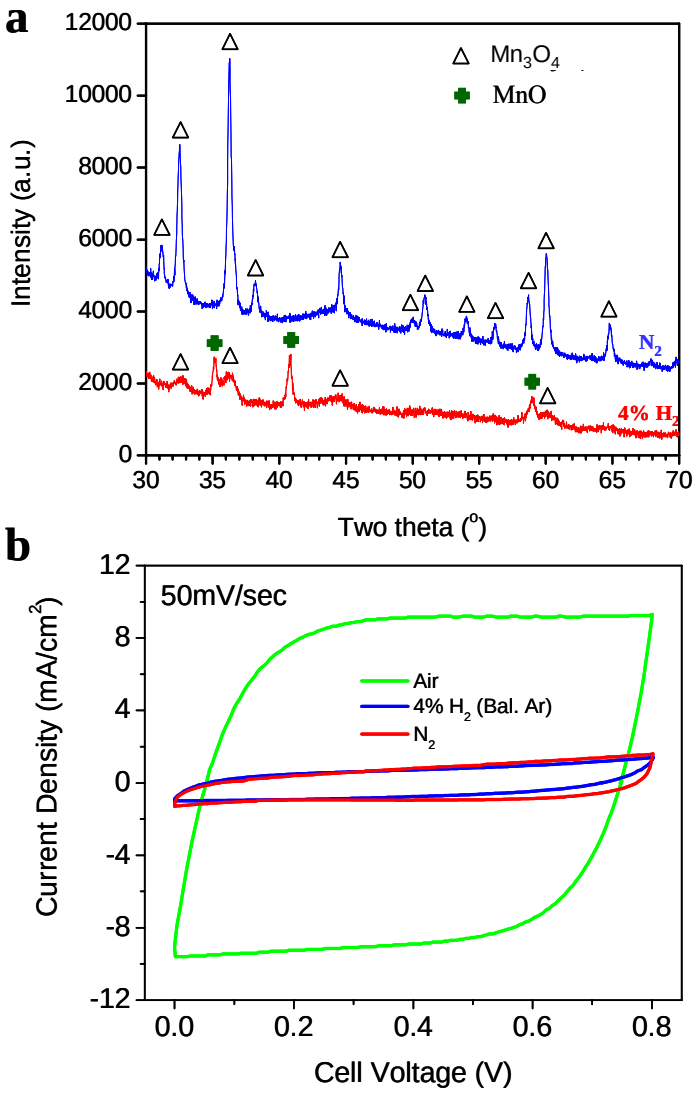

Figure 4.21. a, Laboratory XRD pattern of MnO_x electrodes annealed at 400°C in N_2 and 4% H_2 (balanced with Ar) for 2h. **b,** Cyclic voltammograms measured at a scan rate of 50mV/sec of electrochemical capacitors constructed from electrodes annealed at 400°C in N_2 and 4% H_2 (balanced with Ar) for 2h.

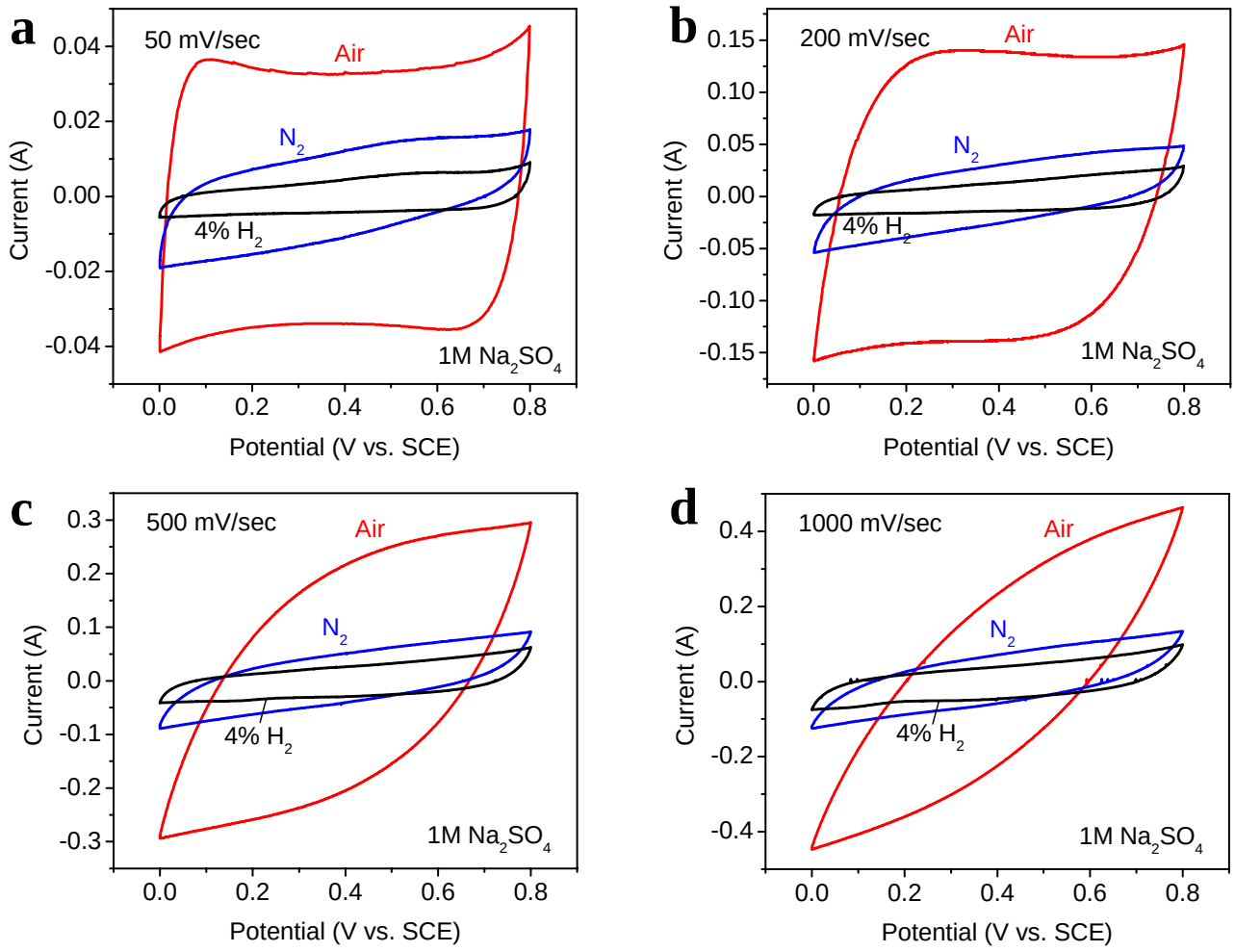

Figure 4.22. Typical cyclic voltammograms of the MnO_x/CFP composite electrodes annealed at 400°C under different atmosphere (Air, N_2, and 4% H_2) measured in 1M Na_2SO_4 solution using a 3-electrode configuration at different scanning rates: **a,** 50 mV/sec**, b,** 200 mV/sec, **c,** 500 mV/sec, and **d,** 1000 mV/sec.

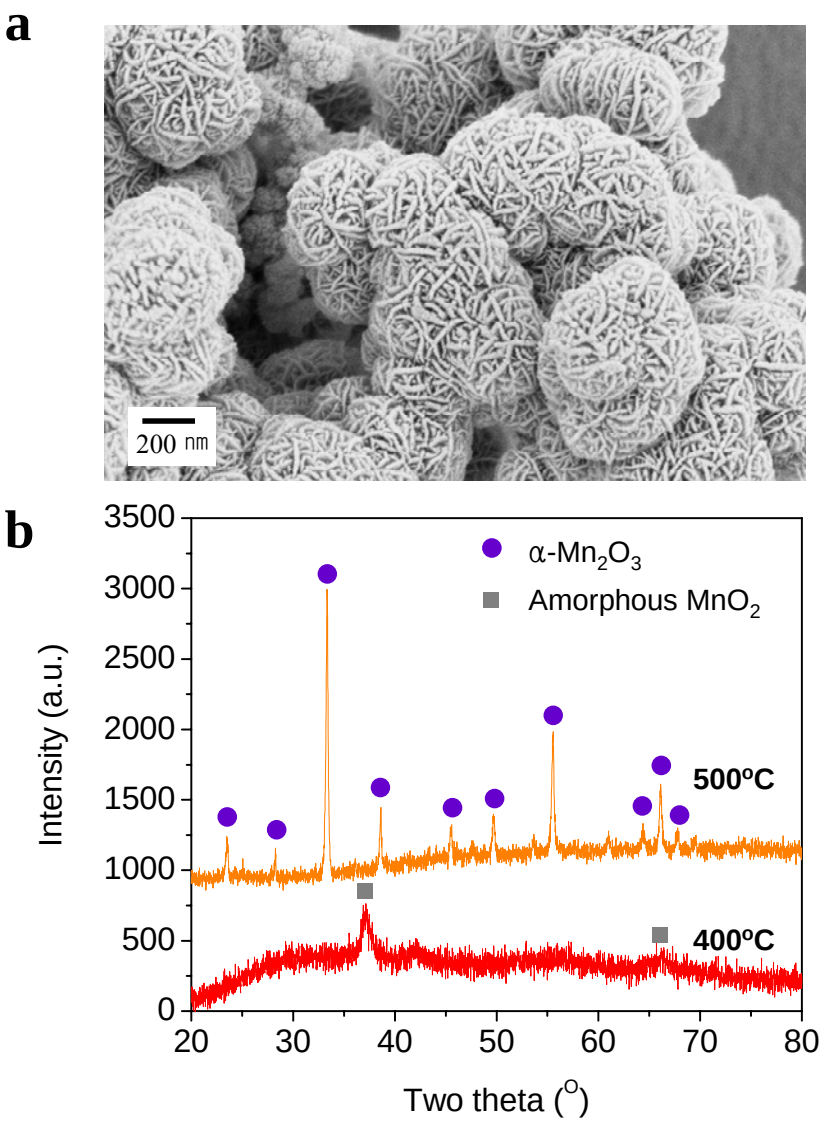

Figure 4.23. a, SEM image of powder samples synthesized under the same condition ($KMnO_4$ as precursor in 2M H_2SO_4 solution at 75°C) without carbon fiber paper. **b,** Laboratory XRD patterns of the powder samples annealed at 400°C and 500°C in air for 2h without carbon fiber paper.

It is believed that the annealing conditions played an important role in creating this unique nano-architecture. The phase composition of the electrode material is very sensitive to the annealing conditions and carbon. Based on the *in-situ* synchrotron XRD data collected during the annealing process, it was found that annealing at 400^{o}C for 2 h produced multi-phases with greatly enhanced pseudocapacitive behaviors. As previously discussed, it was revealed that small crystalline phases started to form above 360^{o}C. At 400^{o}C, sharp peaks of crystalline α-Mn_2O_3 appeared with small amounts of Mn_3O_4 and α-MnO_2.

It is noted that, as shown in the insert of Figure 4.23, while the peak intensity of Mn_2O_3 increased continuously, the peak intensity of Mn_3O_4 increased first for ~1 hour, and then started to decrease. When the annealing at 400^{o}C was a little bit longer than 2 h (e.g., more than three hours), the intensities of the Mn_3O_4 peaks decreased with annealing time at 400^{o}C and disappeared after annealing at 400^{o}C in air for 3 hours (the result is not shown) and the performance dropped significantly, implying that bulk phase Mn_3O_4 in the mixed-valent MnO_x might play important roles in the observed large pseudocapacitance contrary to previous works (largely with MnO_2) which demonstrated only the surface is active.

A slightly better performance was observed with higher intensity of Mn_3O_4 peak found in the *in-situ* synchrotron XRD pattern. It appears that different annealing condition would be required to form these unique multi-valent MnO_x, depending on the thickness of MnO_x film and/or choice of carbon. However, this will be largely an engineering effort to further find the optimized annealing condition. It is in part the reason why this enhanced capacitance of multi-valent MnO_x we report has not been

observed before, given the large amount of work on nanostructured MnO_2 for energy storage devices.

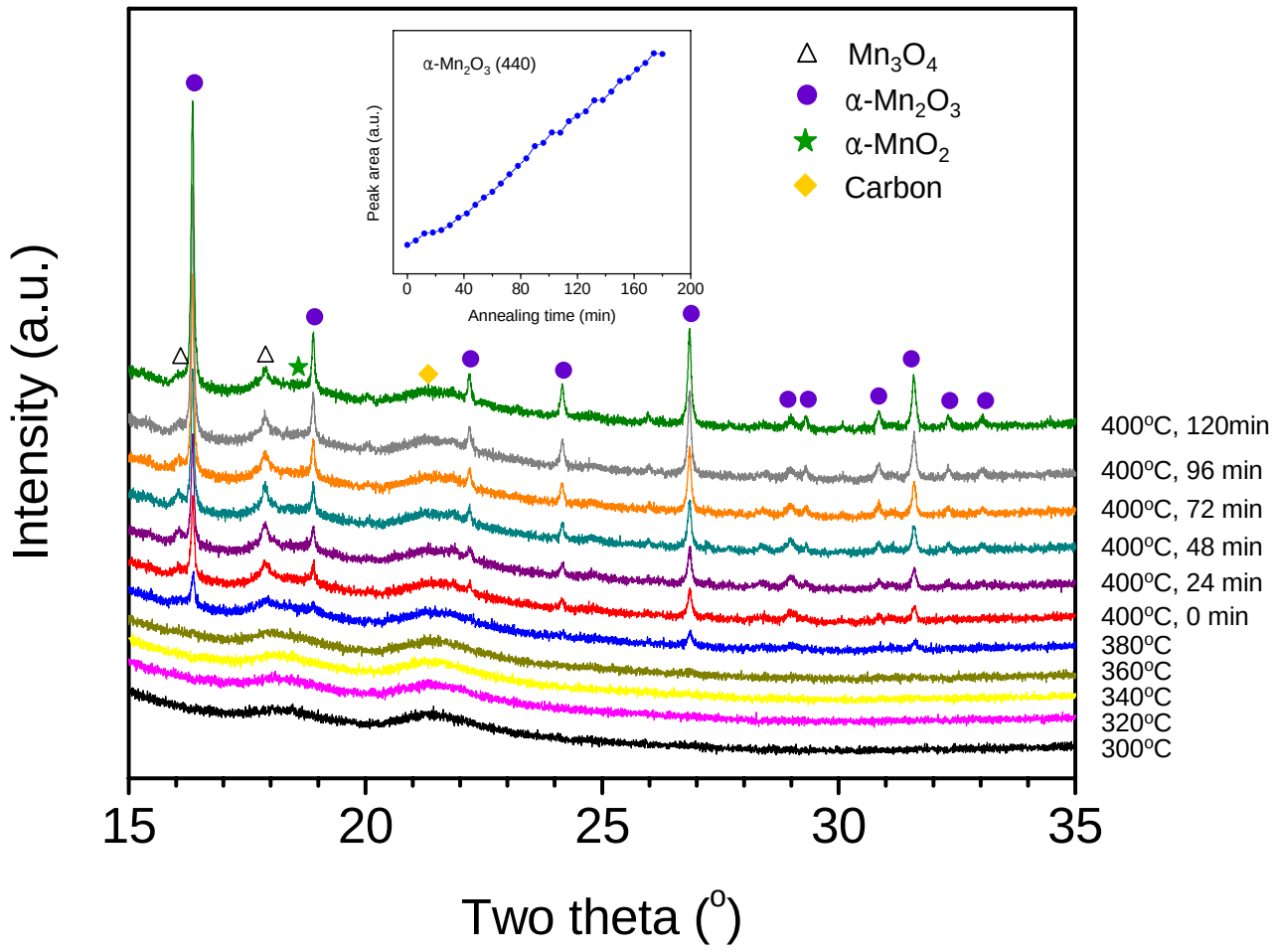

Figure 4.24. *In-situ* synchrotron-based XRD patterns (transmission mode) of MnO_x coating measured at different temperatures and annealing times.

4.5. Summary

In this chapter, it was demonstrated that a nanostructured, mixed-valent manganese oxide electrode can exhibit dramatically enhanced pseudocapacitive behavior with the highest demonstrated specific capacitance (3,859 F/g) among all known pseudocapacitor materials, while maintaining excellent rate capability and long cycling life (little degradation after 200,000 cycles). The demonstrated performance is far superior to those ever reported for electrochemical capacitors. The results presented in this section suggest that electrochemical capacitors can achieve high energy density, offering potential for reaching energy densities comparable to those of existing batteries.

The unique mixed-valent MnO_x developed in this thesis will have immediate and profound implications for a new generation of electric energy storage devices for many emerging applications such as electric vehicles and smart-grids. However, many fundamental questions must be answered before this potential can be realized. Above all, a rigorous understanding of the mechanisms and kinetics of charge storage processes in mixed-valent compounds is critical to achieving rational design of improved electrode materials and structures for efficient energy storage and conversion.

CHAPTER 5

INVESTIGATION INTO THE CHARGE STORAGE MECHANISM

In the previous chapter, it was demonstrated that nanostructured, mixed-valent MnO_x/CFP electrodes exhibited the highest specific capacitance (3,859 F/g) of all materials investigated with excellent rate capability and long cycling performance. In this section, new insights into their charge storage mechanisms for enhanced pseudocapacitance are discussed based on both *ex-situ* and *in-situ* XAS analysis combined with electrochemical measurements.

5.1. Synchrotron-enabled X-ray Absorption Spectroscopic Study

X-ray absorption spectroscopy (XAS) is a technique that is atom-specific and capable of probing the local atomic and electronic structure around an atom of interest. X-ray spectroscopic absorption studies of structure are normally divided into two methods. While XANES (X-ray absorption near-edge structure) can give the information about oxidation state, site symmetry, and covalent bond strength, EXAFS (Extended X-ray fine structure) can provide information regarding inter-atomic distance, coordination number, and Debye-Waller factor. By performing both *ex-situ* and *in-situ* XAS analysis, the local atomic and electronic structure of the mixed-valent MnO_x can be analyzed and their changes upon charging and discharging can be observed in order to gain better insights into enhanced pseudocapacitive behavior and to explore the origin of the superior properties of this mixed-valent MnO_x material. The works presented in this section were a collaborative effort with research scientists at Brookhaven National Laboratory.

5.1.1. Experimental Methods

The synchrotron-enabled X-ray absorption (XANES and EXAFS) data were collected at the beamline X3B of the National Synchrotron Light Source (NSLS) at Brookhaven National Laboratory. The measurements were collected in transmission mode using a 13-element Ge detector. A Mn metal powder sample was used for energy calibration and data reduction as a means to follow standard procedures[83,84].

In-situ Mn K-edge XAS during charge-discharge (with constant current of 25uA) of the cell was carried out at the beamlines X18A and X19A in fluorescence mode using a PIPS detector. The reference Mn foil spectra were also measured simultaneously in transmission mode to provide an energy calibration.

5.1.2. *Ex-situ* XAS Study on the Mixed-Valent MnO_x

Ex-situ XAS results of as-synthesized electrode (amorphous MnO_2) and electrode (deposited for 2min) annealed at 400^oC in air (mixed-valent MnO_x) are shown in Figure 5.1. Overall XANES spectrum of the as-synthesized electrode is close to that of MnO_2. There is a weak pre-edge feature (peak A) and a strong main edge feature (peak C) for as-synthesized electrode. The pre-edge and main absorption edge are assigned to a 1s → 3d transition and a 1s → 4p transition, respectively. The double let of pre-edge peak for as-synthesized MnO_2 is the indication of the $Mn^{3+}O_6/Mn^{4+}O_6$ mixture. It is reasonable because K^+ from the precursor ($KMnO_4$) exists in the electrode.

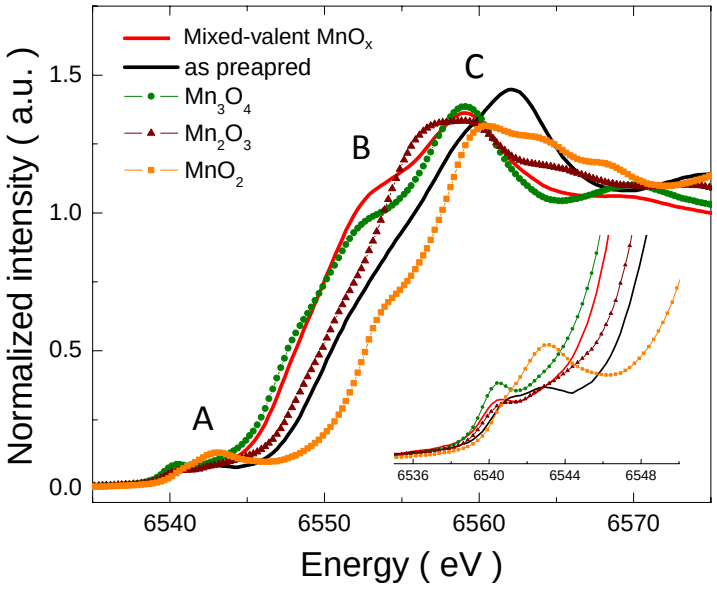

Figure 5.1. Mn K-edge XANES spectra of the as-prepared and the mixed-valent MnO_x (heat-treated at 400°C in air for 2h) electrodes in comparison with the reference spectra for Mn_3O_4, Mn_2O_3 and MnO_2. Inset shows the enlargement of the pre-edge region A. Data courtesy of Dr. Nam and Dr. Yang at Brookhaven National Laboratory.

XANES spectrum of mixed-valent MnO_x is shifted to the lower energy region indicating the average oxidation state of mixed-valent MnO_x is lower than as-synthesized sample. It can be explained by the fact that the higher absorption energy is required to excite the 1s core electron which is strongly bounded to the less screened nucleus. Overall XANES feature of mixed-valent MnO_x is close to that of Mn_3O_4 bulk. It agrees very well with our synchrotron XRD results which showed that the bulk phase of mixed-valent MnO_x was Mn_3O_4. In addition to the pre-edge feature (A) and main edge (C), however, there was a strong shoulder peak (B) developed on the edge. XANES main

peak energies are affected when the core-electron binding energy is changed by altering the bond distance or electronic charge density on the absorbing ion. The shoulder peak B represents the increased degree of covalency between the Mn(3d)-O(2p) bond due to the ligand to metal charge transfer (LMCT)[85,86]. The observed 1s → 4p + LMCT transition suggests that the electronic configuration of Mn ion in the ground state is changed by the redistribution of electronic charge density in the Mn-O bond.

The Fourier transform of *ex-situ* EXAFS data are shown in Figure 5.2 with the first peak corresponding to the Mn-O bond in the first coordination shell. The next two FT peaks represent two types of Mn-Mn bonds, corresponding to edge-shared MnO_6 octahedra and corner-shared MnO_6 octahedral, respectively. In accordance with XANES spectrum, as-synthesized electrode shows the local structure similar to that of a layered birnessite type MnO_2 structure in which Mn^{4+} cations predominantly assembled in layers of edge-sharing MnO_6 octahedral. Along with XANES spectrum, the Fourier transform of EXAFS data indicates that local structure of mixed-valent MnO_x is close to that of Mn_3O_4.

However, there are some unique differences in both XANES and EXAFS data. It is demonstrated that Mn_3O_4 and the mixed-valent MnO_x have the similar XANES shape with a reduced and broadened peak of the latter indicating more disordered structure by local distortions or multiphases. Also, much stronger shoulder peak indicates that there was a quite significant electronic structural change. Also, EXAFS data indicates that significant structural differences exist between mixed-valent MnO_x and Mn_3O_4. Mn-O peak position is shorter than that of bulk Mn_3O_4 suggesting shorter Mn-O bond length which is probably due to the increased covalent character between Mn-O bond and/or the

existence of Mn^{3+}/Mn^{4+} at the surface. In addition, overall amplitude of FT-EXAFS peaks is much smaller than that of bulk Mn_3O_4 suggesting the existence of local disorder. These unique XANES and EXAFS data implies that the formation of mixed-valent MnOx involves the changes in electronic as well as atomic structure.

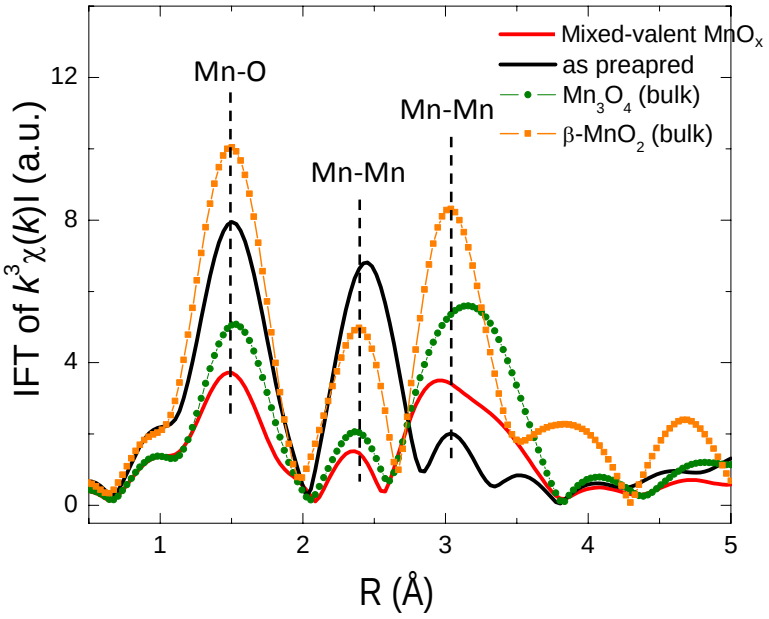

Figure 5.2. Fourier transform (FT) magnitude of the k^3 weighted EXAFS spectra of the as-prepared and the mixed-valent MnO_x (heat-treated at 400°C in air for 2h) electrodes in comparison with the reference Mn_3O_4 and MnO_2 spectra. The FT was not phase corrected so that the actual bond length may be ca 0.2 ~ 0.4 Å longer. Data courtesy of Dr. Nam and Dr. Yang at Brookhaven National Laboratory.

5.1.3. *In-situ* XAS Study on the Mixed-Valent MnO_x during Cycling

In-situ Mn K-edge fluorescence X-ray absorption spectroscopy (XAS) was used to observe the local atomic and electronic structural change of as-synthesized sample (amorphous MnO_2) as a function of the applied potential in 1M Na_2SO_4. In the charging process up to 1.0V, we observed the continuous edge shift toward the higher energy region indicating that the average oxidation state of the manganese ions in the electrode increases during oxidation of Mn^{3+} ions. When discharged down to 0.0V, the absorption edge returned to its initial lower energy state by reduction of Mn^{4+} ions. This spectral change agrees very well with the common belief that the charge compensation for the incorporation/extraction of cations into the MnO_2 occurs in the Mn site by the redox of Mn^{3+} to Mn^{4+} ion with accompanying electrons to maintain charge neutrality.

However, quite different spectral behavior was observed for the mixed-valent manganese oxide during cycling. *In-situ* Mn K-edge fluorescence XAS was used to observe the local atomic and electronic structural change of the mixed-valent manganese oxides in 1M Na_2SO_4. First, it was revealed that the average oxidation state and local structure of the mixed-valent manganese oxide changed reversibly during charging/discharging.

Again, overall XANES feature of mixed-valent MnO_x is close to that of Mn_3O_4 bulk. Mn_3O_4 itself is a mixed-valent compound and has a normal spinel structure: Mn^{2+} in tetragonal sites and Mn^{3+} in octahedral sites. Also, based on synchrotron XRD results, we know there are Mn^{2+} and Mn^{3+} predominantly in the bulk and Mn^{3+} and Mn^{4+} on the surface of the electrode. However, the quantitative information about the oxidation state changes of each three different oxidative Mn ion could not be determined from the XANES feature. XAS is a bulk technique and the information depth is a few micron

meter. Considering the fact that the thickness of MnO_x is less than 100nm and active surface layer would be even thinner, it is very possible that we cannot probe the oxidation state change of surface Mn ions. Instead, we have observed the average oxidation state change with the insertion/extraction of Na^+ ions.

When charged up to 1.0V, the main edge shifted slightly towards higher energy position indicating the increase of average oxidation state of Mn ions. Also, the intensity of main edge increased, indicating the increased local ordering. Since Mn^{3+} ion is a Jahn-Teller distorted site, the oxidation of Mn^{3+} to non Jahn-Teller Mn^{4+} ion leads to relative symmetric oxygen distribution. This might be one of the causes for the observed increase in the intensity of the main edge during the charge. FT EXAFS data also showed the increase of Mn-O and Mn-Mn peak amplitude during the charging. Since the charging leads to a relative uniform oxidation state of Mn^{4+} from the mixed oxidation state of Mn^{2+} and Mn^{3+}, the increase of FT peaks could be explained by the site ordered distribution, in addition to the decrease of the Jahn-Teller distorted Mn^{3+} sites in the octahedral symmetry.

Unlike the continuous edge-shift observed in amorphous MnO_2, we found the systematic decrease of shoulder B peak intensity for the mixed-valent MnO_x during the charging. The spectral change is attributed the decreased degree of covalency between Mn-O bond. From the *ex-situ* XANES before applying any potential, appearance of a strong B peak indicates that the ground state of the Mn atom can be described as an equilibrium of $Mn^{n+} + O^{2-} <-> Mn^{(n-1)+} + O^{1-}$ by LMCT process, i.e., electron transfer from ligand to Mn ions. The systematic decrease of peak intensity for the LMCT process is closely associated with the dominant formation of Mn^{n+}-O^{2-} ion pair from the

coexistence of $Mn^{(n-1)+}$-O^{1-} and Mn^{n+}-O^{2-} in the mixed-valent MnO_x by the transfer of hole state in the oxygen 2p band to the Mn atomic site, following by the decrease of Mn-O bond covalency. This observation also provides spectroscopic evidence that oxygen anion can also participate in the charge balance by redistributing the electrons around Mn-O bond.

The *in-situ* XAS results of mixed-valent MnO_x during the discharge from 1.0V to 0.0V. The average oxidation state and local structure of the manganese oxide changed reversibly during charging/discharging, indicating a highly reversible charge storage process. Shown in Figure 5.3, continuous edge shift towards lower energy was observed, indicating the decrease of average oxidation state of Mn ions. Also, the re-evolution of shoulder peak B at lower energy position was observed during discharging. It suggests the increased Mn-O bond covalency during the discharge process.

In particular, the return of shoulder peak to the initial position after charge-discharge cycle indicates that the change of Mn-O covalency is participating in the charge compensation process in the highly reversible manner. Also, it is demonstrated that the charge excess/deficiency was compensated with electronic structural variations of oxygen ion as well as Mn ion. The fact that covalency plays a role by reversible LMCT process has never been reported for this type of material for pseudocapacitors.

During the discharge process, the intensity of main peak C decreased gradually, implying the increase of local disorder. Similarly, the EXAFS results showed that the FT peaks corresponding to Mn-O and Mn-Mn (edge) bond decreased during discharge, indicating an increase of the degree of disorder in the MnO_6 octahedra framework. This can be attributed to the formation of Jahn-Teller distortion active Mn^{3+} ions as well as the

static disorder of mixed Mn^{2+}, Mn^{3+} and Mn^{4+} ions upon the reduction of Mn^{4+} during the discharge process.

In summary, the local atomic and electronic structure change of the mixed-valent MnO_x during the charge-discharge was investigated by *in-situ* X-ray absorption spectroscopy. Mn K-edge spectra obtained as a function of potential clearly revealed a reversible redox behavior of Mn ions during charging-discharging process. The observed oxidation state change of Mn ion, however, cannot account for the large pseudocapacitance observed experimentally. Therefore, another charge compensation mechanism is required. The most likely additional charge compensation mechanism is the participation of oxygen, probably partial oxidation of coordinated O^{2-} in the crystals, in the reversible charge–discharge reaction. Indeed, in addition to the main edge shift, we observed the reversible evolution/decrease of shoulder peak assigned as reversible change of degree of Mn-O covalency by ligand-to-metal charge transfer during the cycling. Although the mechanism of molecular orbital hybridization for the mixed-valent manganese oxides is not fully understood yet, a strong LMCT peak suggests there was a significantly large charge redistribution between Mn and O. The resulting charge delocalization between Mn and O is considered to contribute to the enhanced pseudocapacitance. The observation that the charge compensation for the electron exchange can be achieved at oxygen site as well as Mn site has never been reported for the pseudocapacitor system and much more fundamental works will be required to fully understand this phenomenon.

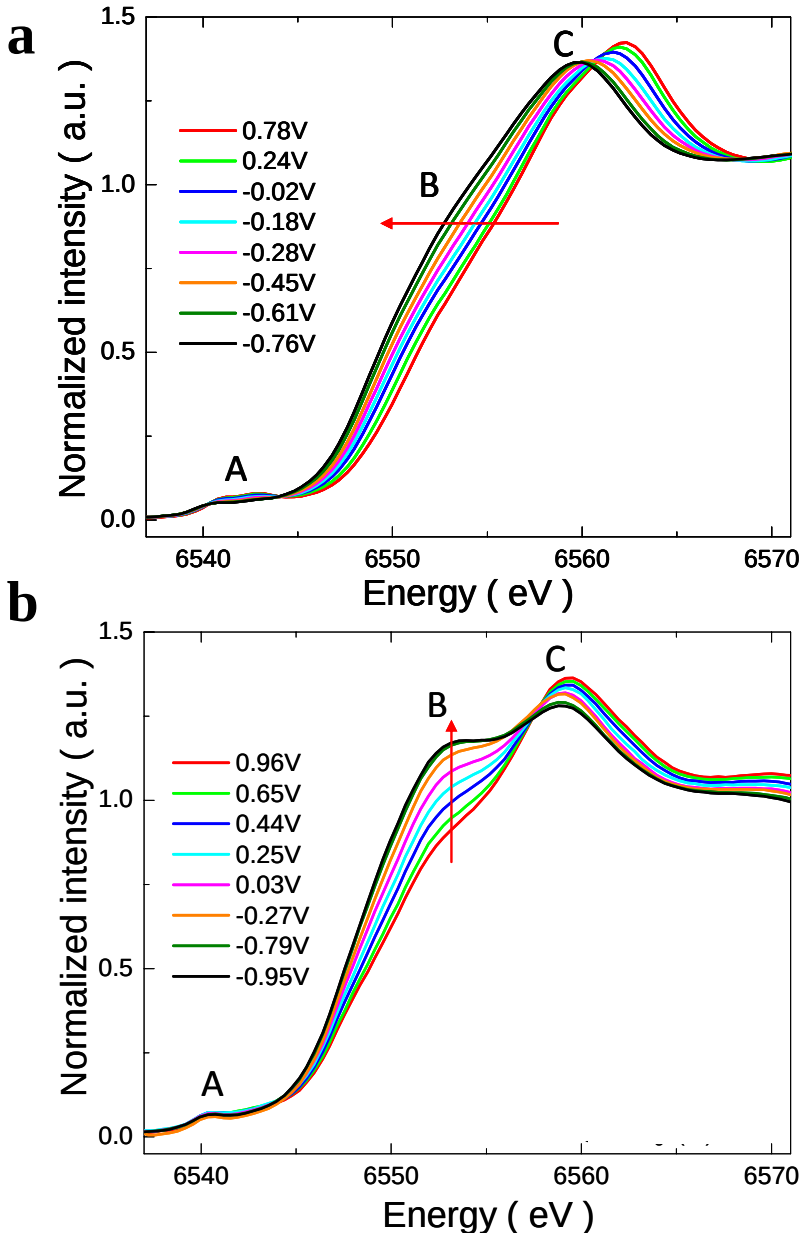

Figure 5.3. XANES spectra of the positive electrodes in the *in-situ* cell for **a,** the as-prepared and **b,** mixed-valent MnO_x electrode during discharge in 1.0M Na_2SO_4 electrolyte. Data courtesy of Dr. Nam and Dr. Yang at Brookhaven National Laboratory.

Although small intensity change of shoulder peak (B) in XANES spectra during charge-discharge were reported in the literature[87,88] for transition metal K-edges such as Co and Mn, it has never been observed that this spectral changes can play a dominating role over the continuous edge shift. The role of oxygen anions in transition metal oxides for charge compensation was previously argued for lithium battery electrodes. Aydinol et al. showed that more charge can be transferred to the oxygen anions than to the metal cations in the oxide upon intercalation of lithium ions[88,89].

5.2. Discussion on the Charge Storage Mechanism

While significantly improved performance has been demonstrated in this thesis, a fundamental question remains unanswered; how one can account for values above 3000 F/g? That is, what is the charge storage mechanism to provide this magnitude of capacitive charge storage? Previously, researchers achieved numbers on the order of 1200-1500 F/g which were consistent with one-electron redox for the materials being investigated. In this section, a possible mechanism for the enhanced pseudocapacitance of the mixed-valent MnO_x is proposed based on both *in-situ* XAS analysis coupled with electrochemical measurements.

5.2.1. Current Understanding of Charge Storage Mechanism

While considerable efforts have been devoted to the development of new materials for pseudocapacitors, the progress has been slow due to the lack of a clear understanding of the complex charge storage mechanisms. For example, Toupin *et al.*[44] used X-ray photoelectron spectroscopy to detect the change in oxidation state of Mn ions

from +4 to +3. However, the Na/Mn ratio for the reduced electrode was much lower than what was anticipated for the observed capacitance. Thus, they suggested that protons might also be involved and it is difficult to fully understand the mechanism. Recently, lattice expansion/contraction during cycling was reportedly observed by synchrotron-based XRD analyses, indicating that the pseudocapacitance of MnO_2 involves not only surface adsorption but also intercalation or insertion of cations into the bulk of manganese oxides[80]. Although any facile reaction involving reversible charge transfer (but not limited by diffusion) may be ideally suited for pseudocapacitance[3], it is often very difficult to fully understand the charge storage mechanism.

The theoretical specific capacitance of MnO_2 is 1,390 F/g for one electron transfer associated with the Mn^{4+}/Mn^{3+} redox reaction over a potential window of 0.8V. Indeed, high specific capacitances (up to 1,380 F/g) were reported for ultra-thin (tens to hundreds of nanometers thick) films of MnO_2[44]. This appears to be reasonable because a nanoscale thin-film of MnO_2 can overcome the limitations of (i) the poor electronic conductivity (10^{-5}-10^{-6} S/cm) of MnO_2 (by deposition on an excellent current collector) and (ii) low diffusivity of the inserted cations (by reducing the distances required for solid-state diffusion) to fully utilize all electrode material.

However, this estimation of theoretical capacitance is under the silent assumption that the MnO_2 is perfect and in a bulk form since the surface area and defects were not considered. If the manganese oxide is highly defected and have high specific surface area (like the nano-porous, multi-valent MnO_x in this case), the surfaces and the defects (on the surface or within the bulk) may act as additional reaction sites to accommodate charge, thus increasing the theoretical capacitance. Further, the nanostructure and the

defects may change the physicochemical properties of the manganese oxides, including the ionic and electronic conductivity, the surface reactivity, and the capacity for insertion of ions from electrolyte. These properties may in turn affect the performance significantly since the practical (or obtainable) capacitance is often limited by the kinetics.

Many factors can influence the charge storage process, including porosity, morphology, crystal structure, and texture/orientation. For example, it was claimed in the literature that amorphous MnO_2 involves only surface adsorption while crystalline MnO_2 involves not only surface adsorption but also bulk intercalation of alkaline cations and/or protons from the electrolyte[50,96]. It was demonstrated that the 3D spinel structure showed the highest capacitance, followed by the 2D layer birnessite structure[97]. It was also revealed that the specific capacitance can be better correlated with the ionic conductivity of the MnO_2, which is clearly related to the crystal structure and microstructure, than simply surface area[97]. Therefore, it is necessary to consider many factors contributing to the pseudocapacitance in order to comprehend the charge storage mechanisms responsible of nanostructured, porous, mixed-valent MnO_x with high surface area.

5.2.2. Redox Reactions at Mn and O sites

Synchrotron-based XRD and XAS analyses suggest that the bulk phase of the mixed-valent MnO_x is similar to Mn_3O_4 (but not exactly the same). Thus, if the redox reactions of Mn ions are the only charge storage mechanism, the theoretical specific capacitance of Mn_3O_4 should be 1,580 F/g over a potential window of 0.8V for one electron transfer per Mn ion. Since the mixed-valent MnO_x electrode displayed a capacitance of ~2,500F/g in 1M Na_2SO_4 electrolyte and ~3,900F/g in 1M H_2SO_4

electrolyte, the number of electrons transferred should be ~1.5 and ~2.5 per Mn ion, respectively. In other words, the average oxidation state of Mn ions in the MnO_x electrode would have to change by 1.5 and 2.5 in Na_2SO_4 and H_2SO_4 electrolyte solution, respectively. However, *in-situ* XAS analyses suggest that the actual changes in oxidation state of Mn ions are only ~0.4 (far smaller that ~1.5) in 1M Na_2SO_4, implying that additional charge compensation mechanism(s) may be significant.

Based on *in-situ* synchrotron XAS experiments, it seems that the charge compensation for the electron exchange can be achieved at the oxygen site as well as Mn site, which has never before been reported for pseudocapacitor electrodes. As discussed previously, unique evolution of a shoulder peak was observed for mixed-valent MnO_x, which is related to the ligand-to-metal charge transfer process, in addition to the slight edge shift towards lower energy in the discharge process, which indicates the decrease of average oxidation state of Mn ions. The increased shoulder peak intensity indicates the increased degree of covalent character of Mn(3d)-O(2p) bonding, clearly showing that a large portion of the charge compensation during discharge might be originated from the hole state redistribution towards the oxygen sites, rather than electrons toward the Mn ions (as in the case of the as-prepared sample). The unique atomic and electronic structure of the nanostructured, mixed-valent MnO_x may allow this additional charge compensation mechanism, which is not observed in MnO_2.

There are several charge compensation mechanisms for pseudocapacitive behavior in addition to the conventional redox reactions of metal cations. It is believed that the situation is much more complex: part of the capacitance may be associated with the charge storage at Mn and O sites, which were probed by *in-situ* X-ray analysis.

However, the majority of the capacitance is still associated with possible charge storage at defects with ions and the electron pilling up at the surfaces, which depend on the detailed surface defects and the double layer structure of the electrode surface.

5.2.3. Defects as Additional Charge Storage Sites

It is believed that the defects created during the formation of multi-valent MnO_x may act as active sites for surface charge storage; the so-called surface/interface storage mechanism may play an important role in the nanoporous electrode[40]. The co-existence of aliovalent cations (Mn^{2+}, Mn^{3+}, and Mn^{4+}) may facilitate the formation of more ionic defects (e.g., vacancies and misplaced ions) and electronic defects (electrons and holes), thus altering the electronic, ionic, and catalytic properties of the manganese oxides. These defects may accelerate the kinetics of the surface redox reactions. Also, the mismatches induced by structural differences among different manganese oxide phases may produce additional defects (cavities, stacking faults, etc.), thus facilitating the formation of porous nano-architectures that may enhance the transport of charged species and extend the reaction sites from the surface to the subsurface of electrode.

Recent theoretical studies predicted that photoconductivity of MnO_2 can be enhanced by introducing Ruetschi defects or protonated Mn(IV) vacancies, suggesting that electronic properties can be tailored by tuning the defect structure during synthesis. Similar effect has also been observed in batteries. For example, a disordered carbon showed much larger capacity (sometimes larger than 1,100 mAh/g) than graphite (with theoretical capacity of 372 mAh/g)[40]. While the theoretical capacity of ordered graphite is well known because only certain crystallographic sites can be occupied by lithium atom,

the theoretical capacity of disordered carbons can not be predicted because the defects make significant contributions to capacity. The surface/interface storage mechanisms are also important for graphenes with certain defects or functional groups on the surface, which can act as additional reaction sites to accommodate lithium and hence increase capacity. This surface/interface storage mechanism would be more important in nanoscale regime. Recent first-principles study clearly showed the distinction between batteries and electrochemical capacitors became ambiguous as the size of material decreases to less than 10 nm and predicted that conventional battery electrode materials can exhibit the transition from battery-like behavior to capacitor-like behavior[98].

5.2.4. Roles of Mixed-Valence in Enhanced Charge Transfer

While the effect of multi-valence on chemical reactivity is still not fully understood and much more intensive studies are required to gain more insight, it is also shown that the presence of two-electron mixed valence itself can lead to faster charge-transfer. For instance, Professor Daniel G. Nocera at MIT described in his recent article[99] that

> *"Mixed valency in molecular compounds is typically accommodated at metal centers whose formal oxidation states differ by one. In these complexes, reactivity is confined to single-electron oxidations and reductions of the constituent* M^n *and* M^{n+1} *centers, respectively. Extrapolating from this one-electron formalism, two-electron mixed valency of bimetallic cores provides entry into multielectron oxidation−reduction chemistry. Redox cooperativity may be established between the individual metal centers of a* $M^n \cdots M^{n+2}$ *mixed-valence core such that two-*

electron oxidations may be promoted at a M^{n+2} center and two-electron reductions may be promoted at a M^{n} center".

It was also claimed that two-electron mixed valence can be a useful design concept for the development of multi-electron reaction schemes. It is believed that ligands in the mixed-valent compounds may play very important roles in effectively bridging the electron acceptors and donors.

5.2.5. Roles of Enhanced Double-Layer Capacitance

Moreover, as the dramatically enlarged surface area was observed during the formation of mixed-valent MnO_x, it is necessary to also consider the double-layer capacitance, which is very hard to calculate theoretically unless we know precisely the surface double layer structure. For example, the adsorption of ions on electrode surface does not always result in change in oxidation state or phase of the electrode materials. Let's take carbon electrode as an example. High-surface area activated carbons have been widely used as the electrode for electrochemical double layer capacitors, demonstrating a specific capacitance of ~400 F/g in aqueous electrolytes. Yet, this capacity can not be predicted by change in oxidation state of carbon atoms or phases in the carbon electrodes. Similarly, when a metal is used as the electrode, neither the oxidation state nor the phase has to change to store charge (adsorb ions) on the surface. The charge of ions adsorbed on electrode surface is balanced by pilling up electron or holes at the electrode surfaces to form a double layer. The capacity due to this process is determined by the solid-liquid

interface, which is much less understood. Chmiola et al. reported the anomalous increase in carbon at pore size less than 1 nm[6]. This anomalous enhancement by desolvation might also play some role in the nano-porous mixed-valent MnO_x, which has average pore size of 2 nm whereas the tunnel size of alpha MnO_2 is known to be less than 0.5 nm.

It is also necessary to consider the electronic structure of the surface. Double-layer capacitance generally results from the potential-dependence of the charge densities stored on the surface electrostatically. For transition metal oxides, the charge accumulated on surfaces is due to excess or deficient electrons (or holes) in conduction (or valence) band, which is counter-balanced by the cations or anions accumulated near the interfaces from the electrolyte. If there is a variation in electron density on the surface, a corresponding contribution (referred to "metal contribution") arises to the double-layer capacitance, although this contribution is not generally included in the classical treatments of the double layer. Using *in-situ* XAS, it was observed that a strong LMCT peak developed during the formation of mixed-valent MnO_x. Although the mechanism of molecular orbital hybridization for the mixed-valent MnO_x is not yet fully understood, a strong LMCT peak suggests there was significant charge redistribution between Mn and O. The resulting unique atomic and electronic structure and possible charge delocalization between Mn and O may alter the double layer structure/capacitance on the surface, contributing to the enhanced capacitance.

5.3. Summary

In this chapter, we have discussed the redox occurring on both the Mn and the O sites and the potential roles of defects and double layer capacitance, all of which can

contribute to the enhanced capacitance. The traditional notion that the observed capacitance must correspond to a change in oxidation states (or redox reaction) of Mn ion is questionable; the projected "theoretical" capacitance based on one-electron redox reactions of Mn ions represents only part, not all, of the charge stored on the surface or subsurface of electrodes. In fact, this has been mentioned in recent publications. For example, Professor Bruce Dunn et al.[3] at UCLA described in their recent article published in Nature Materials 2010,

> *"Interestingly, 150 uF/cm^2 of charge corresponds approximately to 4.5 e- per surface molybdenum assuming only redox pseudocapacitance. This value is chemically unreasonable and further argues that surface pseudocapacitance is not the only mechanism working in these materials."*

Also, Dr. Conway described in his monograph *"Electrochemical supercapacitors: Scientific fundamentals and technological applications"* that there would be 1-2.5 electron per atom of accessible surface in pseudocapacitors[5]. His explanation was also cited in recent review paper[2].

In conclusion, the enhanced performance is attributed to the unique mixed-valent (2+, 3+, and 4+) manganese oxides of porous nano-architectures, which may facilitate rapid mass transport and enhance surface double-layer capacitance, while promoting facile redox reactions associated with charge storage at both Mn and O sites, leading to unprecedented levels of energy and power density. In particular, the implication that significant amount of charge can be stored at the O sites of nanostructured MnO_x, as suggested by *in-situ* X-ray absorption spectroscopy, directly challenges the traditional notion that pseudocapacitive behavior is associated mainly with redox reactions of

cations and offers potential for taking advantages of these new energy storage mechanisms (in addition to those associated with redox reactions of cations) in rational design of a new-generation pseudocapacitor materials.

CHAPTER 6

CONCLUDING REMARKS

6.1. Conclusions

In this thesis, novel electrodes with tailored architecture and controlled mixed-phases were prepared by depositing a thin, conformal coating of nanostructured, mixed-valent MnO_x onto porous carbon fiber paper via a simple solution deposition process at low temperature. After a controlled annealing process, several distinctly different phases were formed on the surface in addition to the bulk Mn_3O_4 phase. Both *in-situ* and *ex-situ* synchrotron-enabled X-ray diffraction/absorption methods and advanced electron microscopy have been used to determine that the unique "surface" chemistry is very different from that of the "bulk". It is a completely new nanostructure of MnO_x: a mixed-phase, multi-valent MnO_x with graded oxidation state and nano-porous architecture.

Electrochemical capacitors constructed from these electrodes showed the highest specific capacitance (3,856 F/g) of all materials investigated, superior rate capability, and enhanced cycling stability (little degradation after 200,000 cycles). The demonstrated performance is far superior to any previously reported for electrochemical capacitors. To investigate the charge storage mechanism, *in-situ* X-ray absorption spectroscopy was carried out on the mixed-valent MnO_x electrode materials during discharge. In particular, it was demonstrated that significant amounts of charge can be stored at the O sites of nanostructured MnO_x, leading to unprecedented levels of energy and power density.

These results directly challenge the traditional notion that pseudocapacitive behavior originates primarily from redox reactions of cations (or changes in oxidation

states of cations) in electrode materials during operation. These results also provide new insights into some novel charge storage mechanisms (in addition to those associated with redox reactions of cations) which are inherent to nanostructured, mixed-valent MnO_x, which have never before been reported for pseudocapacitors.

The results demonstrated in this thesis suggest that electrochemical capacitors can achieve high energy density, offering potential for reaching energy densities comparable to those of existing batteries, while maintaining high rate capabilities and excellent cycling performance of EDLCs. This is accomplished by deposition of thin films of mixed-valent manganese oxides with porous nano-architecture, enabling multiple charge storage mechanisms with much smaller internal resistance and highly reversible, faster charge transfer kinetics.

Creation of nanostructured, mixed-valent electrode materials would represent one of the most attractive strategies to dramatically enhance electrochemical performance, including capacity (or capacitance), rate capability, and cycling life of electrodes. Although mixed-valent manganese oxides were investigated as active materials in this study, other transition metal oxides could also be explored using a similar method to design functional materials with significantly enhanced electrochemical performances.

6.2. Recommendations

While significantly improved performance has been demonstrated in this thesis, high specific capacitance (thus energy density) was achieved with a nanoscale coating of mixed-valent MnO_x. Although the battery community often only considers active materials in calculating the energy density for performance comparisons with those

reported in journal articles, the energy density projected from an electrode structure, not a device, may not be fairly compared with those of existing batteries. However, the mixed-valent MnO_x presented in this dissertation shows great potential to provide an order of magnitude increase in practical energy density without penalizing power density. If a given electrode material has attractive intrinsic properties, it is expected that high energy density can, in principle, be achieved through optimization of capacitor design, although design parameters (current collectors, substrates and other components) can limit the ultimate practical capacitance (thus energy density).

Although this is largely an engineering effort to further optimize energy density, it is still necessary to explore ways to also increase practical capacitances, energy and power densities. The author believes that MnO_x coatings must be thin to offer the best possible power density. Therefore, one effective approach to increasing practical energy density (e.g. loading) without compromising the specific capacitance or rate capability is to reduce the diameter of the carbon fibers and increase the surface area of CFP. Also, energy and power density could be further improved by matching suitable counter electrodes in an asymmetric cell design.

More complete understanding on the atomic/electronic structure of mixed-valent compounds and their charge transfer/storage mechanisms will be necessary to achieving rational design of better electrode materials and structures for efficient energy storage and conversion. It is anticipated that a simple approach to create nanostructured, mixed-valent compounds demonstrated in this dissertation may also guide the design of high-performance electrode materials for other electrochemical energy devices such as batteries and fuel cells.

Advances in computational methodologies will be also necessary to provide the atomic, molecular and continuum-level insights required to establish the fundamental criteria for next-generation electrical energy storage systems with higher energy and power densities, faster recharge times, and longer lifetimes than existing technologies. As demonstrated in this thesis, combining the power of computational capabilities and *in-situ* characterization tools could open up entirely new avenues for developing novel multifunctional materials with the tailored physical and chemical properties, leading to greatly enhanced performance.

REFERENCES

1 Simon, P. & Gogotsi, Y. Materials for electrochemical capacitors. *Nat. Mater.* **7**, 845-854, doi:10.1038/nmat2297 (2008).

2 Hall, P. J. *et al.* Energy storage in electrochemical capacitors: designing functional materials to improve performance. *Energy & Environmental Science* **3**, 1238-1251 (2010).

3 Brezesinski, T., Wang, J., Tolbert, S. H. & Dunn, B. Ordered mesoporous alpha-MoO3 with iso-oriented nanocrystalline walls for thin-film pseudocapacitors. *Nat. Mater.* **9**, 146-151, doi:10.1038/nmat2612 (2010).

4 Whittingham, M. S. Materials challenges facing electrical energy storage. *MRS Bull.* **33**, 411-419 (2008).

5 Conway, B. E. *Electrochemical Supercapacitors*. (Kluwer-Academic, 1999).

6 Chmiola, J. *et al.* Anomalous increase in carbon capacitance at pore sizes less than 1 nanometer. *Science* **313**, 1760-1763, doi:10.1126/science.1132195 (2006).

7 Arico, A. S., Bruce, P., Scrosati, B., Tarascon, J. M. & Van Schalkwijk, W. Nanostructured materials for advanced energy conversion and storage devices. *Nat. Mater.* **4**, 366-377, doi:10.1038/nmat1368 (2005).

8 *Basic research needs for electrical energy storage* (Office of Basic Energy Sciences, U.S. Department of Energy, 2007).

9 Baxter, J. *et al.* Nanoscale design to enable the revolution in renewable energy. *Energy & Environmental Science* **2**, 559-588, doi:10.1039/b821698c (2009).

10 Fernandez-Garcia, M., Martinez-Arias, A., Hanson, J. C. & Rodriguez, J. A. Nanostructured oxides in chemistry: Characterization and properties. *Chem. Rev.* **104**, 4063-4104, doi:10.1021/cr030032f (2004).

11 Millot, N. *et al.* Particle size dependency of ternary diagrams at the nanometer scale: Evidence of TiO2 clusters in Fe-based spinels. *J. Phys. Chem. B* **107**, 5740-5750, doi:10.1021/jp022312p (2003).

12 Zhang, H. Z. & Banfield, J. F. Thermodynamic analysis of phase stability of nanocrystalline titania. *J. Mater. Chem.* **8**, 2073-2076 (1998).

13 McHale, J. M., Auroux, A., Perrotta, A. J. & Navrotsky, A. Surface energies and thermodynamic phase stability in nanocrystalline aluminas. *Science* **277**, 788-791 (1997).

14 Ayyub, P., Multani, M., Barma, M., Palkar, V. R. & Vijayaraghavan, R. SIZE-INDUCED STRUCTURAL PHASE-TRANSITIONS AND HYPERFINE PROPERTIES OF MICROCRYSTALLINE FE2O3. *Journal of Physics C-Solid State Physics* **21**, 2229-2245 (1988).

15 Hernandez-Alonso, M. D. *et al.* Confinement effects in quasi-stoichiometric CeO2 nanoparticles. *Physical Chemistry Chemical Physics* **6**, 3524-3529, doi:10.1039/b403202k (2004).

16 Nutzenadel, C., Zuttell, A., Chartouni, D., Schmid, G. & Schlapbach, L. Critical size and surface effect of the hydrogen interaction of palladium clusters. *European Physical Journal D* **8**, 245-250 (2000).

17 Roduner, E. Size matters: why nanomaterials are different. *Chem. Soc. Rev.* **35**, 583-592, doi:10.1039/b502142c (2006).

18 Kosacki, I., Petrovsky, V. & Anderson, H. U. Band gap energy in nanocrystalline ZrO2 : 16%Y thin films. *Appl. Phys. Lett.* **74**, 341-343 (1999).

19 Albaret, T., Finocchi, F. & Noguera, C. First principles simulations of titanium oxide clusters and surfaces. *Faraday Discussions* **114**, 285-304 (1999).

20 Anchell, J. L. & Hess, A. C. H2O dissociation at low-coordinated sites on (MgO)(n) clusters, n=4,8. *J. Phys. Chem.* **100**, 18317-18321 (1996).

21 Rodriguez, J. A., Chaturvedi, S., Kuhn, M. & Hrbek, J. Reaction of H2S and S-2 with metal/oxide surfaces: Band-gap size and chemical reactivity. *J. Phys. Chem. B* **102**, 5511-5519 (1998).

22 FernandezGarcia, M., Conesa, J. C. & Illas, F. Effect of the Madelung potential value and symmetry on the adsorption properties of adsorbate/oxide systems. *Surface Science* **349**, 207-215 (1996).

23 Ji, X. L., Lee, K. T. & Nazar, L. F. A highly ordered nanostructured carbon-sulphur cathode for lithium-sulphur batteries. *Nat. Mater.* **8**, 500-506, doi:10.1038/nmat2460 (2009).

24 Maier, J. Nanoionics: ion transport and electrochemical storage in confined systems. *Nat. Mater.* **4**, 805-815, doi:10.1038/nmat1513 (2005).

25 Gleiter, H. NANOCRYSTALLINE MATERIALS. *Progress in Materials Science* **33**, 223-315 (1989).

26 Kumar, K. S., Van Swygenhoven, H. & Suresh, S. Mechanical behavior of nanocrystalline metals and alloys. *Acta Materialia* **51**, 5743-5774, doi:10.1016/j.actamat.2003.08.032 (2003).

27 Meyers, M. A., Mishra, A. & Benson, D. J. Mechanical properties of nanocrystalline materials. *Progress in Materials Science* **51**, 427-556, doi:10.1016/j.pmatsci.2005.08.003 (2006).

28 He, G., Eckert, J., Loser, W. & Schultz, L. Novel Ti-base nanostructure-dendrite composite with enhanced plasticity. *Nat. Mater.* **2**, 33-37, doi:10.1038/nmat792 (2003).

29 Schiotz, J., Di Tolla, F. D. & Jacobsen, K. W. Softening of nanocrystalline metals at very small grain sizes. *Nature* **391**, 561-563 (1998).

30 Kumar, K. S., Suresh, S., Chisholm, M. F., Horton, J. A. & Wang, P. Deformation of electrodeposited nanocrystalline nickel. *Acta Materialia* **51**, 387-405, doi:10.1016/s1359-6454(02)00421-4 (2003).

31 Chen, M. W. *et al.* Deformation twinning in nanocrystalline aluminum. *Science* **300**, 1275-1277, doi:10.1126/science.1083727 (2003).

32 Budrovic, Z., Van Swygenhoven, H., Derlet, P. M., Van Petegem, S. & Schmitt, B. Plastic deformation with reversible peak broadening in nanocrystalline nickel. *Science* **304**, 273-276 (2004).

33 Champion, Y. *et al.* Near-perfect elastoplasticity in pure nanocrystalline copper. *Science* **300**, 310-311 (2003).

34 Robertson, A. D., Armstrong, A. R. & Bruce, P. G. Layered LixMn1-yCoyO2 intercalation electrodes-influence of ion exchange on capacity and structure upon cycling. *Chem. Mat.* **13**, 2380-2386, doi:10.1021/cm000965h (2001).

35 Guo, Y. G., Hu, J. S. & Wan, L. J. Nanostructured Materials for Electrochemical Energy Conversion and Storage Devices (vol 20, pg 2878, 2008). *Advanced Materials* **20**, 4384-4384, doi:10.1002/adma.200800627 (2008).

36 Hu, Y. S., Kienle, L., Guo, Y. G. & Maier, J. High lithium electroactivity of nanometer-sized rutile TiO2. *Advanced Materials* **18**, 1421-1426, doi:10.1002/adma.200502723 (2006).

37 Jamnik, J. & Maier, J. Nanocrystallinity effects in lithium battery materials - Aspects of nano-ionics. Part IV. *Physical Chemistry Chemical Physics* **5**, 5215-5220, doi:10.1039/b309130a (2003).

38 Balaya, P. Size effects and nanostructured materials for energy applications. *Energy & Environmental Science* **1**, 645-654, doi:10.1039/b809078p (2008).

39 Wang, Q., Li, H., Chen, L. Q. & Huang, X. J. Monodispersed hard carbon spherules with uniform nanopores. *Carbon* **39**, 2211-2214 (2001).

40 Kaskhedikar, N. A. & Maier, J. Lithium Storage ion Carbon Nanostructures. *Advanced Materials* **21**, 2664-2680, doi:10.1002/adma.200901079 (2009).

41 Amatucci, G. G. & Pereira, N. Fluoride based electrode materials for advanced energy storage devices. *Journal of Fluorine Chemistry* **128**, 243-262, doi:10.1016/j.jfluchem.2006.11.016 (2007).

42 Hou, Y., Cheng, Y. W., Hobson, T. & Liu, J. Design and Synthesis of Hierarchical MnO2 Nanospheres/Carbon Nanotubes/Conducting Polymer Ternary Composite for High Performance Electrochemical Electrodes. *Nano Lett.* **10**, 2727-2733, doi:10.1021/nl101723g (2010).

43 Lee, S. W., Kim, J., Chen, S., Hammond, P. T. & Shao-Horn, Y. Carbon Nanotube/Manganese Oxide Ultrathin Film Electrodes for Electrochemical Capacitors. *ACS Nano* **4**, 3889-3896, doi:10.1021/nn100681d (2010).

44 Toupin, M., Brousse, T. & Belanger, D. Charge storage mechanism of MnO2 electrode used in aqueous electrochemical capacitor. *Chem. Mat.* **16**, 3184-3190, doi:10.1021/cm049649j (2004).

45 Raymundo-Pinero, E., Khomenko, V., Frackowiak, E. & Beguin, F. Performance of manganese oxide/CNTs composites as electrode materials for electrochemical capacitors. *J. Electrochem. Soc.* **152**, A229-A235, doi:10.1149/1.1834913 (2005).

46 Chou, S. L., Wang, J. Z., Chew, S. Y., Liu, H. K. & Dou, S. X. Electrodeposition of MnO2 nanowires on carbon nanotube paper as free-standing, flexible electrode for supercapacitors. *Electrochem. Commun.* **10**, 1724-1727, doi:10.1016/j.elecom.2008.08.051 (2008).

47 Fischer, A. E., Pettigrew, K. A., Rolison, D. R., Stroud, R. M. & Long, J. W. Incorporation of homogeneous, nanoscale MnO2 within ultraporous carbon structures via self-limiting electroless deposition: Implications for electrochemical capacitors. *Nano Lett.* **7**, 281-286, doi:10.1021/nl062263i (2007).

48 Lang, X. Y., Hirata, A., Fujita, T. & Chen, M. W. Nanoporous metal/oxide hybrid electrodes for electrochemical supercapacitors. *Nat. Nanotechnol.* **6**, 232-236, doi:10.1038/nnano.2011.13 (2011).

49 Post, J. E. Manganese oxide minerals: Crystal structures and economic and environmental significance. *Proc. Natl. Acad. Sci. U. S. A.* **96**, 3447-3454 (1999).

50 Devaraj, S. & Munichandraiah, N. Effect of crystallographic structure of MnO2 on its electrochemical capacitance properties. *Journal of Physical Chemistry C* **112**, 4406-4417, doi:10.1021/jp7108785 (2008).

51 Tian, Z. R. *et al.* Manganese oxide mesoporous structures: Mixed-valent semiconducting catalysts. *Science* **276**, 926-930 (1997).

52 Cao, H. & Suib, S. L. Highly efficient heterogeneous photooxidation of 1-propanol to acetone with amorphous manganese oxide catalysts. *J. Am. Chem. Soc.* **116**, 5334-5342 (1994).

53 Shen, Y. F. *et al.* Manganese oxide octahedral molecular sieves: preparation, characterization, and applications. *Science* **260**, 511-515 (1993).

54 Hankache, J. & Wenger, O. S. Organic Mixed Valence. *Chem. Rev.* **111**, 5138-5178, doi:10.1021/cr100441k (2011).

55 Young, C. G. MIXED-VALENCE COMPOUNDS OF THE EARLY TRANSITION-METALS. *Coordination Chemistry Reviews* **96**, 89-251, doi:10.1016/0010-8545(89)80032-3 (1989).

56 Varma, C. M. MIXED-VALENCE COMPOUNDS. *Reviews of Modern Physics* **48**, 219-238, doi:10.1103/RevModPhys.48.219 (1976).

57 Richardson, D. E. & Taube, H. Mixed-valence molecules: Electronic delocalization and stabilization. *Coordination Chemistry Reviews* **60**, 107-129, doi:10.1016/0010-8545(84)85063-8 (1984).

58 Robin, M. B. & Day, P. in *Advances in Inorganic Chemistry* Vol. Volume 10 (eds H. J. Emeléus & A. G. Sharpe) 247-422 (Academic Press, 1968).

59 Garcia, J. & Subias, G. The Verwey transition - a new perspective. *Journal of Physics-Condensed Matter* **16**, R145-R178, doi:10.1088/0953-8984/16/7/r01 (2004).

60 Earnshaw, A. & Greenwood, N. *Chemistry of the Elements*. 2nd edn, (Butterworth-Heinemann, 1997).

61 Schulz, W. W. & Wentzcovitch, R. M. ELECTRONIC BAND-STRUCTURE AND BONDING IN NB3O3. *Physical Review B* **48**, 16986-16991, doi:10.1103/PhysRevB.48.16986 (1993).

62 Brunschwig, B. S., Creutz, C. & Sutin, N. Optical transitions of symmetrical mixed-valence systems in the Class II-III transition regime. *Chem. Soc. Rev.* **31**, 168-184 (2002).

63 Nelsen, S. F. "Almost Delocalized" Intervalence Compounds. *Chemistry – A European Journal* **6**, 581-588, doi:10.1002/(sici)1521-3765(20000218)6:4<581::aid-chem581>3.0.co;2-e (2000).

64 Winter, M. & Brodd, R. J. What are batteries, fuel cells, and supercapacitors? *Chem. Rev.* **104**, 4245-4269, doi:10.1021/cr020730k (2004).

65 Chen, Y., Liu, C., Li, F. & Cheng, H. M. Preparation of single-crystal alpha-MnO2 nanorods and nanoneedles from aqueous solution. *J. Alloy. Compd.* **397**, 282-285, doi:10.1016/j.jallcom.2004.12.049 (2005).

66 Ragupathy, P. *et al.* Remarkable Capacity Retention of Nanostructured Manganese Oxide upon Cycling as an Electrode Material for Supercapacitor. *Journal of Physical Chemistry C* **113**, 6303-6309, doi:10.1021/jp811407q (2009).

67 Xu, M. W., Zhao, D. D., Bao, S. J. & Li, H. L. Mesoporous amorphous MnO2 as electrode material for supercapacitor. *J. Solid State Electrochem.* **11**, 1101-1107, doi:10.1007/s10008-006-0246-4 (2007).

68 Subramanian, V., Zhu, H. W. & Wei, B. Q. Synthesis and electrochemical characterizations of amorphous manganese oxide and single walled carbon nanotube composites as supercapacitor electrode materials. *Electrochem. Commun.* **8**, 827-832, doi:10.1016/j.elecom.2006.02.027 (2006).

69 Lee, H. Y. & Goodenough, J. B. Supercapacitor behavior with KCl electrolyte. *Journal of Solid State Chemistry* **144**, 220-223 (1999).

70 Gao, T. *et al.* Microstructures and spectroscopic properties of cryptomelane-type manganese dioxide nanofibers. *Journal of Physical Chemistry C* **112**, 13134-13140, doi:10.1021/jp804924f (2008).

71 Hu, C. C. & Tsou, T. W. Ideal capacitive behavior of hydrous manganese oxide prepared by anodic deposition. *Electrochem. Commun.* **4**, 105-109 (2002).

72 Dubal, D. P., Dhawale, D. S., Salunkhe, R. R. & Lokhande, C. D. Conversion of Chemically Prepared Interlocked Cubelike Mn(3)O(4) to Birnessite MnO(2) Using Electrochemical Cycling. *J. Electrochem. Soc.* **157**, A812-A817, doi:10.1149/1.3428675 (2010).

73 Dubal, D. P., Dhawale, D. S., Salunkhe, R. R. & Lokhande, C. D. A novel chemical synthesis of Mn(3)O(4) thin film and its stepwise conversion into birnessite MnO(2) during super capacitive studies. *J. Electroanal. Chem.* **647**, 60-65, doi:10.1016/j.jelechem.2010.05.010 (2010).

74 Wang, H., Casalongue, H. S., Liang, Y. & Dai, H. Ni(OH)2 Nanoplates Grown on Graphene as Advanced Electrochemical Pseudocapacitor Materials. *J. Am. Chem. Soc.* **132**, 7472-7477, doi:10.1021/ja102267j (2010).

75 Hu, C. C., Chen, W. C. & Chang, K. H. How to achieve maximum utilization of hydrous ruthenium oxide for supercapacitors. *J. Electrochem. Soc.* **151**, A281-A290, doi:10.1149/1.1639020 (2004).

76 Oswald, H. R., Feitknec.W & Wampetic.Mj. Crystal Data of MN5O8 AND CD2MN3O8. *Nature* **207**, 72-& (1965).

77 Park, Y. J. & Doeff, M. A. Synthesis and electrochemical characterization of M2Mn3O8 (M=Ca, Cu) compounds and derivatives. *Solid State Ion.* **177**, 893-900, doi:10.1016/j.ssi.2006.02.001 (2006).

78 Xu, C. J., Du, H. D., Li, B. H., Kang, F. Y. & Zeng, Y. Q. Capacitive Behavior and Charge Storage Mechanism of Manganese Dioxide in Aqueous Solution Containing Bivalent Cations. *J. Electrochem. Soc.* **156**, A73-A78, doi:10.1149/1.3021013 (2009).

79 Chabre, Y. & Pannetier, J. STRUCTURAL AND ELECTROCHEMICAL PROPERTIES OF THE PROTON GAMMA-MNO2 SYSTEM. *Progress in Solid State Chemistry* **23**, 1-130, doi:10.1016/0079-6786(94)00005-2 (1995).

80 Kuo, S. L. & Wu, N. L. Investigation of pseudocapacitive charge-storage reaction of MnO(2).nH(2)O supercapacitors in aqueous electrolytes. *J. Electrochem. Soc.* **153**, A1317-A1324, doi:10.1149/1.2197667 (2006).

81 Dean, J. A. *Lange's Handbook of Chemistry*. (McGraw-Hill, 1992).

82 Wen, S., Lee, J. W., Yeo, I. H., Park, J. & Mho, S. The role of cations of the electrolyte for the pseudocapacitive behavior of metal oxide electrodes, MnO2 and RuO2. *Electrochim. Acta* **50**, 849-855, doi:10.1016/j.electacta.2004.02.056 (2004).

83 Konningsberger, D. C. & Prins, R. *X-Ray Absorption: Principles, Applications, Techniques of EXAFS, SEXAFS and XANES*. (Wiley, 1988).

84 Ravel, B. & Newville, M. ATHENA, ARTEMIS, HEPHAESTUS: data analysis for X-ray absorption spectroscopy using IFEFFIT. *J. Synchrot. Radiat.* **12**, 537-541, doi:10.1107/s0909049505012719 (2005).

85 Kim, M. G. & Yo, C. H. X-ray absorption spectroscopic study of chemically and electrochemically Li ion extracted LiyCo0.85Al0.15O2 compounds. *J. Phys. Chem. B* **103**, 6457-6465, doi:10.1021/jp990753b (1999).

86 Horne, C. R. *et al.* Electronic structure of chemically-prepared LixMn2O4 determined by Mn X-ray absorption and emission spectroscopies. *J. Phys. Chem. B* **104**, 9587-9596, doi:10.1021/jp994475s (2000).

87 Yoon, W. S. *et al.* Investigation of the charge compensation mechanism on the electrochemically Li-ion deintercalated Li1-xCo1/3Ni1/3Mn1/3O2 electrode system by combination of soft and hard x-ray absorption spectroscopy. *J. Am. Chem. Soc.* **127**, 17479-17487, doi:10.1021/ja0530568 (2005).

88 Kim, M. G., Shin, H. J., Kim, J. H., Park, S. H. & Sun, Y. K. XAS investigation of inhomogeneous metal-oxygen bond covalency in bulk and surface for charge

compensation in li-ion battery cathode Li Ni1/3Co1/3Mn1/3 O-2 material. *J. Electrochem. Soc.* **152**, A1320-A1328, doi:10.1149/1.1926647 (2005).

89 Aydinol, M. K., Kohan, A. F., Ceder, G., Cho, K. & Joannopoulos, J. Ab initio study of lithium intercalation in metal oxides and metal dichalcogenides. *Physical Review B* **56**, 1354-1365, doi:10.1103/PhysRevB.56.1354 (1997).

90 Kresse, G. & Furthmuller, J. Efficient iterative schemes for ab initio total-energy calculations using a plane-wave basis set. *Physical Review B* **54**, 11169-11186, doi:10.1103/PhysRevB.54.11169 (1996).

91 Kresse, G. & Joubert, D. From ultrasoft pseudopotentials to the projector augmented-wave method. *Physical Review B* **59**, 1758-1775, doi:10.1103/PhysRevB.59.1758 (1999).

92 Perdew, J. P., Burke, K. & Ernzerhof, M. Generalized gradient approximation made simple. *Physical Review Letters* **77**, 3865-3868, doi:10.1103/PhysRevLett.77.3865 (1996).

93 Dudarev, S. L., Botton, G. A., Savrasov, S. Y., Humphreys, C. J. & Sutton, A. P. Electron-energy-loss spectra and the structural stability of nickel oxide: An LSDA+U study. *Physical Review B* **57**, 1505-1509, doi:10.1103/PhysRevB.57.1505 (1998).

94 Franchini, C., Podloucky, R., Paier, J., Marsman, M. & Kresse, G. Ground-state properties of multivalent manganese oxides: Density functional and hybrid density functional calculations. *Physical Review B* **75**, doi: 10.1103/PhysRevB.75.195128 (2007).

95 Bader, R. F. W. *Atoms in Molecules - A Quantum Theory*. (Oxford University Press, 1990).

96 Ragupathy, P., Vasan, H. N. & Munichandraiah, N. Synthesis and characterization of nano-MnO2 for electrochemical supercapacitor studies. *J. Electrochem. Soc.* **155**, A34-A40, doi:10.1149/1.2800163 (2008).

97 Ghodbane, O., Pascal, J. L. & Favier, F. Microstructural Effects on Charge-Storage Properties in MnO(2)-Based Electrochemical Supercapacitors. *Acs Applied Materials & Interfaces* **1**, 1130-1139, doi:10.1021/am900094e (2009).

98 Kang, J., Wei, S. H., Zhu, K. & Kim, Y. H. First-Principles Theory of Electrochemical Capacitance of Nanostructured Materials: Dipole-Assisted Subsurface Intercalation of Lithium in Pseudocapacitive TiO(2) Anatase Nanosheets. *Journal of Physical Chemistry C* **115**, 4909-4915, doi:10.1021/jp1090125 (2011).

99 Nocera, D. G. Chemistry of Personalized Solar Energy. *Inorganic Chemistry* **48**, 10001-10017, doi:10.1021/ic901328v (2009).